The Lamb Shift in Muonic Helium Ions

Die Lamb-Verschiebung in myonischen Helium-Ionen

SIGILL: UNIVERSITAT: LUDOVIC: MAXIM:

München, den 7. Oktober 2015

The Lamb Shift in Muonic Helium Ions

Die Lamb-Verschiebung in myonischen Helium-Ionen

DISSERTATION
AN DER FAKULTÄT FÜR PHYSIK
LUDWIG–MAXIMILIANS–UNIVERSITÄT
MÜNCHEN

VORGELEGT VON:
MARC DIEPOLD

MÜNCHEN, DEN 7. OKTOBER 2015

1.Gutachter: Prof. Dr. Theodor W. Hänsch
2.Gutachter: Prof. Dr. H. Weinfurter
Tag der mündlichen Prüfung: 11.11.2015

Gewidmet meinem besten Freund Jonas, der nun schon seit fast 20 Jahren immer für mich da ist und das auch hoffentlich immer sein wird.

Und meinem Vater Norbert, der immer einen Rat für mich hat wenn ich ihn am meisten brauche.

Ohne euch hätte ich es nicht soweit gebracht, Danke.

Zusammenfassung

Das Thema dieser Arbeit ist die Messung des Lamb shifts in myonischen Helium Ionen, also der Energiedifferenz zwischen den $2S$ und $2P$ Zuständen im gebundenen System aus Heliumkern und negativen Myon. Ziel unseres Experiments ist die Bestimmung der entsprechenden Übergangsenergien in $\mu^4\mathrm{He}^+$ und $\mu^3\mathrm{He}^+$ mit einer Genauigkeit von mindestens 50 ppm. Dies wird durch Laserspektroskopie ermöglicht. Anhand der Messungen wird das quadratische Mittel (rms) des Ladungsradiusses beider Heliumisotope mit einer Genauigkeit von 0.03 % bestimmt. Die resultierenden Ladungsradien sind einen Faktor zehn präziser als die bisherigen Resultate aus der Elektronenstreuung und dienen als fundamentale Parameter für das Verständnis von atomaren Energiespektren und der Kernstruktur.

Unsere Messung beleuchtet auch das sogenannte ”Proton Radius Puzzle” (PRP), eine Abweichung im Standardmodell der Teilchenphysik die durch unser letztes Experiment in myonischem Wasserstoff aufgebracht wurde. Der aus dem damaligen Experiment resultierende Protonenladungsradius war ebenfalls mehr als zehnmal genauer als der bis dahin etablierte Wert (CODATA 2006), jedoch 4 % kleiner. Daraus ergab sich eine Diskrepanz von mehr als sieben Standardabweichungen zwischen dem myonischem Wasserstoff-Wert und den vorangegangenen Messungen aus normaler Wasserstoffspektroskopie und Elektronenstreuung. Trotz andauernder Bemühungen aus verschiedenen Bereichen der Wissenschaft konnte dieses Problem bisher nicht geklärt werden und bleibt eine der größten Unbekannten im Standardmodell der Teilchenphysik.

Die besonders genaue Messung von Ladungsradien durch Spektroskopie in myonischen Atomen wird durch den großen Einfluss der ausgedehnten Ladungsverteilung ermöglicht. Der Energiebeitrag, welcher durch die Kernausdehnung in diesen exotischen Atomen erzeugt wird ist drastisch größer als in elektronischen Systemen. Grund hierfür ist die 200 mal schwerere Myonenmasse welche zu einem kleineren Bohr-Radius des gebundenen Systems führt. Die sich daraus ergebende Verstärkung wird für unsere Messungen genutzt und ist der Hauptgrund warum Spektroskopieexperimente in myonischen Atomen und Ionen schon vor 50 Jahren vorgeschlagen wurden.

Das Experiment in myonischem Helium wurde am Protonenbeschleuniger des Paul Scherrer Instituts in der Schweiz durchgeführt. Die bereit gestellten Myonen werden in einer speziell entwickelten Beamline von hohen Anfangsgeschwindigkeiten heruntergebremst bevor sie das Niedrigdruck-Gastarget erreichen. Dort entstehen myonische Helium Ionen von denen ein kleiner Teil im für die Spektroskopie benötigten $2S$-Zustand überlebt. Die Anregung zum $2P$-Zustand wird mit einem intensiven gepulsten Laser durchgeführt und abgegebene Röntgenstrahlung wird beim Zerfall in den $1S$-Grundzustand detektiert und dient als Spektroskopiesignal.

Während zwei dreimonatigen Messperioden gelang es beide Lamb shift Übergänge in $\mu^4\mathrm{He}^+$ ($2S_{1/2} - 2P_{3/2}$ und $2S_{1/2} - 2P_{1/2}$) mit einer Genauigkeit von 50 ppm zu messen. Die erste Resonanz ist in Fig. 1 zu sehen und die gemessen Übergangsfrequenzen beider Linien sind:

$$\nu_{\,2S_{1/2}-2P_{3/2}} = 368.660(17)_{\mathrm{total}}\,\mathrm{THz}$$

$$\nu_{\,2S_{1/2}-2P_{1/2}} = 333.352(16)_{\mathrm{total}}\,\mathrm{THz}$$

Aus diesen Werten kann ein neuer Ladungsradius des Alphateilchens sowie die Feinstruktur Energiedifferenz (FS) in $\mu^4\mathrm{He}^+$ bestimmt werden:

$$r_{^4\mathrm{He}} = 1.67829(14)_{\mathrm{exp}}(52)_{\mathrm{theo}}\,\mathrm{fm}$$

$$\Delta E_{\mathrm{FS}}^{(\mathrm{Exp})} = 146.022(96)\,\mathrm{meV}$$

Zusätzlich wurden in 2014 noch weitere Lamb shift Übergänge in $\mu^3\mathrm{He}^+$ mit vergleichbarer Genauigkeit gemessen ($2S_{1/2}^{F=1} - 2P_{3/2}^{F=2}$, $2S_{1/2}^{F=0} - 2P_{3/2}^{F=1}$ und $2S_{1/2}^{F=1} - 2P_{1/2}^{F=1}$). Die dazugehörigen Daten sind noch in einem sehr frühen Analysestadium, weshalb in dieser Arbeit nur vorläufige Werte präsentiert werden.

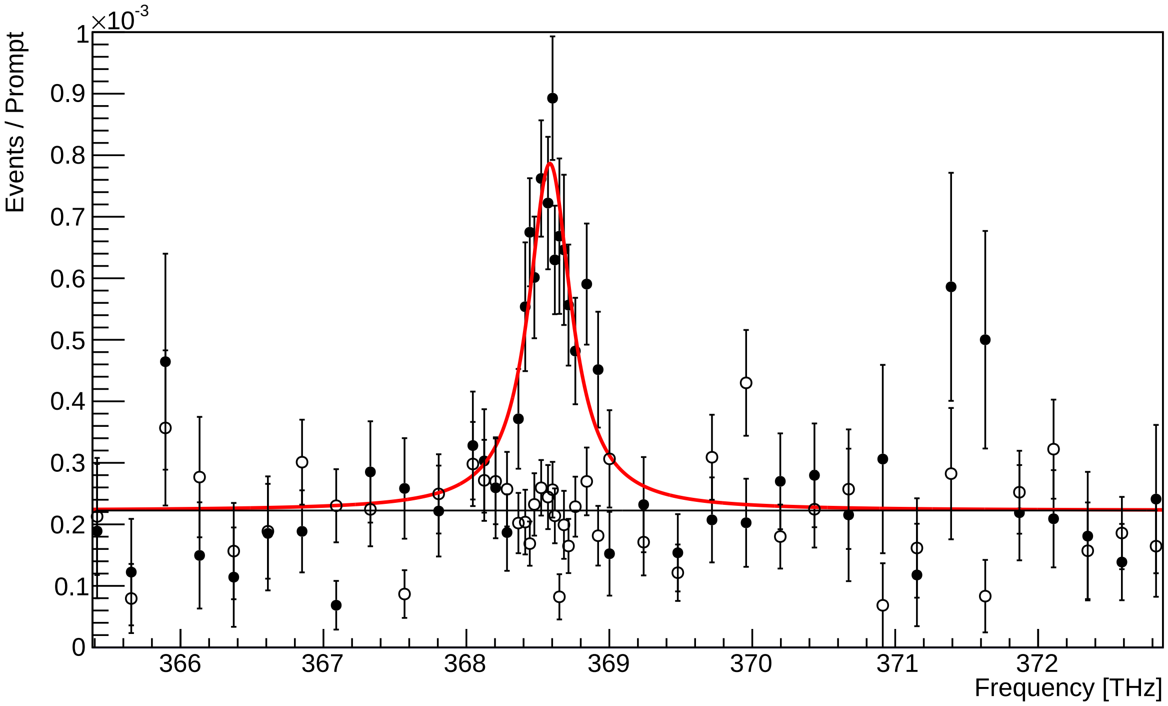

Abbildung 1: $2S_{1/2}-2P_{3/2}$ **Resonanz.** Daten der ersten Lamb shift Messung in $\mu^4\mathrm{He}^+$ welche in 2013 am Paul Scherrer Institut gesammelt wurden. Die rote Kurve zeigt den Lorentz-Fit der gemessenem $2S_{1/2}-2P_{3/2}$ Übergangslinie. Die leeren Punkte zeigen zusätzliche Untergrundmessungen unter den selben Bedingungen wie die Lasermessungen auf gleicher Frequenz. Jeder Datenpunkt entspricht $5-20$ Stunden Messzeit.

Abstract

The subject of this thesis is the measurement of the Lamb shift in the muonic helium ions, i.e. the energy difference between the $2S$ and $2P$ levels in the bound system of a helium nucleus and a negative muon. The experiments goal was to determine the transition energies in $\mu^4\mathrm{He}^+$ and $\mu^3\mathrm{He}^+$ with an accuracy of at least 50 ppm, made possible by employing laser spectroscopy techniques. From these measurements the root-mean-square (rms) charge radii of the helium isotopes will be determined with an uncertainty of 0.03 %, a factor of ten more precise than previous results obtained from electron scattering. These charge radii are fundamental parameters needed for the understanding of atomic energy spectra and nuclear structure.

The presented measurement sheds light on the Proton Radius Puzzle (PRP), a disparity raised by our predecessor experiment performed in muonic hydrogen. Its result provided a proton rms charge radius that was ten times more accurate than the established value from the 2006 CODATA adjustment of fundamental constants. The new result was however 4 % smaller, creating a now seven standard deviations discrepancy between the muonic hydrogen result and other measurements from electronic hydrogen spectroscopy and electron scattering. This problem has not been resolved since 2009, despite continuous efforts from different sides of the scientific community and continues to be one of the biggest unknowns in the standard model of particle physics.

Exceptionally precise and accurate charge radius determinations from muonic atom and ion spectroscopy measurements are possible due to the strongly enhanced influence of the extended charge distribution on the measured Lamb shift transitions. The finite size contribution in these exotic atoms is about two orders of magnitude bigger than in normal electronic systems due to the 200 times higher muon mass that leads to a reduced orbital size. This strong enhancement is exploited in the performed measurement and is the prime reason why spectroscopic experiments in muonic atoms and ions have been proposed for 50 years.

The muonic helium experiment is performed at the proton accelerator facility of the

Paul Scherrer Institute in Villigen (CH) that provides the muons for the measurement. These muons are slowed down from high speeds by trapping them inside a specifically developed low energy beam line before entering a low pressure gaseous helium target. Here they form muonic ions and a small percentage ends up in the metastable $2S$-state that is usable for the laser spectroscopy measurement. Upon successful excitation to the $2P$-state by a high power pulsed laser and the successive decay to the $1S$ ground state, delayed low energy x-rays are detected and serve as signal for the spectroscopy.

During two three-month lasting measurement periods in 2013 and 2014, the project was able to measure both Lamb shift transitions in $\mu^4\mathrm{He}^+$ ($2S_{1/2} - 2P_{3/2}$ and $2S_{1/2} - 2P_{1/2}$, the first one shown in Fig. 2) with accuracies better than 50 ppm. The respective transition frequencies are:

$$\nu_{\,2S_{1/2}-2P_{3/2}} = 368.660(17)_{\mathrm{total}}\,\mathrm{THz}$$
$$\nu_{\,2S_{1/2}-2P_{1/2}} = 333.352(16)_{\mathrm{total}}\,\mathrm{THz}$$

From these values, a new alpha particle charge radius can be extracted and the fine structure splitting (FS) in $\mu^4\mathrm{He}^+$ can be determined:

$$r_{^4\mathrm{He}} = 1.67829(14)_{\mathrm{exp}}(52)_{\mathrm{theo}}\,\mathrm{fm}$$
$$\Delta E_{\mathrm{FS}}^{(\mathrm{Exp})} = 146.022(96)\,\mathrm{meV}$$

Additionally, three Lamb shift transitions in $\mu^3\mathrm{He}^+$ were measured in 2014 with similar precision ($2S_{1/2}^{F=1} - 2P_{3/2}^{F=2}$, $2S_{1/2}^{F=0} - 2P_{3/2}^{F=1}$, and $2S_{1/2}^{F=1} - 2P_{1/2}^{F=1}$). These are still in a preliminary state of analysis and therefore no final results will be given.

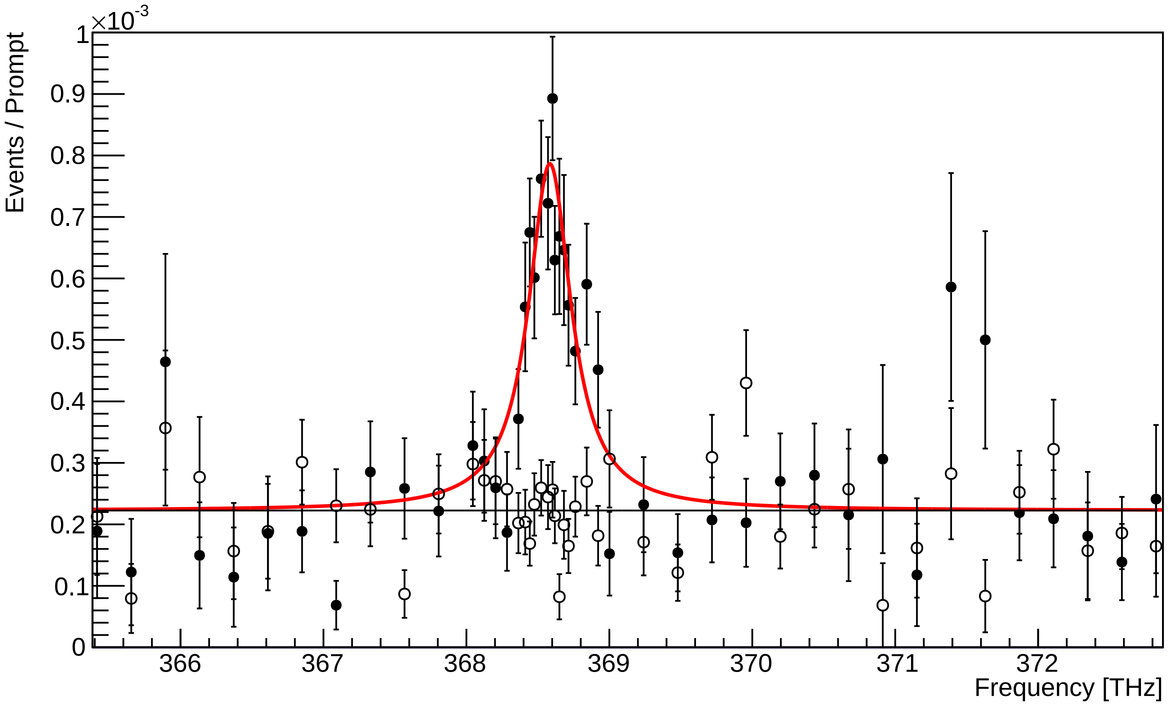

Figure 2: $2S_{1/2} - 2P_{3/2}$ **resonance.** Data of the Lamb shift measurement in μ^4He$^+$ that was gathered in the 2013 beam time at the Paul Scherrer Institute. The red curve shows the Lorentzian fit of the measured $2S_{1/2} - 2P_{3/2}$ transition line. Hollow points show background measurements without laser that happened under the same conditions as the runs on the respective laser frequency. Each data point corresponds to $5 - 20$ hours of measurement time, depending on accumulated statistics and accelerator performance.

Contents

Contents **ix**

List of Figures **xiii**

List of Tables **xv**

Abbreviations **xvii**

The CREMA Collaboration **1**

1 Introduction and Context **3**
- 1.1 The Proton Radius Puzzle 6
  - 1.1.1 Charge Radii from Electron Scattering 8
  - 1.1.2 Charge Radii from Atom and Ion Spectroscopy 10
  - 1.1.3 Charge Radii from Muonic Atom and Ion Spectroscopy 12
  - 1.1.4 Theoretical Discussion of the Puzzle 13
- 1.2 The CERN µHe Measurement 15

2 Energy Levels in Muonic Helium **19**
- 2.1 Leading Order Lamb Shift Contributions 19
- 2.2 Higher Order Lamb Shift Contributions 21
- 2.3 2P Fine Structure 23
- 2.4 Predictions for the $2S_{1/2} - 2P_{3/2}$ and $2S_{1/2} - 2P_{1/2}$ transition based on current theory 24

3 Measurement Principle and Apparatus **29**
- 3.1 Muonic Ion Formation 30
- 3.2 Realization of the Setup 31
- 3.3 Low Energy Negative Muon Beamline 32
- 3.4 Target Volume and Detectors 35
  - 3.4.1 Incoming Muon Detection 35
  - 3.4.2 Gas Target and Circulation System 37

3.4.3 X-ray Detectors 38
3.4.4 Electron Detectors 40
3.5 Laser System 41
3.5.1 Thin Disk Laser Setup 43
3.5.2 Ti:Sa Laser System 46
3.5.3 Non-resonant Multi-pass Cavity 47
3.5.4 Laser Monitoring and Pointing Stabilization 49

4 Data Acquisition and Analysis **53**
4.1 Event Generation and Muon Trigger 53
4.2 Background Reduction and Cuts 55
4.3 Line Shape Model and Fitting of the Resonance Signal 57

5 Systematics **61**
5.1 Resonance Linewidth 61
5.2 Physical Systematic Effects 62
5.2.1 Zeeman Effect 62
5.2.2 Doppler Shift and Broadening 63
5.2.3 DC Stark Shift 64
5.2.4 AC Stark Shift 65
5.2.5 Pressure Shift and Broadening 66
5.3 Laser Parameters 67
5.3.1 Laser Chirp 67
5.3.2 Laser Pulse Energy Calibration 68
5.3.3 Frequency Calibration 70
5.4 Total Uncertainty Budget 72

6 Results and Discussion **73**
6.1 The μ^4He$^+$ $2S_{1/2} - 2P_{3/2}$ Transition 73
6.2 The μ^4He$^+$ $2S_{1/2} - 2P_{1/2}$ Transition 74
6.3 Extracted Value of the ^{4}He Charge Radius 76
6.4 The μ^4He$^+$ Fine Structure Splitting 77
6.5 Preliminary μ^3He$^+$ Results 79
6.6 Conclusion 80

A APD Signal Processing **83**

B Cuts and Detector Calibration **89**
B.1 APD Energy Calibration 89
B.2 APD Energy Cuts 89
B.3 Coincidence Cuts 91

B.4 Delayed Electron Cut 92
B.5 Second Muon Cut 94

C 2S-State Lifetime Determination in μ^4He$^+$ through Two-Photon Decay 95

D Elastic Two-Photon Exchange Contribution to the μ^4He$^+$ Lamb shift 99

E Systematic Studies of Fit Results 103

Bibliography 107

List of Figures

1 $2S_{1/2} - 2P_{3/2}$ Resonanz iii
2 $2S_{1/2} - 2P_{3/2}$ resonance vii
3 People of the collaboration 2

1.1 Energy level scheme of atomic hydrogen 4
1.2 Value of the proton charge radius over time 7
1.3 Rosenbluth separation of G_{E} and G_{M} 8
1.4 Charge radius extraction from form factors 10
1.5 Proton charge radius from different hydrogen measurements 11
1.6 Muonic hydrogen $(2S_{1/2}^{F=1} - 2P_{3/2}^{F=2})$ resonance 13
1.7 Two-photon exchange contribution to the Lamb shift 14
1.8 $2S_{1/2} - 2P_{3/2}$ transition in $\mu^4\mathrm{He}^+$ measured by Carboni *et al.* 16
1.9 X-ray time spectrum 17

2.1 One and two loop vacuum polarization 21

3.1 Atomic cascade and experimental principle 31
3.2 Scheme of the low energy muon beam line at PSI 33
3.3 Photo of the experimental setup 34
3.4 Incoming muon detection system 36
3.5 Photo of partially assembled LAAPD array 38
3.6 Detector geometry around the gas target 39
3.7 Photo of the PSC interior 40
3.8 Laser system schematic 42
3.9 Disk oscillator working principle 44
3.10 Disk multi-pass amplifier 45
3.11 Photo of the disk laser system 46
3.12 Principle of the multi-pass cavity 48
3.13 The non-resonant multi-pass cavity 49
3.14 Cavity fluence monitoring 50
3.15 Intra cavity fluence distribution 51

4.1 Data acquisition system 54
4.2 Principle of the delayed electron cut 56
4.3 Efficiencies of the used cuts 58

5.1 μ^4He$^+$ pressure shift and broadening 67
5.2 Ti:Sa pulse energy measurements 69
5.3 Saturated spectroscopy of Kr and Cs for calibration 70

6.1 The μ^4He$^+$ $2S_{1/2} - 2P_{3/2}$ resonance 75
6.2 The μ^4He$^+$ $2S_{1/2} - 2P_{1/2}$ resonance 76
6.3 Preliminary μ^3He$^+$ $2S^{F=1}_{1/2} - 2P^{F=2}_{3/2}$ resonance 78
6.4 Preliminary μ^3He$^+$ $2S^{F=0}_{1/2} - 2P^{F=1}_{3/2}$ and $2S^{F=1}_{1/2} - 2P^{F=1}_{1/2}$resonances . . . 78
6.5 Isotope shift in helium 79
6.6 Comparison of our data with predictions 81

A.1 Planar APD working principle 83
A.2 Energy spectrum and standard traces 84
A.3 APD trace fitting results 86
A.4 Rise time spectrum and signal classification 87
A.5 APD trace fit χ^2 distribution 88

B.1 Analysis APD energy cuts 90
B.2 Coincidence Cuts 91
B.3 Electron tidiness distribution 93
B.4 Second muon cut 94

C.1 Energy vs Energy x-ray spectrum of two-photon coincidences 96
C.2 Summed energy spectrum of two-photon coincidences 97
C.3 Time spectrum of two-photon coincidences 97

D.1 Form factor functions used for TPE calculation 101

List of Tables

2.1 Nuclear structure independent Lamb shift contributions 25
2.2 Nuclear structure dependent Lamb shift contributions 26
2.3 µ^{4}He$^+$ $2P$-state fine structure splitting 27
2.4 Transition properties of the muonic helium Lamb shift 28

5.1 Zeeman shift in muonic helium 63
5.2 Pulsed Ti:Sa laser pulse chirp 68
5.3 Measured calibration lines 71
5.4 Uncertainty budget for the µ^{4}He$^+$ $2S_{1/2} - 2P_{3/2}$ and $2S_{1/2} - 2P_{1/2}$ lines 72

B.1 Tidiness parameter of the electron classification 92

D.1 Elastic TPE values determined from the calculation 102

E.1 $2S_{1/2} - 2P_{3/2}$ transition fit systematics 104
E.2 $2S_{1/2} - 2P_{1/2}$ transition fit systematics 105

Abbreviations

Overview of the different abbreviations used in this thesis with some brief explanations for each term. Sorted alphabetically.

ADC	*Analog to Digital Converter.* Electronic hardware that measures voltages and converts the signal to computer processable values.
APD	*Avalanche Photo Diode.* Semiconductor solid-state detector that creates a charge current signal through electron multiplication. Used for detecting light, x-rays and charged particles.
BBO	*Beta Barium Borate.* Crystal commonly used for second harmonic generation of laser light. Often used to create green light from Nd:YAG or Yb:YAG lasers.
BSM	*Beyond Standard Model.* Effects and theories currently not described in the standard model of particle physics.
CODATA	*Committee on Data for Science and Technology.* Interdisciplinary work group of the International Council of Science promoting improved data management. Provides globally accepted values of fundamental constants in a least-square-adjustment every four years.
CT	*Cyclotron Trap.* Superconducting magnet system creating a bottle potential for pions and muons in our experiment.
CW	*Continuous Wave.* Term used for lasers that provide light with a constant amplitude and frequency as opposed to pulsed lasers for example.
DAQ	*Data Acquisition (System).* Electronic setup that acquires and pre-processes measurement data and transfers it to a computer for storage and analysis.
eVP	*Electron Vacuum Polarization.* Main QED contribution to the Lamb shift created by the spontaneous creation of electron-positron pairs.
FF	*Form Factor.* Parameterization in momentum space that describes the shape of the electric or magnetic properties of the nucleus.

FP	*Fabry-Pérot.* Optical cavity with high finesse that provides equidistant frequency markers via its transmission fringes.
FS	*Fine Structure.* Splitting of atomic energy levels due to the coupling of angular momentum and lepton spin (Spin-orbit coupling).
FWHM	*Full Width at Half Maximum.* Value describing the width of a Gaussian or Lorentzian distribution at half of the peak‘s maximum amplitude.
HV	*High Voltage.*
LAAPD	*Large Area Avalanche Photo Diode.* Avalanche Photo Diode with extended surface area for large solid angle applications. In our case 14x14 mm^2.
LSM	*Line Shape Model.* Fitting function used for the determination of the resonance position.
LTW	*Laser Time Window.* Time interval in the event where the laser pulse illuminates muonic ions in the gas target creating laser induced x-rays when on resonance.
MEC	*Muon Extraction Channel.* Magnet system used as transfer line and momentum filter for low energy muons.
$\mu^3\mathrm{He}^+$	*Muonic 3-Helium*$^+$ *Ion.* Helion with one bound muon.
$\mu^4\mathrm{He}^+$	*Muonic 4-Helium*$^+$ *Ion.* Alpha particle with one bound muon.
PC	*Pockels Cell.* Electro-optical device acting as a voltage controlled wave plate using the Pockels effect. Used for Q-switching lasers.
PM	*Photo Multiplier.* Single Photon detectors with very high sensitivity. Uses the photoelectric effect to amplify the primary photo-current.
PRP	*Proton Radius Puzzle.* Discrepancy between determination of the proton electric charge radius brought up by the muonic hydrogen Lamb shift measurement.
PSC	*Phase Space Compressor.* Superconducting solenoid magnet used to compress the muon beam size for the usage in our experiment.
PSI	*Paul Scherrer Institute.* Institute with a division for experimental particle physics in Villigen, Switzerland, where the experiment is located.
SOG	*Sum Of Gaussians.* Function parameterization made up out of a sum of Gaussian distributions used in recent FF extractions from elastic electron scattering.
TDC	*Time to Digital Converter.* Electronic hardware that converts the timing of incoming signals to computer processable values.

TFP	*Thin Film Polarizer.* Optical polarizer using interference effects for a given wavelength in a multilayer dielectric coating on a transparent substrate.
TPE	*Two Photon Exchange.* 2nd order nuclear structure dependent contribution to the Lamb shift
Ti:Sa	*Titanium Sapphire.* Translucent crystal used as laser medium for applications between ≈ 600 and 1000 nm
QED	*Quantum Electrodynamics.* Relativistic quantum field theory of electrodynamics. Theoretical framework in which most atomic physics related properties are calculated.
VP	*Vacuum Polarization.* Additional contribution in the photon exchange propagator due to spontaneous creation and annihilation of electron positron pairs.
WFD	*Waveform Digitizer.* Electronic hardware that can store electronic pulse shapes digitally. Works by measuring the input voltage at regular time intervals.
Yb:YAG	*Ytterbium doped Yttrium Aluminum Garnet.* Christaline laser medium for high power lasers with emission at 1030 nm.

The CREMA Collaboration

The experiment discussed in this thesis is part of a project pursued by the CREMA collaboration that has set its goal to perform precision physics measurements by doing laser spectroscopy on muonic atoms. The acronym stands for **C**harge **R**adius **E**xperiments with **M**uonic **A**toms and the collaboration consists currently out of 40 people:

Marwan Abdou-Ahmed[6], Fernando D. Amaro[5], Pedro Amaro[8],Aldo Antognini[1,3], François Biraben[4], Tzu-Ling Chen[9], Daniel S. Covita[7], Andreas J. Dax[1], Marc Diepold[2], Beatrice Franke[2], Luis M.P. Fernandes[5], Sandrine Galtier[4], Andrea L. Gouvea[5], Johannes Götzfried[2], Thomas Graf[6], Theodor W. Hänsch[2], Malte Hildebrandt[1], Paul Indelicato[4], Lucile Julien[4], Klaus Kirch[1,3], Andreas Knecht[1], Franz Kottmann[3], Julian J. Krauth[2], Yi-Wei Liu[9], Jorge Machado[8], Cristina M. B. Monteiro[5], Françoise Mulhauser[2], Boris Naar[3], Tobias Nebel[2], François Nez[4], Jose Paulo Santos[8], Joaquim M. F. dos Santos[5], Karsten Schuhmann[1,3], Csilla I. Szabo[4], David Taqqu[3], Joao F.C.A. Veloso[7], Andreas Voss[6], Birgit Weichelt[6] and Randolf Pohl[2].

Involved in its experiments are nine institutes from five different countries:

1) Paul Scherrer Institute, 5232 Villigen-PSI, Switzerland.
2) Max Planck Institute of Quantum Optics, 85748 Garching, Germany.
3) Institute for Particle Physics, ETH Zurich, 8093 Zurich, Switzerland.
4) Laboratoire Kastler Brossel, University P. et M. Curie, 75005 Paris, France.
5) Physics Department, University Coimbra, 3004-516 Coimbra, Portugal.
6) Institut für Strahlwerkzeuge, Universität Stuttgart, 70569 Stuttgart, Germany.
7) University Aveiro, Campus de Santiago, 3810-193 Aveiro, Portugal.
8) Science and Technology Department, University of Lisbon, 892-516 Caparica, Portugal.
9) Physics Department, National Tsing Hua University, Hsincho 300, Taiwan.

Root mean square (rms) charge radii of light nuclei, that serve as important input parameters in nuclear and atomic theory, are of particular interest for the collaboration. These charge radii are determined with unprecedented precision using the strong enhancement of the finite size effect in muonic atoms, exploited by the experiments at the Paul Scherrer Institute (PSI). Since this is a revolutionary approach, challenges had to be overcome and new techniques had to be developed in order to make the measurements possible. Between the years 1998 and 2009, the collaboration worked hard to set up a laser spectroscopic measurement in muonic hydrogen to determine the size of the proton charge radius. Measurements of the Lamb shift ($2S-2P$ energy difference) in muonic hydrogen and deuterium were completed successfully after more than ten years of combined effort. The muonic hydrogen measurement provided a proton rms charge radius $\sqrt{\langle r_p^2 \rangle} \mathrel{\hat{=}} r_\mathrm{p} = 0.84087(39)\,\mathrm{fm}$ that has a ten times smaller uncertainty than the

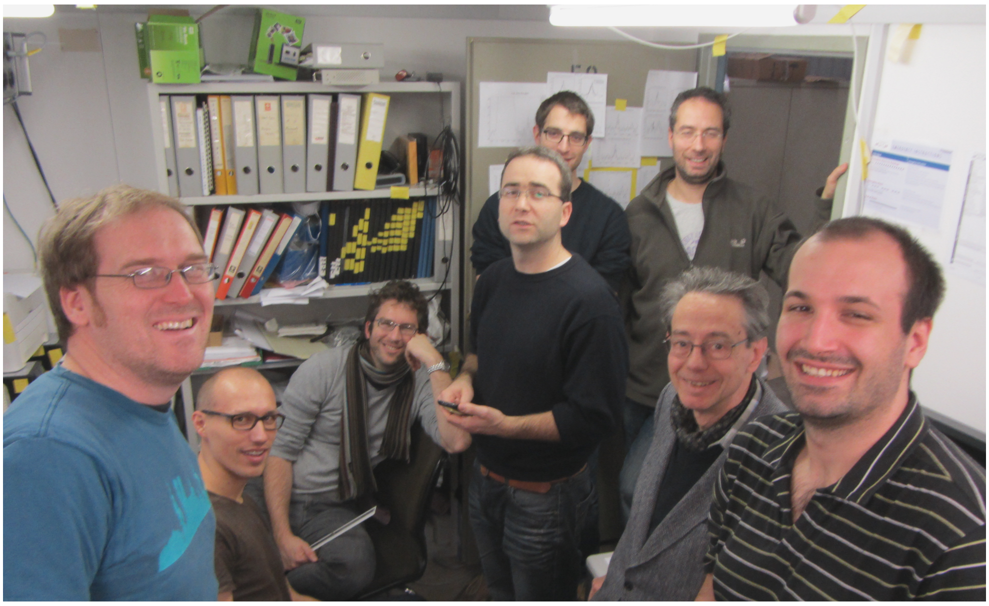

Figure 3: People of the collaboration. Picture of a small part of the CREMA collaboration during the measurement of the muonic helium Lamb shift in 2013 at PSI.

averaged data available until then, marking the effort as a great success [1]. However, this value was 4 % smaller than the average of previous determinations, sparking a lot of interest in the created $7\,\sigma$ discrepancy which is generally denoted as the proton radius puzzle (PRP) .

As successor experiment, a similar measurement in muonic helium has been proposed with the goal to further investigate charge radii of light nuclei, and to shed light on the PRP [2]. Its target is to measure different Lamb shift transitions in $\mu^3\mathrm{He}^+$ and $\mu^4\mathrm{He}^+$ with approximately 50 ppm of accuracy. After three years of preparation, these goals haven been met with great success during two three-month-lasting beam times at PSI in the autumn of 2013 and the summer of 2014. Once data analysis and theoretical considerations are completed, the measurements will allow an extraction of the helion and alpha particle rms charge radii with an accuracy of 0.03 %.

For future endeavors, measurements in other light elements and isotopes are currently considered. The study of muonic tritium could provide interesting data on the nuclear structure differences between the hydrogen isotope and the already measured helion nucleus, and the required experiment could be realized in similar manner to the muonic hydrogen measurement. Additionally, the next system in line after muonic helium, muonic lithium, could give interesting insight in higher order QED effects.

Chapter 1

Introduction and Context

The depiction of nature through physics has changed a lot over the centuries, yet has always been about the struggle to explain the world around us with means that are understandable by the people of its time. The more science and technology advance, the more complex and accurate theoretical predictions have to become in order to adequately describe what we already know about the universe. Vice versa, experimentalists have to perform state-of-the-art research on the edge of current knowledge in order to provide more and more stringent tests that drive the scientific understanding forward. As long as both worlds evolve consistently, they are able to provide new ideas and standards, helping to rule out antiquated theories or facilitating the creation of more complete successors. The most interesting topics in physics are those where observations are made that are neither expected nor understood by the descriptions currently available. These are often motivated by intrinsically discrepant measurements or differences between experiment and theory. Commonly these situations are resolved by improved error treatment or by taking a closer look at the experiments involved, like in the case of the recent report of super-luminous neutrino observation [3]. In rare cases such circumstances remain present after long periods and large efforts from the experimentalists and theorists side. A prime example of this is the so called Proton Radius Puzzle (PRP) [4, 5] that sparked interest in the work of this thesis and will be discussed in this chapter.

In order to get a good understanding of the context of this work, it is worthwhile to talk a bit about the underlying field of atomic physics. Its mainstay is one of the most simple systems imaginable, the hydrogen atom. Its first properties were studied by Joseph Fraunhofer in the year 1814 while looking at the light from our nearest star, the sun. The observed absorption within the lights energy spectrum was first calculated by Johann Jakob Balmer in the year 1885 [6]. He used a special case of a formula later postulated by Johannes Rydberg that allowed to trace back the energy spectrum to a

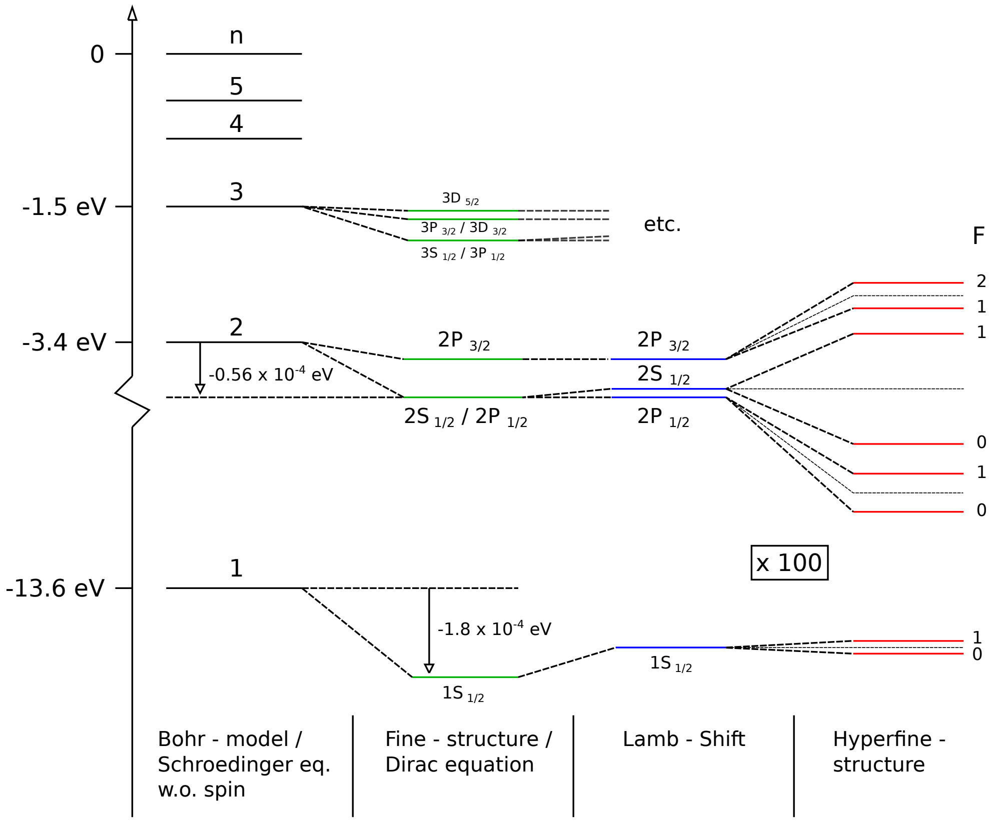
0
-1.5 eV
-3.4 eV
-13.6 eV
n
5
4
3
2
1
-0.56 x 10^-4 eV
-1.8 x 10^-4 eV
3D 5/2
3P 3/2 / 3D 3/2
3S 1/2 / 3P 1/2
etc.
2P 3/2
2S 1/2 / 2P 1/2
2P 3/2
2S 1/2
2P 1/2
1S 1/2
1S 1/2
F
2
1
1
0
1
0
1
0
x 100
Bohr - model / Schroedinger eq. w.o. spin
Fine - structure / Dirac equation
Lamb - Shift
Hyperfine - structure

Figure 1.1: Energy level scheme of atomic hydrogen. Illustration of the various effects that contribute to the hydrogen spectrum. In reality, the effects are not separated and only a combination be measured, i.e. Lamb shift + fine structure (FS) or hyperfine structure (HFS). The hyperfine structure splitting is amplified by a factor of 100 for clarity.

fundamental constant and a simple scaling law. The Rydberg-formula allows the rough calculation of energy levels in bound one-electron systems:

$$E_n = -Z^2\, h\, c\, R_\infty \cdot \frac{1}{n^2}. \tag{1.1}$$

Here E_n is the energy of the single electron atomic/ionic state with principal quantum number n for a nucleus with charge number Z. R_∞ is the Rydberg constant describing the scaling of the level system and c and h are the speed of light and Planck's constant, respectively. Although this formula already gives a good phenomenological description, it took roughly thirty years to provide a plausible model that described the measured observations. In this model brought up by Nils Bohr, where the inner structure of atoms was supposed to behave like a system of planets orbiting a common star [7]. The center of the system is taken by the positively charged nucleus while the role of the planets is filled by electrons. An additional quantization constraint forced the electrons on paths with fixed radii that could only be abandoned by absorbing or emitting a discrete number of photons. The idea that not only light–atom interaction but also atomic properties themselves are quantized, is a cornerstone of modern quantum electro dynamics (QED). QED is a theory commonly used to describe atomic spectra like the level scheme of hydrogen as seen in Fig. 1.1.

The energy levels and transitions of atomic hydrogen extracted from QED are currently among the most precisely calculated and measured quantities known. A prime example of this claim is the energy difference between the ground state and the first exited level, known as the $1S - 2S$ transition. Its value is known to a relative precision of 4×10^{-15} [8, 9]. In order to determine transitions with a that high precision, a large number of different effects have to be considered. The first order result reproducing the values provided by the Rydberg-formula is given nowadays by the solution of the Schrödinger-equation of the two particle system with Coulomb interaction [10]:

$$E\psi = -\frac{\hbar^2}{2m}\left[\frac{1}{r^2}\frac{\partial}{\partial r}\Big(r^2\frac{\partial}{\partial r}\Big) + \frac{1}{r^2\sin\theta}\frac{\partial}{\partial\theta}\Big(\sin\theta\frac{\partial}{\partial\theta}\Big) + \frac{1}{r^2\sin^2\theta}\frac{\partial^2}{\partial\phi^2}\right]\psi + V(r)\psi. \tag{1.2}$$

E are the energy eigenstates of the system, $V(r)$ is the potential of the Coulomb interaction and ψ is the wavefunction of the electron. It is written in a spherical coordinate system with the radial component r, the azimuthal angle θ and the polar angle ϕ. Solving this differential equation provides the already known approximate energy levels, as well as much more elaborate electron orbitals originating from the result of the bound state electron wavefunction [10]:

$$\psi(r,\theta,\phi) = R_{nl}(r)Y_l^m(\theta,\phi) \tag{1.3}$$

$$R_{nl}(r) = -\left[\frac{(n-l-1)!}{2n[(n+l)!]^3}\right]^{1/2}\Big(\frac{2Z}{na_0}\Big)^{l+3/2} r^l e^{\frac{-Zr}{na_0}} L_{n+l}^{2l+1}\Big(\frac{2Zr}{na_0}\Big). \tag{1.4}$$

$Y_l^m(\theta,\phi)$ are spherical harmonics, L_{n+l}^{2l+1} are Legendre polynomials, l is the angular momentum quantum number of the electron (with orientation m) and a_0 is the Bohr radius of the electron in state $n = 1, l = 0$. Energy levels of different l-states for the same n-value are still degenerate in the solution of the Schrödinger equation. The resulting orbitals not only serve as foundation for higher order calculations in atomic systems, but also for the understanding of chemical bonds and molecular structures. In a next step of abstraction, the consideration of the electron spin and relativistic effects inside the orbitals are calculated by solving the Dirac equation. Its solution lifts the n-level degeneracy of the hydrogen spectrum by coupling the magnetic moment of the electron with the one produced by its movement around the nucleus (spin–orbit coupling). In addition, the much smaller effect seen in the hyperfine structure (HFS) can be understood in a similar manner by considering the magnetic moment of the nucleus and its interaction with the total angular momentum of the electron.

Another insight into the hydrogen spectrum is the description of the Lamb shift, experimentally first observed by Lamb and Retherford in 1947. It is predominantly seen as energy difference between the $2S_{1/2}$ and $2P_{1/2}$ state of atomic hydrogen [11]. This effect cannot be completely described in Dirac-theory and must be treated in QED instead. It consists out of terms describing vacuum-fluctuations created in the interaction between the electron and the nucleus as well as additional smaller contributions. One of these added contributions is the finite-size effect that can be calculated semi-classically. Since the orbitals calculated from Eq. 1.2 exhibit a non-zero overlap with the extended nucleus, there is a certain probability for the electron to reside inside the proton. In first order perturbation theory this can be calculated by [12]:

$$\Delta E_{\mathrm{FS}} = \langle \psi | B | \psi \rangle \tag{1.5}$$

$$B(r) = \begin{cases} \frac{Ze^2}{2r_p}[(\frac{r}{r_p} - 3 + \frac{2r_p}{r})] & \text{for } 0 \leq r \leq r_p \\ 0 & \text{for } r \geq r_p \end{cases} \tag{1.6}$$

$$\Delta E_{n=1,l=0} \approx \frac{2Ze^2 r_p^2}{5a_0^3}, \text{ for } \frac{r_p}{a_0} \ll 1 \tag{1.7}$$

It is apparent that this effect strongly depends on the charge radius of the proton (r_p). Since this quantity cannot be calculated a priori at this point, experimental measurements are needed to determine the finite size effect directly. There is a number of different ways to extract the charge radius from independent experiments that will be discussed later in this chapter.

1.1 The Proton Radius Puzzle

One experiment that provides access to the proton charge radius is the muonic hydrogen Lamb shift measurement at the Paul Scherrer Institute (PSI) in Switzerland. It managed to successfully measure the proton charge radius with un-preceded accuracy after more than a decade of effort:

$$r_{\mathrm{p}} = 0.84184(67)\,\mathrm{fm} \quad \text{(CREMA 2010) [1].} \tag{1.8}$$

Improved in 2013:

$$r_{\mathrm{p}} = 0.84085(39)\,\mathrm{fm} \quad \text{(CREMA 2013) [15].} \tag{1.9}$$

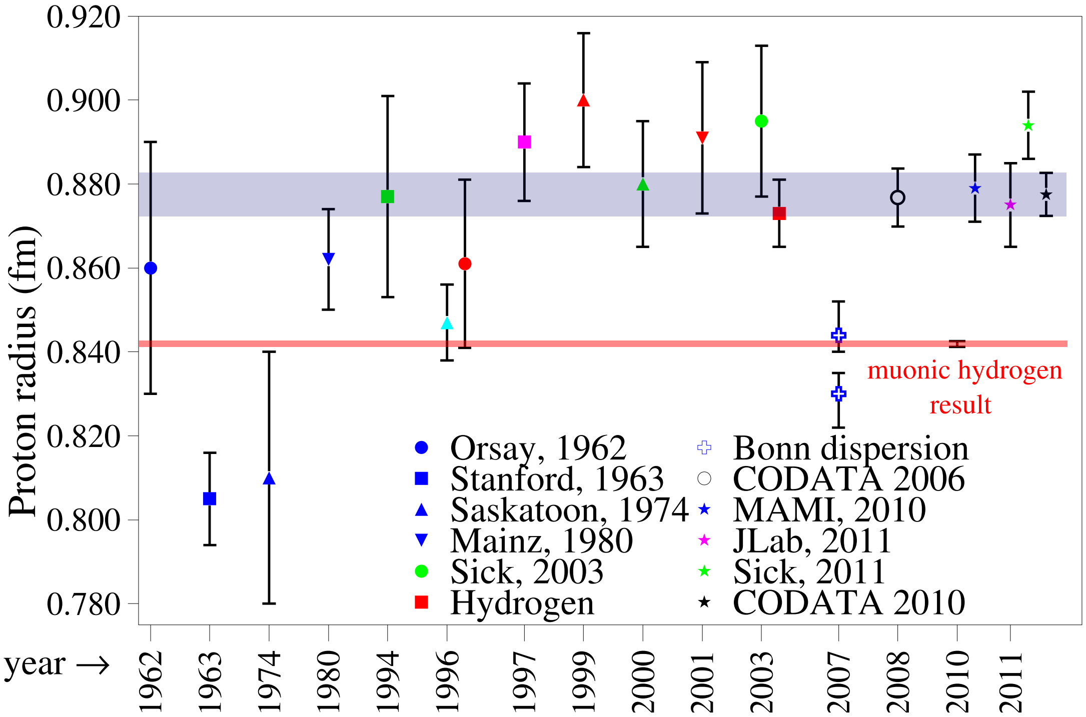

Figure 1.2: Value of the proton charge radius over time. Results of various experiments and fits determining the rms proton charge radius r_p plotted versus the year of the respective publication [13]. The muonic hydrogen result has a ten times smaller error bar than the weighted average of previous measurements (CODATA 2006 [14]) but is roughly $7\,\sigma$ away from the center value of the least squares adjustment. So far no explanation has been found that could shift the µp value.

This newly provided value ”shrunk” the proton by roughly four percent compared to the weighted sum of previously measured results provided in the least squares adjustment of fundamental constants. The value of:

$$r_\mathrm{p} = 0.8768(69)\,\mathrm{fm} \quad \text{(CODATA 2006) [14]}, \tag{1.10}$$

stated there, was calculated from a global fit of hydrogen spectroscopy and electron-proton scattering data provided by Ingo Sick in 2003 [16]. Since both electron scattering measurements and hydrogen spectroscopy agreed on a satisfactory basis over the last decades (see Fig. 1.2) the muonic hydrogen result came as quite a surprise to the scientific community and sparked a lot of interest in the topic. This discrepancy is now known as Proton Radius Puzzle (PRP).

In order to sketch the different approaches and to talk about possible solutions, one has to take a closer look at the three different measurement techniques that contribute to

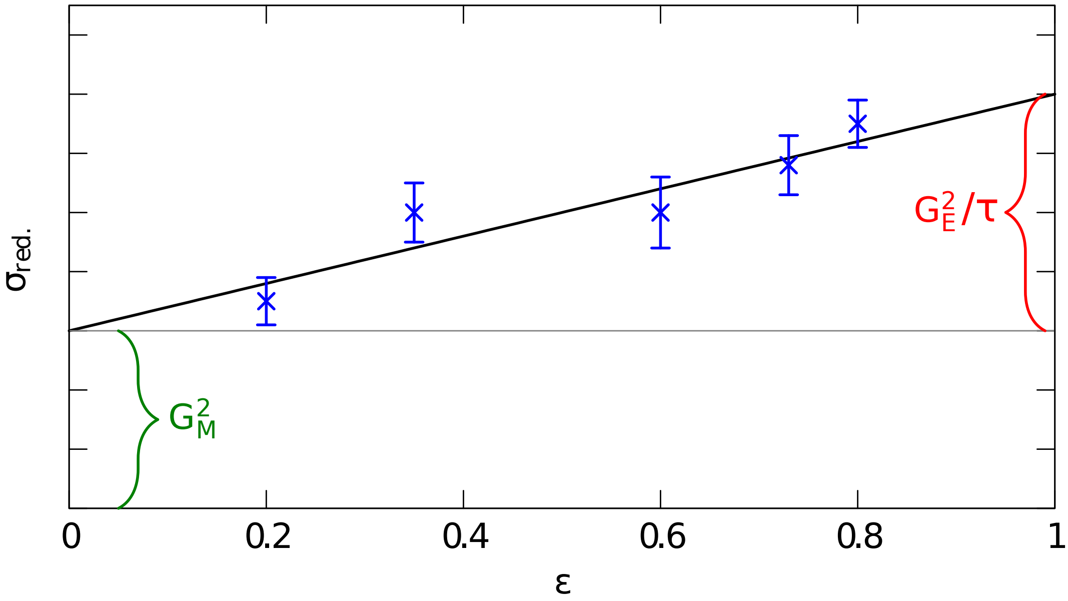

Figure 1.3: Rosenbluth separation of G_{E} and G_{M}. Schematic plot of the reduced scattering cross section $(d\sigma/d\Omega)_{\mathrm{red}}$ versus the virtual photon polarization ϵ (see Eq. 1.12) for a constant momentum transfer value Q^2 obtained by electron scattering experiments [17]. A linear fit allows extraction of G_{E} and G_{M} by determining slope and offset of the reduced cross section.

the current proton charge radius discussion. Each determination type will be explained during the next sections, together with eventual flaws that could lead to a bias in the radius extraction. Once this is done and the current scope of the PRP is presented, its implications for the Muonic Helium Lamb shift measurement will be discussed.

1.1.1 Charge Radii from Electron Scattering

Scattering experiments have been one of the most common ways to extract properties of nuclear structure for over more than half a century [18]. In the case of electron scattering, these measurements are performed by firing a high current, high energy beam in the GeV range onto a pressurized or cryogenically liquidized gas target. The scattered electrons are detected with respect to the incident angle to the incoming electron beam in order to measure the relative scattering cross section σ. The dynamics of this process are parameterized in terms of the relativistic four-momentum transfer Q^2 that is exchanged between the incoming relativistic electron and the quasi static nucleus. To get information about the nucleon electric and magnetic radii in particular, one has to perform a set of measurements with constant Q^2 values at different angles and beam energies. By this, it is possible to extract the electric and magnetic form factors G_{E} and G_{M} from the obtained scattering cross sections. The most common way to access these form factors is by performing a Rosenbluth separation. This method splits the cross section data via a fit in order do provide both quantities separately. The differential scattering cross sections needed can be written as [19]:

$$\frac{d\sigma}{d\Omega} = \Big(\frac{d\sigma}{d\Omega}\Big)_{\text{Mott}} \times \Big[G_{\text{E}}^2 + \frac{\tau}{\epsilon} G_{\text{M}}^2\Big] / (1+\tau), \tag{1.11}$$

where $\tau = Q^2/4\,m^2$, m is the electron mass and ϵ is the virtual photon polarization. Dividing out the constant Mott scattering cross section and using the linearity in ϵ, the form factors can be written in the following expression [19]:

$$\Big(\frac{d\sigma}{d\Omega}\Big)_{red} = \frac{\epsilon(1+\tau)}{\tau} \Big(\frac{d\sigma}{d\Omega_{exp}}\Big) / \Big(\frac{d\sigma}{d\Omega_{\text{Mott}}}\Big) = G_{\text{M}}^2 + \frac{\epsilon}{\tau} G_{\text{E}}^2 \tag{1.12}$$

One has to perform a linear fit in ϵ of this reduced scattering cross section to extract G_{E} and G_{M} from the offset and slope of the fit as seen in Fig. 1.3. When the individual electric form factors G_{E} for each Q^2 value are plotted versus momentum transfer, the nucleon mean-square (rms) charge radius is defined as slope of the electric form factor at zero momentum transfer:

$$\langle r^2 \rangle = -6\hbar^2 \frac{dG_{\text{E}}}{dQ^2}\Big|_{Q^2=0} \tag{1.13}$$

Analogously, this is also possible for the magnetic radius. It has to be noted that even though this is the most convenient approach, recent publications use more complex and robust methods to achieve this splitting [20]. To obtain explicit values for the nucleon charge radii, a fit reaching down to zero momentum transfer has to be performed (see Fig. 1.4).

This gives rise to a problem of increased low–Q^2 sensitivity of the extracted radius. Since arbitrary small scattering angles cannot be realized within experimental constraints, any extraction of the proton charge radius from scattering measurements has to rely on fits of higher Q^2 data and successive extrapolation to $Q^2 = 0$. This can lead to model dependencies of the used fit function providing diverging values of the extracted proton charge radius [21].

In addition, the normalization of the currently best scattering data is not fixed [20]. This leads to additional degrees of freedom that have to be taken into account. Phenomenological fits of the electric form factor with splines and polynomials provide a very good χ^2 for the most recent data set and find a large proton charge radius compared to the muonic hydrogen result:

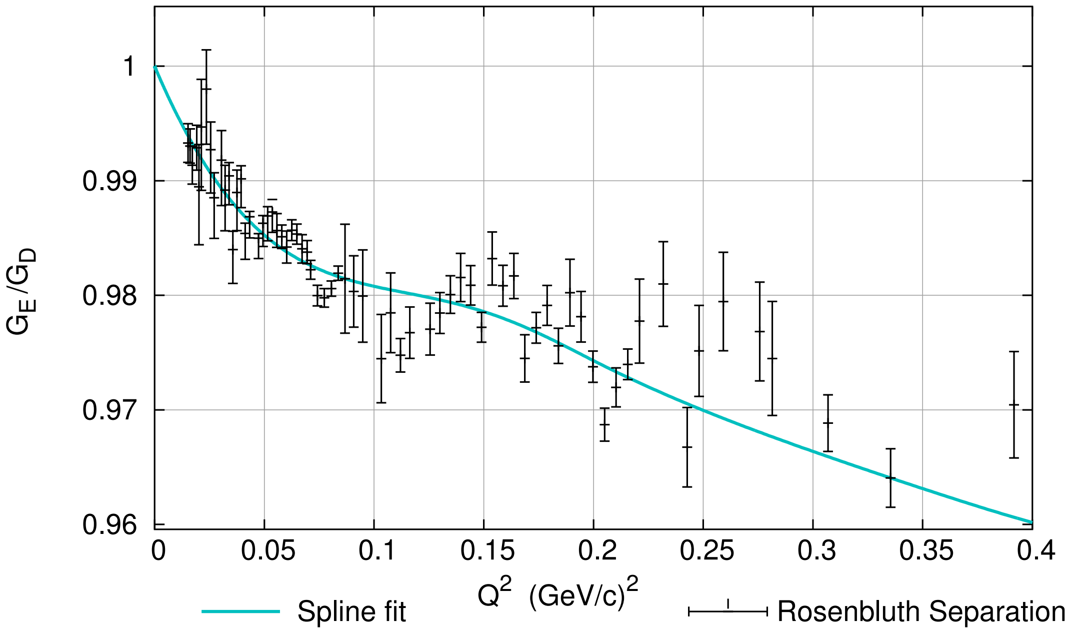

Figure 1.4: Charge radius extraction from form factors. Rosenbluth separated electron scattering data of the electric form factor G_E normalized to the dipole form factor G_D and plotted versus momentum transfer Q^2 [22]. The slope of the fit at $Q^2 = 0$ determines the obtained charge radius value.

$$r_\mathrm{p} = 0.879 \pm 0.005_\mathrm{stat} \pm 0.004_\mathrm{syst} \pm 0.002_\mathrm{model} \pm 0.004_\mathrm{group}\,\mathrm{fm}. \tag{1.14}$$

(MAMI. 2010 [20])

During this determination, measures were taken to study the systematic effects of model dependent fitting results, leading to the last contribution of the above stated error.

It has to be noted that there are still doubts on the validity of this extraction. Dispersion relation fits using a vector meson dominance model provides a different, smaller proton radius from the same dataset although at worse χ^2 values:

$$r_\mathrm{p} = 0.84 \pm 0.01\,\mathrm{fm}\ \text{(Disp. 2012 [23])}, \tag{1.15}$$

1.1.2 Charge Radii from Atom and Ion Spectroscopy

Complementary to the measurements done in electron scattering, nuclear charge radii can also be determined by performing laser spectroscopy in regular atoms and ions. As already motivated, the energy levels in the atomic spectrum are influenced in varying

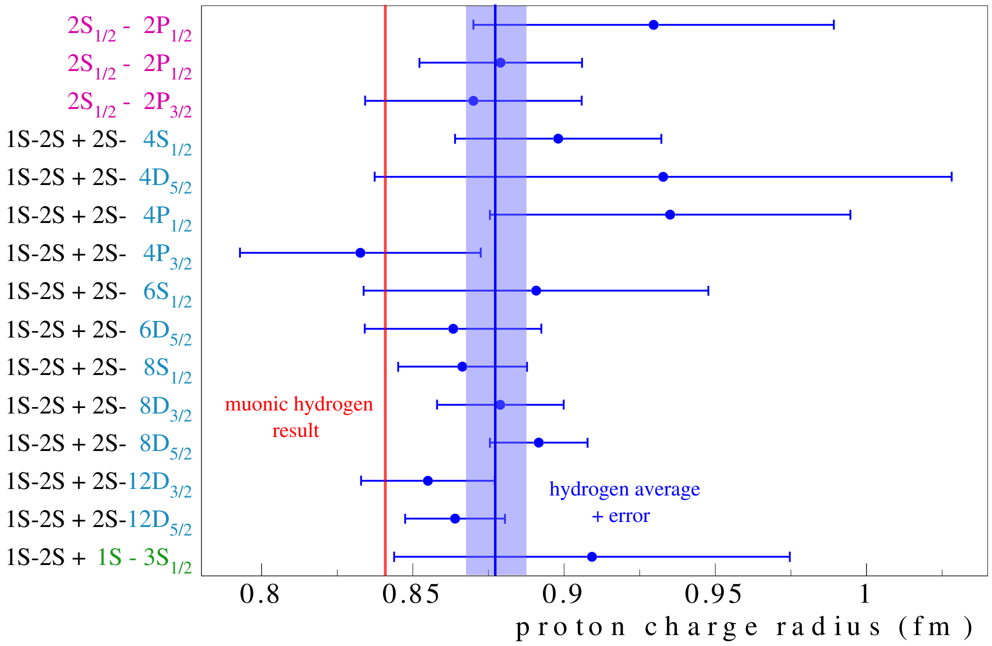

Figure 1.5: Proton charge radius from different hydrogen measurements. Extracted proton charge radius from electronic hydrogen measurements when their result is combined with the result of the $1S - 2S$ transition energy [8, 13]. Most of the individual measurements agree with the muonic hydrogen value at 0.84 fm, only the average does differ significantly.

degrees by the finite size of the nucleus. For most measurements this is only a minor contribution however. The finite size effect in hydrogen is encoded in the $1S$-Lamb shift (L_{1S}) and scales approximately inversely to the third power of the principal quantum number n. It is however only one of the relevant parameters required to accurately predict the atomic energy spectrum from QED calculations. Another one is the Rydberg constant which has a larger influence on the overall scaling of the energy spectrum. The energy level scaling in atomic hydrogen is approximately given by (in frequency units) [5]:

$$E_{nS}/h \simeq -\frac{R_\infty}{n^2} + \frac{L_{1S}}{n^3}, \tag{1.16}$$

$$L_{1S} = 8171.636(4)\ \text{MHz} + 1.5645\ \text{MHz/fm}^2 \cdot r_p^2, \tag{1.17}$$

$$R_\infty = 3289.841960364(17)\ \text{THz}. \tag{1.18}$$

To obtain both parameters one needs at least two independently measured transitions with sufficient precision. As the first one, the precisely measured $1S - 2S$ transition is chosen [8, 9]. Due to the different orbital-core-overlap of both involved states, its sensitivity to the Lamb shift is not negligible. To extract the Rydberg component one normally chooses a set of energy differences for higher n-states that show an reduced sensitivity to the charge radius [24, 25]. A global fit of the available data allows the determination of both parameters making it possible to extract nuclear charge radii from the Lamb shift. Measurements of various two-photon transitions starting at the $2S$-state determine the proton radius from hydrogen spectroscopy as can be seen in Fig. 1.5. The extracted radius is given by:

$$r_\mathrm{p} = 0.8779 \pm 0.0094\,\mathrm{fm}\ \text{(H-Spec. 2012 [26])}. \tag{1.19}$$

Additional measurements of the different $2S-4P$ and $1S-3S$ transitions are also able to provide data for the extraction of the proton radius [27, 28], as does a direct measurement of the $2S-2P$ transition via radio-frequency spectroscopy [29]. New measurements in this field will provide updated data on the proton radius puzzle and will check if the discrepancy between normal and muonic hydrogen spectroscopy persists [27, 28, 30].

1.1.3 Charge Radii from Muonic Atom and Ion Spectroscopy

A more promising system for the extraction of nuclear charge radii that is still accessible to laser spectroscopy was found in so-called exotic atoms. In exotic atoms the electron is replaced by another, heavier particle. Of interest for charge radii extraction are so-called muonic atoms, where the replacement particle is a negatively charged muon with a mass of roughly 206 m_e. The reason is that the already mentioned finite size effect strongly depends on the Bohr radius of the measured system itself ($\sim a_0^{-3}$, see Eq. 1.7). Shrinking the Bohr radius therefore improves the sensitivity on the finite size effect drastically. The reduced mass in muonic hydrogen for example shrinks the Bohr-radius of the system by a factor of 186, leading to a $186^3 \approx 10^7$ times larger relative overlap between the nucleus and the lepton orbital. When compared to normal hydrogen this highly increased effect renders the uncertainty provided by the Rydberg constant completely negligible.

As can be derived from Eq. 1.4, leptons in S-states show the highest probability of presence at the origin. In contrast, P-states show a local minimum at the origin leading to a drastically reduced wave function overlap with the nucleus. Therefore the measurement of different $2S-2P$ (Lamb shift) transitions further enhances the sensitivity on the finite nuclear size. Using these advantageous factors, the CREMA collaboration was able to provide a 25 times more accurate value of the proton charge radius compared to spectroscopic measurements in normal hydrogen, even though the absolute frequency uncertainty of roughly 1 GHz is much less precise than any of the individual measurements which contribute to the electronic hydrogen spectroscopy value [1].

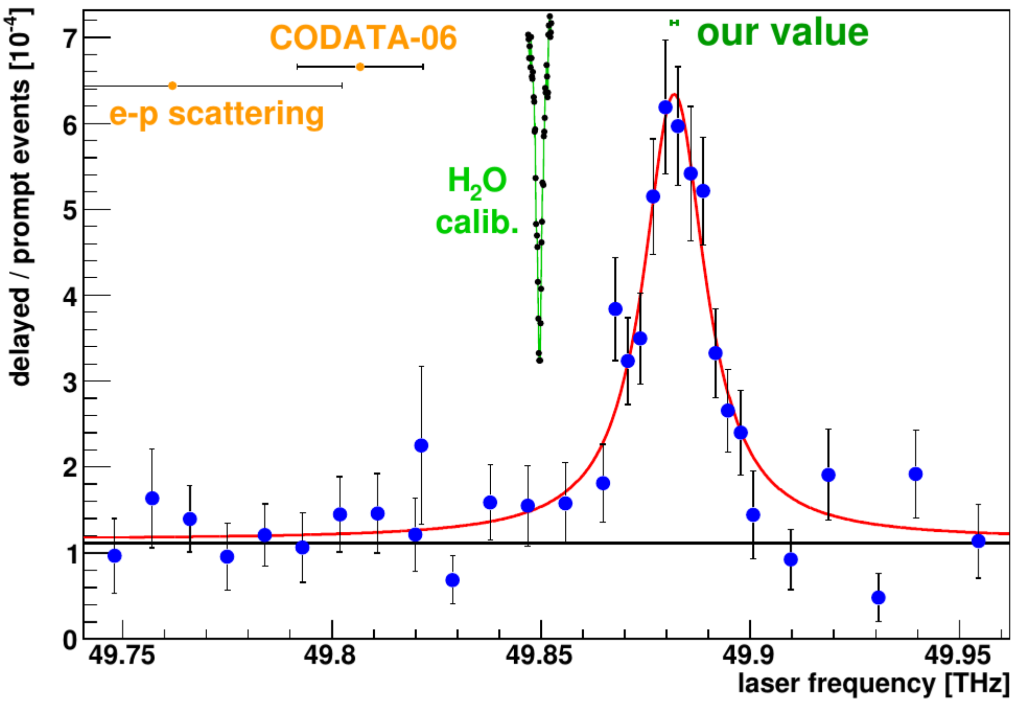

Figure 1.6: Muonic hydrogen ($2S_{1/2}^{F=1} - 2P_{3/2}^{F=2}$) resonance . One of two independently measured Lamb shift resonances in muonic hydrogen that determines the extracted proton charge radius value [1]. As the indication of the CODATA-06 value shows, the resonance position is far away from the expected position.

To provide credibility of this new experimental approach, systematic studies in muonic hydrogen have thoroughly investigated effects which could lead to a shift in the measured frequencies [31]. However, the size of all systematic effects was found to be only fractions of the measured linewidth, whereas a more drastic shift would be required to be compatible with the CODATA value (see Fig. 1.6). Since then, there have been five consistent measurements of different Lamb shift transitions in the muonic hydrogen isotopes. Two in µH [1, 15] and three in µD [31]. This further substantiates the integrity of the measurements.

1.1.4 Theoretical Discussion of the Puzzle

Another important part of the puzzle is derived from the theory involved in the extraction of the proton charge radius from the muonic hydrogen measurements. The QED terms needed for this were calculated and checked by multiple sources [32–36]. Nevertheless one higher order contribution was temporary supposed to be a possible solution for the puzzle. The term held responsible is the so called proton polarizability contribution to the Lamb shift. As seen in Fig. 1.7, the polarizability term describes a

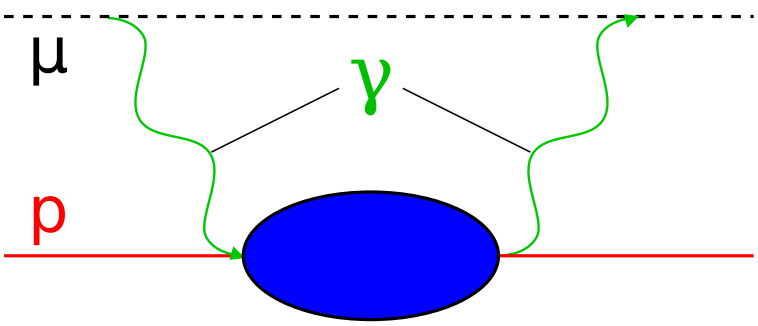

Figure 1.7: Two-photon exchange contribution to the Lamb shift. Feynman diagram showing the two-photon exchange of the proton polarizability. A first photon emitted by the lepton leads to an excitation of the proton that is then successively probed by the second photon. This effect was mentioned as possible solution for the proton size puzzle [37, 38] but was found to be not significant [39].

two-photon exchange (TPE) mechanism that leads to an effective deformation of the charge distribution of the proton. It is related to the proton's resonances (excitation spectrum) by standard dispersion relations [40]. According to calculations, this effect leads to an additional energy of 0.0127(5) meV in the Lamb shift [41]. Compared with the size of the discrepancy (0.31 meV) this effect is therefore small.

Postulation of uncovered off-shell contributions could lead to a contribution similar in size to the discrepancy [37, 38]. Even though this idea is not completely ruled out at this point, independent sources argued that it will not solve the proton radius puzzle due to already being included and being too small in size [39].

Another discussed idea is the requirement of a non-perturbative treatment of the vacuum polarization in muonic atoms. This might be needed since some of the required simplifications could break down due to the muon's high mass and decreased orbit [42]. A contribution from vacuum polarization inside the nucleus was also studied and could lead to a shift of the muonic hydrogen value although it has not been verified yet [43,44].

In contrast to approaches that assume fundamental flaws in the current QED theory description, there are also other, yet not yet tested ideas. When all of the individual measurements and the corresponding QED theory is valid, there would be a directly observable difference between electronic and muonic bound systems, possibly questioning lepton universality. Adding to this notion, is that the most accurate g-factor measurement of the muon provided by the Brookhaven Laboratories disagrees more than 3σ with the theoretical prediction [45]. With two muon-related discrepancies present, the discussion also moved to effects that are currently not covered in the standard model of particle physics.

One of the possible beyond standard model (BSM) explanations for both discrepancies is given by the existence of an unstable neutral vector boson in the mass range $m_e \ll m_B \ll m_\mu$ that has not been found so far [46, 47]. This particle would differentiate in force propagation between electron and muon, fundamentally altering the muonic results. Its existence would resolve the discrepancy, but would also shift the rms proton charge radius extracted by normal hydrogen spectroscopy slightly [42].

This model provides a prediction for the measurements described in this thesis and can therfore be tested. According to [46], a shift of the extracted alpha particle rms charge radius value ($\Delta r^2_{^4\mathrm{He}} = -0.06\,\mathrm{fm}^2$) should be observed when evaluating it from the muonic helium Lamb shift transitions.

1.2 The CERN μHe Measurement

In order to provide a complete picture, not only about the proton radius puzzle but also about previous measurements, the following section gives a brief introduction to an experiment similar to the one reported in this thesis. The mentioned effort was undertaken in the 1970s by E. Zavattini and colleagues at the CERN experimental facilities [48]. Special attention is given to the discovered problems with the CERN experiment and why the interpretation of the measurement is not reliable.

It was known from calculations and experiments that by stopping muons in gaseous helium environments, a certain percentage of $\mu^4\mathrm{He}^+$ ions ends up in the metastable $2S$-state [49]. Since the required negative muons could only be generated with high kinetic energies in accelerator facilities, high gas pressures of 40 bar were used to stop a sufficient amount of muons to perform an laser experiment (see Chap. 3). Direct studies seemed to show that the lifetime and population of muonic helium atoms in the $2S$-state were sufficiently high at such gas pressures to justify a laser experiment [50]. This was later questioned by multiple sources from the experimental and theoretical community, since it disagreed with the predicted scaling determined in low pressure experiments [51].

A first measurement of the $2S_{1/2} - 2P_{3/2}$ transition was reported by the collaboration working at the CERN 600 MeV synchrocyclotron in 1976 [48]. To perform the spectroscopy, their setup used a tuneable dye laser pumped by a Q-switched ruby laser, while multiple plastic scintilators provided the required trigger signals on muon arrival inside the 40 bar He gas target. Additional NaI slabs were used to register the emit-

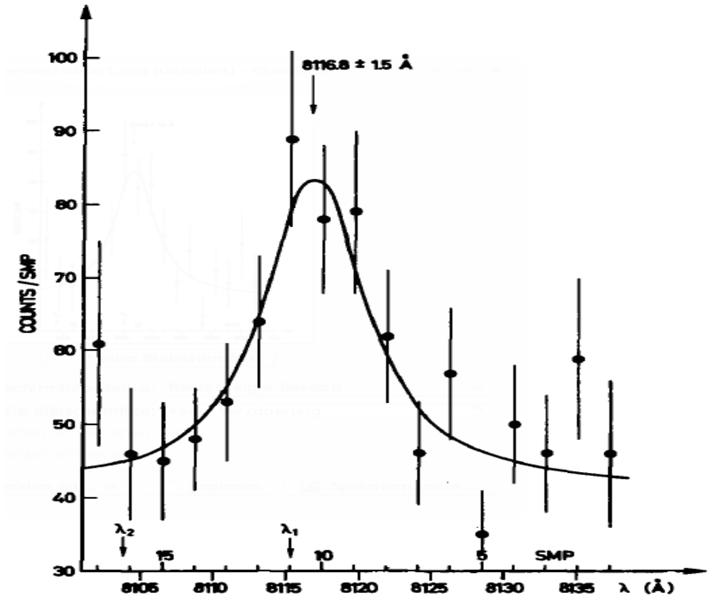

Figure 1.8: $2S_{1/2}-2P_{3/2}$ **transition in** $\mu^4\mathrm{He}^+$ **measured by Carboni** ***et al.*****.** Reported signal of the $2S_{1/2}-2P_{3/2}$ transition in $\mu^4\mathrm{He}^+$ by Carboni, Zavattini *et al.* published in 1977 [48]. The truncated y-axis hides a quite low signal to noise ratio.

ted 8 keV x-rays resulting from a successful transfer of $2S$ atoms to the $2P$ state and the successive de-excitation to the ground state. Two measurements found agreeing positions of the $2S_{1/2} - 2P_{3/2}$ transition at approximately 811.7 nm [48, 52], and the resonance with the highest statistical significance can be seen in Fig. 1.8. Additional measurements in the same apparatus provided a value of the $2S_{1/2} - 2P_{1/2}$ line later, backing up the claims made [53].

In order to test the CERN resonance measurement an additional experiment at PSI was granted to verify the position of the $2S_{1/2}-2P_{3/2}$ transition in $\mu^4\mathrm{He}^+$ [54]. The experiment was done at gas pressures of 40 mbar, a factor 1000 lower than in the CERN measurement. There, experimental and theoretical results agreed for the lifetime of the required $2S$-ions. To achieve muon capture in this low pressure environment, the muons were caught in a gas filled, rotationally symmetric magnetic bottle, similar in manner to what is used as a first stage in our setup. A laser pulse was used to drive the transition inside the gas chamber while flat multi-wire proportional chambers detected the produced 8.2 keV $\mathbf{K}_\alpha$ x-rays. The result of this experiment excluded the position of the $2S_{1/2} - 2P_{3/2}$ resonance within the range of 811.4 nm to 812.0 nm with a probability of greater than 95%, ruling out the previously reported result [54]. Within the x-ray time spectrum no influence of the laser induced events could be observed as seen in Fig. 1.9. Since the overall population of the $2S$ state in $\mu^4\mathrm{He}^+$ only

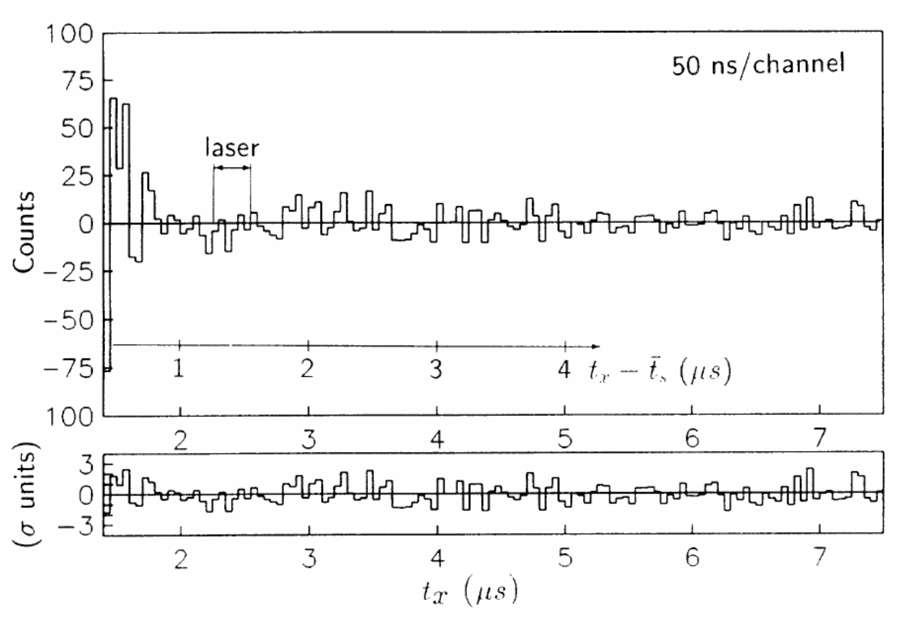

Figure 1.9: X-ray time spectrum. Time spectrum of $\mathbf{K}_\alpha$ x-rays taken at the PSI $\mu^4\mathrm{He}^+$ Lamb shift measurement [54]. No visible indication of laser induced events in the laser time window was found. The absence of any significant effect on the $\mu^4\mathrm{He}^+$ ion x-ray emission excludes previous results provided by the collaboration at CERN.

amounts to roughly 1% [51] and the overall x-ray detection efficiency in the experiment was low, statistics did not allow an extended search for the real $2S_{1/2}-2P_{3/2}$ resonance.

Up to this point it is not clear what was measured at both CERN experiments. It is the now accepted knowledge that the population of the $2S$-state is quenched within very short times at the high pressures hat were used in the CERN experiment. Therefore the results of Zavatini *et al.* are to be considered dubious and are now excluded with more than $10\,\sigma$ by our experimental results (see Chap. 6) as well as by the results of Hauser *et al* [54].

Chapter 2

Energy Levels in Muonic Helium

It is apparent that simple calculations as presented in Chap. 1 are not sufficient to determine the value of the alpha particle charge radius on a level which is comparable to the previous measurement in muonic hydrogen. There is a number of different terms contributing to the theoretical Lamb shift and fine structure calculations in $\mu^4\mathrm{He}^+$. Each of them has to be considered in order to accurately calculate both $2S-2P$ energy differences to an adequate precision. The main contribution of the Lamb shift will be discussed and all higher order terms are summarized within this chapter to provide the theoretical background for the charge radius determination. The basis for the theoretical summary are the works of Borie, and the groups of Martynenko, Jentschura, Karshenboim and Bacca [35, 55–61].

To directly extract the alpha particle charge radius from the $2S-2P$ transitions measured in $\mu^4\mathrm{He}^+$, it is suitable to use the following parameterization:

$$\Delta E_{(2S_{1/2}-2P_j)} = \Delta E_{\mathrm{LS}}^{\mathrm{indep.}} + \Delta E_{\mathrm{LS}}^{\mathrm{dep.}}(\langle r^2\rangle) + \delta_{j,\frac{3}{2}} \cdot \Delta E_{\mathrm{FS}}. \tag{2.1}$$

The energy differences are split in charge radius independent ($\Delta E_{\mathrm{LS}}^{\mathrm{indep.}}$) and charge radius dependent terms ($\Delta E_{\mathrm{LS}}^{\mathrm{dep.}}$). For the $2S_{1/2}-2P_{3/2}$ transition the $2P$ fine structure interval of the muonic helium ion (ΔE_{FS}) has to be added in order to account for spin-orbit coupling of the muon. Since the FS only contains a minor nuclear structure related contribution it can be treated without explicit charge radius dependence. As the alpha particle has no nuclear spin, no hyperfine splitting has to be considered in the $\mu^4\mathrm{He}^+$-ion.

2.1 Leading Order Lamb Shift Contributions

The largest term in the muonic atom and ion Lamb shift stems from the first order contribution of the electron vacuum polarization (eVP). This charge radius independent effect describes the creation of electron-positron pairs by the exchanged photon between lepton and nucleus in propagation of the Coulomb force. A Feynman diagram of this process can be seen in Fig. 2.1 a). To calculate this effect, the evaluation using a quasi-potential method in quantum electrodynamics is needed. Muonic atom eigenstates are calculated by solving the Schroedinger equation of the bound system where the particle interaction can be parameterized using the Breit Hamiltonian and the wavefunctions of the $2S$ and $2P$ state [55]:

$$H_B = \frac{\mathbf{p}^2}{2\mu} - \frac{Z\alpha}{r} - \frac{\mathbf{p}^4}{8m_1^3} - \frac{\mathbf{p}^4}{8m_2^3} - \frac{Z\alpha}{2m_1m_2r}\left(\mathbf{p}^2 + \frac{\mathbf{r}(\mathbf{r}\cdot\mathbf{p})\mathbf{p}}{r^2}\right) + \frac{Z\alpha}{r^3}\left(\frac{1}{4m_1^2} + \frac{1}{2m_1m_2}\right)(\mathbf{L}\cdot\sigma_\mathbf{1}), \tag{2.2}$$

$$\psi_{2lm}(r,\theta,\phi) = \frac{W^{3/2}}{2\sqrt{6}} \cdot e^{\left(-\frac{Wr}{2}\right)} \cdot WrY_{lm}(\theta,\phi), \tag{2.3}$$

$$W = \mu Z\alpha \qquad \mu = m_1m_2/(m_1+m_2). \tag{2.4}$$

Here m_1 and m_2 are the masses of the nucleus and the muon and $Y_{lm}(\theta,\phi)$ are spherical harmonics. The Uehling term can be calculated by taking into account the vacuum polarization potential [55]:

$$V_{VP}^C(r) = \frac{\alpha}{3\pi}\int_1^\infty d\xi\rho(\xi)\left(-\frac{Z\alpha}{r}exp(-2m_e\xi r)\right), \tag{2.5}$$

$$\rho(\xi) = \frac{\sqrt{\xi^2-1}(2\xi^2+1)}{\xi^4}. \tag{2.6}$$

Since the Lamb shift is defined as the $2S_{1/2} - 2P_{1/2}$ energy difference, both the $2S$ and $2P$ shifts contribute. The individual results are obtained by numerically integrating to get the expectation value of the Hamiltonian. A shift of the $2S$-level of 2077.2217 meV is obtained while the $2P$-level is shifted 411.4486 meV in the same direction [55]. Including further corrections, the total energy splitting due to the first order eVP is given as [35, 55, 56, 62]:

$$\Delta E_{\text{eVP}}^{\text{1-loop}}(2P-2S) = 1666.2945(15)\,\text{meV}. \tag{2.7}$$

The next leading order charge radius independent part of the Lamb shift is given by the Källén-Sabry term. It describes the two-loop vacuum polarization contribution to the one-photon interaction of the Lamb shift [10]. Its size can be calculated in similar manner to the Uehling term by modifying the photon propagator and summing over all possible terms. The three Feynman diagrams contributing to the Källén-Sabry term are given in Fig. 2.1 b)-d). The total value of the two-loop correction in the one-photon and two-photon interaction was calculated to be [55, 56, 58]:

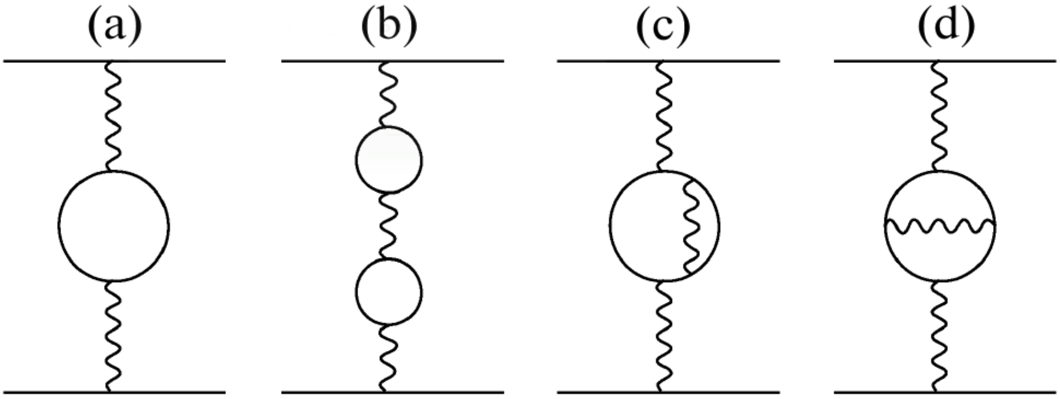

Figure 2.1: One and two loop vacuum polarization. Feynman diagrams contributing to the one- and two-loop terms in the Lamb shift for the exchange in a single photon. The leftmost diagram describes the Uehling term which is the biggest contribution to the Lamb shift, while the neighboring three diagrams contribute to leading order Källén-Sabry term.

$$\Delta E_{\mathrm{eVP}}^{2-\mathrm{loop}} = 13.2769(26)\,\mathrm{meV}. \tag{2.8}$$

The biggest nuclear structure dependent contribution to the Lamb shift in muonic atoms is given by the finite size effect. This effect is probed by the orbiting lepton while inside the nucleus, leading to a reduction in binding energy. The $2P$-state is unaffected since the leading order finite size contribution scales with the square of the lepton wave function at the origin. For the $2S$-state the energy shift scales with the nuclear rms charge radius squared [35, 55, 56]:

$$\Delta E_{\mathrm{fin.size}} = -\frac{\mu^3 (Z\alpha)^4}{12} \left\langle r^2 \right\rangle = 105.321(2)\,\mathrm{meV/fm} \cdot \left\langle r^2 \right\rangle . \tag{2.9}$$

Since the mentioned leading order terms are not sufficient to extract the alpha particle charge radius from $\mu^4\mathrm{He}^+$ spectroscopy, the next section will give an extended overview of the higher order calculations from the listed sources.

2.2 Higher Order Lamb Shift Contributions

All relevant contributions needed to extract an improved rms radius of the alpha particle with sufficiently high accuracy have been compiled into two tables for the nuclear structure independent (Tab. 2.1) and dependent (Tab. 2.2) terms in a manner congruent to previous works [36]. The terms for the total nuclear structure independent part were taken from [35,55–59] and sorted to avoid double counting of individual contributions.

Multiple terms differ between the already mentioned sources. In those cases, our value is given by the center value of most differing calculations with an uncertainty that includes of all individual data points. Using this we obtain the total value of the nuclear structure independent part of the Lamb shift:

$$\Delta E_{\text{LS}}^{\text{indep.}} = 1668.4840(59)\,\text{meV}. \tag{2.10}$$

The summary includes all QED corrections up to the order of $(Z\alpha)^6$. As seen in (Tab. 2.1) there is no term that disagrees above a few µeV between the different sources. Some contributions are only calculated by a single author, therefore not allowing additional cross checks. These include relativistic corrections to the two-loop eVP contribution [55], two out of three light-by-light scattering contributions [59], as well as the total logarithmic recoil [57]. The term describing the recoil in the finite size effect given in [56] is neglected in the presented sum since it is already accounted for in the main two-photon exchange (TPE) term in Tab. 2.2.

The main theoretical uncertainty of the Lamb shift extraction is derived from certain terms in the nuclear structure dependent part (given in Tab. 2.2). The two terms in question are the elastic and inelastic TPE contributions that were found to be difficult to calculate:

$$\Delta E_{\text{TPE}}^{\text{elastic}} = 1.40(2)\frac{\text{meV}}{\text{fm}^3}\cdot\left\langle r^2\right\rangle^{3/2}, \qquad \Delta E_{\text{TPE}}^{\text{inelastic}} = 2.47(15)\,\text{meV}. \tag{2.11}$$

The calculation of the elastic term in [55] used a Gaussian form factor parameterization that is assumed to be a very good approximation for the ^{4}He nucleus. Furthermore they provided the same calculation using a dipole parameterization to obtain an upper limit of the form factor model dependence. Since the dipole shape gives no reasonable estimate of the model dependence due to its drastically altered shape, I studied this effect further as seen in App. D, thereby reducing the respective uncertainty by a factor five compared to the initial publication.

A higher order eVP correction calculated by [55] is ignored in our summary because a partially canceling term exists in the polarizability contributions. These higher orders have not been included in the polarizability, therefore adding the elastic correction would wrongly shift the TPE values.

The inelastic contribution is provided by ab-initio calculations of the polarizability are provided using two independent state-of-the-art nuclear potentials [60]. The previous calculation agrees with the new value but has significantly larger uncertainties compared to the latest result [60]. Even though it was found that this term is partly canceled by the elastic TPE part [63], we decided to keep them separated since it is unknown how well the cancellation is for the helium nuclei. We also exclude Bacca's calculation of the elastic term because it assumes a perfect cancellation with the matching inelastic terms as in muonic deuterium [61].

Polarizability contributions of the individual nucleons have to be accounted for in the determination of the Lamb shift. The contribution for a proton-neutron pair in muonic deuterium was calculated to be $\Delta E_{\mu D}^{hadr} = 28(2)\,\mu\text{eV}$, based on deuteron inelastic data [64]. In order to obtain the corresponding value for $\mu^4\text{He}^+$ this has to be scaled with the nucleon number as well as the third power of the reduced mass and nuclear charge ratio:

$$\Delta E_{\mu\text{He}}^{hadr} = N_{\mu He}/N_{\mu D} \cdot (\mu_{\mu He}/\mu_{\mu D} \cdot Z_{\mu He}/Z_{\mu D})^3 \cdot \Delta E_{\mu D}^{hadr} = 0.48(10)\,\text{meV}. \qquad (2.12)$$

The uncertainty of this term was increased by a factor of two to account for the uncertain scaling compared to muonic deuterium. Multiple experts from the field of nuclear theory validated this uncertainty approximation and are currently working on an more accurate value for $\mu^4\text{He}^+$ and $\mu^3\text{He}^+$ [65]. Using this, the total parameterization of the nuclear structure dependent part of the Lamb shift is given by:

$$\Delta E_{\text{LS}}^{\text{dep}} = -106.357(8)\frac{\text{meV}}{\text{fm}^2} \cdot \langle r^2 \rangle + 1.40(2)\frac{\text{meV}}{\text{fm}^3} \cdot \langle r^2 \rangle^{3/2} + 3.02(18)\,\text{meV}. \qquad (2.13)$$

2.3 2P Fine Structure

In order to extract the Lamb shift from the measured $2S_{1/2} - 2P_{3/2}$ transition, the 2P fine structure ($2P_{3/2} - 2P_{1/2}$ energy difference) has to be included in the transition energy. The fine structure contribution can be calculated to a sufficient level in Dirac theory when additional electron vacuum polarization, the muon anomalous magnetic moment and recoil effects are calculated separately and included. Higher order terms stemming from nuclear finite size and second order vacuum polarization effects have been included in the summary given Tab. 2.3. The used values were taken from [56, 58, 66] and agree on the required accuracy level. The total $2P$ fine structure in $\mu^4\text{He}^+$ is given by:

$$\Delta E_{\mathrm{FS}} = 146.192(13)\,\mathrm{meV}. \tag{2.14}$$

The respective experimental results of this work will be discussed further in the end of this thesis (see Chap. 6).

2.4 Predictions for the $2S_{1/2} - 2P_{3/2}$ and $2S_{1/2} - 2P_{1/2}$ transition based on current theory

Adding all respective terms from the nuclear structure independent part in Tab. 2.1 and the components influenced by nuclear structure in Tab. 2.2, one obtains a parameterization of the $\mu^4\mathrm{He}^+$ Lamb shift based on current theory. The energy difference of the measured $2S_{1/2} - 2P_{1/2}$ and $2S_{1/2} - 2P_{3/2}$ transitions with respect to the ^{4}He rms charge radius (in fm) are:

$$\Delta E_{(2P_{1/2}-2S_{1/2})}(\langle r^2\rangle\,) = 1671.50(18) - 106.357(8)\,\langle r^2\rangle\; + 1.40(2)\,\langle r^2\rangle^{3/2}\;\mathrm{meV}, \tag{2.15}$$

$$\Delta E_{(2P_{3/2}-2S_{1/2})}(\langle r^2\rangle\,) = \Delta E_{(2P_{1/2}-2S_{1/2})}(\langle r^2\rangle\,) + 146.192(13)\,\mathrm{meV}. \tag{2.16}$$

Using this, it is possible to extract two independent charge radius values from the measured $\mu^4\mathrm{He}^+$ transitions or to reduce the statistical uncertainty by combining both measurements. Alternatively, the measurements can be used for a direct determination of the fine structure in $\mu^4\mathrm{He}^+$.

Using the most precise value of the alpha particle charge radius available from electron scattering (1.681(4) fm [67]) the respective expected transition frequencies can be calculated:

$$\Delta E_{(2P_{1/2}-2S_{1/2})} = 1377.61(1.43)\,\mathrm{meV} \mathrel{\widehat{=}} 333.10(35)\;\mathrm{THz}, \tag{2.17}$$

$$\Delta E_{(2P_{3/2}-2S_{1/2})} = 1523.80(1.43)\,\mathrm{meV} \mathrel{\widehat{=}} 368.45(35)\;\mathrm{THz}. \tag{2.18}$$

Similar values served as guide for the search of the Lamb shift transitions during the measurement campaign. More information on all the muonic helium Lamb shift transitions can be found in Tab. 2.4.

nuclear structure independent terms in [meV]

#	Contribution	Martynenko [55]		Borie-v7 [56]		Karshenboim [35, 58, 59]		Jentschura [57, 62]		Our Choice		Ref.
1	NR one-loop electron VP (eVP)	1665.7730	#1			1665.7729	[35] Tab. I	1665.772	[62] Sec. II			
2	Rel. corr. to one-loop (Breit-Pauli)	0.5210	#7, 10			0.52110	[35] Tab. IV; #4	0.521104	[57] Eq. 17d			
3	Rel. one-loop eVP			1666.305	Tab. 5; #1							
19	Rel. RC to eVP $\alpha(Z\alpha)^4$			−0.0090	Tab. 5; #11							
	Sum: One-loop eVP (total)[a]	1666.2940		1666.296		1666.2940	[58] Tab. I; #1	1666.293		1666.2945	±0.0015	B, K, M, J
4	Two-loop eVP (Källen-Sabry)	11.5693	#2	11.573	Tab. 5; #2							
5	One-loop eVP in 2 C-lines $\alpha^2(Z\alpha)^5$	1.7075	#9	(1.709)	Tab. 5; #3			1.707588	[57] Eq. 13d			
	Sum: Two-loop eVP [b]	13.2768		13.282		13.2769	[58] Tab. I; #2			13.2769	±0.0026	B, K, M
6+7	Third-order eVP	0.0703	#4, 11, 12	(0.074(3))	Tab. 5; #4	0.074(3)	[58] Tab. I; #3			0.0722	±0.0019	K, M
29	Second-order eVP contrib. $\alpha^2(Z\alpha)^4$m	0.0021	#8, 13			0.00572	[58] Tab. VIII eVP2			0.00572		K
9	1:3 LbL (Wichmann-Kroll)	−0.0199	#5;			−0.01995(6)	[59] Tab. III; #1					
10	2:2 LbL (Virtual Delbrück)					0.0114(4)	[59] Tab. III; #2					
9a	3:1 LbL					−0.0050(2)	[59] Tab. III; #3					
	Sum: Light-by-light scattering[c]	(−0.0135)		(−0.0136)		−0.0136(6)				−0.0136	±0.0006	K
20	μSE and μVP	−11.1070	#24	−11.105708	Tab. 2					−11.1063	±0.0006	B, M
11	μSE corr to eVP $\alpha^2(Z\alpha)^4$	(−0.0646)	#28 Eq. 99	−0.1314[e]	App. C Tab. 16	−0.06462	[58] Tab. VIII; a	−0.06462	[57] Eq. 29d	−0.06462		K
12	eVP loop in SE $\alpha^2(Z\alpha)^4$	−0.0307	#27			−0.03073	[58] Tab. VIII; d					
30	Hadr. loop in SE $\alpha^2(Z\alpha)^4$m					−0.00041(4)	[58] Tab. VIII; e					
13	Mixed eVP + μVP	0.0023	#3	0.00208	Tab. 5	0.00395	[58] Tab. VIII; b					
31	Mixed eVP + had.VP					0.0025(2)	[58] Tab. VIII; c					
21	Higher ord. corr. to μSE/μVP			−0.034663	Tab. 2							
	Sum: Higher orders [d]	−0.0284		−0.032583		−0.02469(20)				−0.02864	±0.0039	B, K, M
14	Hadronic VP	0.2229	#29	0.228(12)	Tab. 5; #7					0.22545	±0.0026	B, M
17	Recoil corr. $(Z\alpha)^4m^3/M^2$ (Barker-Glover)	0.2952	#21	0.2952	Tab. 5; #12			0.29518	[57] Eq. A3	0.29518		J
22	Rel. RC $(Z\alpha)^5$	−0.4330	#22	−0.4330	Tab. 5; #8			−0.433032	[57] Eq. 32d	−0.433032		J
23	Rel. RC $(Z\alpha)^6$	0.0038	#23							0.0038		M
24	Higher ord. rad. recoil corr.	−0.0377[e]	#25	−0.04737	Tab. 5; #9; p.9					−0.04737		B
28	Rad. (only eVP) RC $\alpha(Z\alpha)^5$							0.003867	[57] Eq. 46d	0.003867		J
	Recoil finite size[f]			0.2662(1)	Tab. 5; #10							
	Sum	1668.4809		1668.8641(50)[g]						1668.4840	±0.0059	

[a] sum: 1+2 / 3+19 [b] sum: 4+5 [c] sum: 9+9a+10 [d] sum: 12-21 [e] incomplete [f] included in TPE [g] taken from text in [56] p. 14

Table 2.1: Nuclear structure independent Lamb shift contributions. Terms contributing to the μ^4He^+ Lamb shift that are independent of the alpha particle nuclear structure. The last column shows the values used for our Lamb shift determination. Terms in brackets were cited from other publication and not calculated by the author. Errors for the different terms are either given in the respective publication or represent the spread of the different calculations. All values are given in meV.

nuclear structure dependent terms

#	Contribution	Martynenko [55]		Borie-v7 [56]		Karshenboim [35]		Bacca [60, 61]		Our Choice			Ref.
n1	NR finite size	$-105.323\,\langle r^2\rangle$	#14	$-105.319\,\langle r^2\rangle$	Tab. 14ba	$-105.32\,\langle r^2\rangle$	Tab. III; #1			-105.3210	± 0.0020	$\langle r^2\rangle$	B, K, M
n2	Rad. corr. finite size $\alpha(Z\alpha)^5$	$-0.0250\,\langle r^2\rangle$ [a]	#26; Eq. 92	$-0.0250\,\langle r^2\rangle$	Tab. 14bb					-0.0250		$\langle r^2\rangle$	B, M
n3	Finite size corr. $(Z\alpha)^6$	$-0.1370\,\langle r^2\rangle$	#26; Eq. 91(1)	$-0.1310\,\langle r^2\rangle$	Tab. 14bc					-0.1340	± 0.0030	$\langle r^2\rangle$	B, M
n4	Fin. size one-loop eVP (Uehling)	$-0.3414\,\langle r^2\rangle$	#16										
n5	Fin. size two-loop eVP (KS)	$-0.0027\,\langle r^2\rangle$	#18										
	Fin. size one&two-loop eVP [b]	$-0.3441\,\langle r^2\rangle$		$-0.3297\,\langle r^2\rangle$	Tab. 14bd	$-0.333\,\langle r^2\rangle$	Tab. III; #3			-0.3369	± 0.0072	$\langle r^2\rangle$	B, K, M
n6	Fin. size one-loop eVP in 2 C-lines	$-0.5362\,\langle r^2\rangle$	#17	$-0.5392\,\langle r^2\rangle$	Tab. 14be	$-0.536\,\langle r^2\rangle$	Tab. III; #2			-0.5376	± 0.0016	$\langle r^2\rangle$	B, K, M
n7	Fin. size 2-loop eVP in 2 C-lines	$-0.0065\,\langle r^2\rangle$	#19;							-0.0065		$\langle r^2\rangle$	M
n8	Finite size corr. to 2p1/2			$-0.004206\,\langle r^2\rangle$	Tab. 14b(2p1/2)					0.004206[c]		$\langle r^2\rangle$	B
n9	Elastic TPE (3rd Zemach)	$1.4040\,\langle r^2\rangle^{3/2}$	#15	$1.4000\,\langle r^2\rangle^{3/2}$	Tab. 5; #16			$1.33(4)\,\langle r^2\rangle^{3/2}$ [d]	[60]	1.40	± 0.02[e]	$\langle r^2\rangle^{3/2}$	M
n10	One-loop corr. to Elastic TPE [f]	$0.0270\,\langle r^2\rangle^{3/2}$	#20										
n11	Inelastic TPE (polarizability)	(2.47(15))[g]		(3.1(6))[h]	Tab. 5; #23			2.47(15)	[61] #2	2.470	± 0.150		Ba
n12	nucleon polarizability									0.480	± 0.100[e]		
n13	Remaining $(Z\alpha)^6$ contrib.	0.07846	#26; Eq. 91(2)	0.055	Tab. 5; #17					0.067	± 0.012		B, M
	Sum	$-106.3718\langle r^2\rangle+1.4310\langle r^2\rangle^{3/2}+2.55(15)$		$-106.340\langle r^2\rangle+1.40(4)\langle r^2\rangle^{3/2}+3.1(6)$ p. 14						$-106.357(8)\langle r^2\rangle+1.40(2)\langle r^2\rangle^{3/2}+3.02(18)$			

[a] wrong sign in [55] [b] sum: n4+n5 [c] sign changed due to convention [d] assumes cancelations with #11 [e] this work [f] cancelations with α^6 terms in #11 [g] originates from [61] [h] originates from [68]

Table 2.2: Nuclear structure dependent Lamb shift contributions. Nuclear structure dependent terms to the $\mu^4\text{He}^+$ Lamb shift with their respective charge radius scaling. All values are give in meV, meV/fm^2, or meV/fm^3. Further discussion of the elastic and inelastic TPE contribution is given in the text. Charge radius dependent terms of the different orders are summed to provide the given parameterization.

fine structure

#	Contribution	Martynenko [66]		Borie-v7 [56]		Karshenboim [35, 58]		Our Choice		Ref.
f1	Dirac			145.7183	Tab. 7; #1					
f2	Recoil corr.			−0.1107	Tab. 7; #6					
f3	$(Z\alpha)^4$ contrib.	145.56382	#1							
f4a	$(Z\alpha)^6$ contrib.	0.01994	#3							
f4b	$(Z\alpha)^6 \mathrm{m}_1/\mathrm{m}_2$ contrib.	−0.00045	#4							
f11*	$\alpha(Z\alpha)^6$ contrib.	−0.00056	#8							
	Sum: Dirac [a]	145.58273		145.6076				145.5952	±0.0124	B, M
f5a	One-loop eVP (Uehling), $\alpha(Z\alpha)^4$	0.13167	#5							
f5b	One-loop eVP in FS interaction	0.14396	#7							
	Sum: One-loop eVP [b]	0.27563		0.2753	Tab. 7; #2	0.27502	[35] Tab. IV	0.2753	±0.0003	B, K, M
f6a	Two-loop eVP (Källen-Sabry)	0.00097	#10,11							
f6b	Two-loop eVP in 2 C-lines	0.00231	#9,12,13	0.0021	Tab. 7; #3					
	Sum: 2-loop eVP [c]	0.00328				0.00247	[58] Tab. VII	0.0029	±0.0004	K, M
f12*	One-loop μVP	0.00001	#6					0.00001		M
f8	μ anom. mag. mom. (a_μ)			0.3290	Tab. 7; #4					
f9	μ anom. mag. mom. higher orders			0.0013	Tab. 7; #5					
	Sum: μ anom. mag. mom. [d]	0.33032	#2	0.3303				0.33032		B, M
f10a	Finite size (1st ord.)	−0.01176	#14	−0.0119	Tab. 7; #7			−0.0118	±0.0007	B, M
f10b	Finite size (2nd ord.)	0.00045	#15					0.00045		M
	Sum	146.18068	[66]	146.2034	B			146.1923	±0.0124	

[a] sum: f1+f2 / f3+f4a+f4b+f11 [b] sum: f5a+f5b [c] sum: f6a+f6b [d] sum: f8+f9 [*] new term

Table 2.3: $\mu^4\mathrm{He}^+$ $2P$-state fine structure splitting. Terms contributing to the fine structure in $\mu^4\mathrm{He}^+$ taken from different sources. The sources agree on the significant level for all calculated contributions.

Transition	ΔE (meV)	λ (nm)	ν (THz)	η	$M(a_\mu^2)$	$f_{a,b}$	F_{sat} (J/cm^2)	Rate (h^{-1})
μ^4He $2S_{1/2}-2P_{1/2}$ *	1380	898	333	1	3	4/12	2.2	48
μ^4He $2S_{1/2}-2P_{3/2}$ *	1526	812	368	1	6	8/12	1.1	48
μ^3He $2S_{1/2}^{F=0}-2P_{1/2}^{F=1}$	1119	1108	270	1/4	3	1/12	2.1	6
μ^3He $2S_{1/2}^{F=1}-2P_{1/2}^{F=1}$ *	1286	964	310	3/4	2	2/12	3.2	22
μ^3He $2S_{1/2}^{F=0}-2P_{3/2}^{F=1}$ *	1294	958	312	1/4	6	2/12	1.1	12
μ^3He $2S_{1/2}^{F=1}-2P_{1/2}^{F=0}$	1344	923	344	3/4	1	1/12	6.4	13
μ^3He $2S_{1/2}^{F=1}-2P_{3/2}^{F=2}$ *	1436	863	347	3/4	5	5/12	1.3	36
μ^3He $2S_{1/2}^{F=1}-2P_{3/2}^{F=1}$	1461	849	353	3/4	1	1/12	6.4	16

Table 2.4: Transition properties of the muonic helium Lamb shift. Energy difference ΔE, vacuum wavelength λ, frequency ν, sublevel population η, matrix element M (in units of the respective Bohr radius a_μ), transition strength $f_{a,b}$ and saturation fluence F_{sat} of the muonic helium Lamb shift transitions. Transitions denoted with a * have been successfully measured in the experiment. The event rates have been calculated assuming only 30% of the saturating fluence is used to avoid power broadening. Measured event rates were a factor of 2-3 smaller, probably due to imperfection in the target cavity. These values are based on knowledge available prior to the measurements, and are therefore subject to small changes.

Chapter 3

Measurement Principle and Apparatus

The µHe Lamb shift experiment described in this work is operated at the proton accelerator facility of the Paul Scherrer Institute in Switzerland. It successfully measured the $2S_{1/2} - 2P_{3/2}$ transition in the $\mu^4\mathrm{He}^+$ ion during a three month beam time in the end of 2013 by means of laser spectroscopy. After upgrades to the experiment, the $2S_{1/2} - 2P_{1/2}$ transition in $\mu^4\mathrm{He}^+$ could be measured in summer of 2014, as well as the $2S_{1/2}^{F=1} - 2P_{3/2}^{F=2}$, $2S_{1/2}^{F=0} - 2P_{3/2}^{F=1}$, and $2S_{1/2}^{F=1} - 2P_{1/2}^{F=1}$ transitions in $\mu^3\mathrm{He}^+$

This chapter focuses on the principles and details of our experimental setup consisting of beam-line, detectors, and high power spectroscopy laser system. It starts by explaining the creation process of muonic atoms in low pressure gaseous environments and the difficulties and conditions that arise from this (see Sec. 3.1). Additionally a rough overview of the experimental principle is given in order to motivate the ways in which the setup is conceptualized (Sec. 3.2).

The following sections describe the individual components of the experiment in detail. Sec. 3.3 gives information on the apparatus that is used for providing low energy muons, consisting out of a so-called Cyclotron Trap (CT) and an additional low energy beam line, the Muon Extraction Channel (MEC).

Sec. 3.4 explains the low pressure helium gas target where the actual Lamb shift excitation takes place. This includes a discussion of the muon detection system, providing the trigger signal for the pulsed laser and the data acquisition system (DAQ). A short introduction to the used gas circulation and purification system is given before the detectors for x-ray and electron measurements are discussed.

The laser system is presented in Sec. 3.5. It consists out of a seeded titanium sapphire (Ti:As) ring laser system, pumped by a two-stage, Q-switched Yb:YAG Disk-Oscillator-Amplifier setup. The non-resonant multi-pass cavity illuminating the µHe$^+$-ions inside the gas target is also explained.

3.1 Muonic Ion Formation

In order to be able to measure the different Lamb shift transitions in µHe$^+$-ions, muonic ions have to be prepared in the $2S$ state first. Driving the $1S-2S$ transition directly is not possible via means of laser excitation (as done in electronic hydrogen for example). This is due to the very strong binding potential created by the reduced Bohr radius in muonic atoms and ions, leading to a $1S-2S$ energy in the x-ray regime. Since there are no appropriate lasers available, one has to rely on other means of obtaining $2S$-ions.

Muons injected into a gaseous environment undergo collisions with the surrounding atoms or molecules. Ionization of the gas particles through impacting muons leads to a net energy loss per collision for the muon. For muons in gaseous helium, the lower limit of the net energy loss per interaction is given by the binding energy of the second helium electron. This equates to: $\Delta E_{\mathrm{ion}}^{\mathrm{e}} = 24.6\,\mathrm{eV}$ [69]. Collisions continue until the kinetic energy of the muon is below this threshold and the muon becomes weakly bound to a helium nucleus by ejecting the first electron via Auger emission [70]. The second electron of the helium nucleus is also ionized by the now bound muon and a muonic ion in a highly excited state is created. The initial excitation level of the muon (n) is given by the maximal overlap of the electronic and muonic wavefunction that can be estimated by [70]:

$$n \sim \sqrt{m_r^{\mu^4He^+}/m_r^{e^4He^+}} \sim 14, \tag{3.1}$$

where m$_r$ are the reduced masses of the respective systems. The atomic cascade taking place after muonic ion formation leads to a prompt de-excitation of these highly excited states [70]. A scheme describing the atomic cascade is presented in Fig. 3.1. At high n-levels, Auger- and Coulomb de-excitation effects dominate, while at $n < 10$ radiative effects become more important. These radiative transitions lead to the emission of keV x-rays during the cascade. Muons following the path along the $l = n - 1$ threshold are undergoing so-called circular transitions and end up in the $1S$ ground state. These ions are lost for the experiment. Stark mixing in collisions with surrounding helium atoms however leads to a re-population of all l sub levels in the spectrum during the cascade. This provides a roughly $2\,\%$ probability for muonic helium ions to end up in the $2S$ state (at a few hPa) [70].

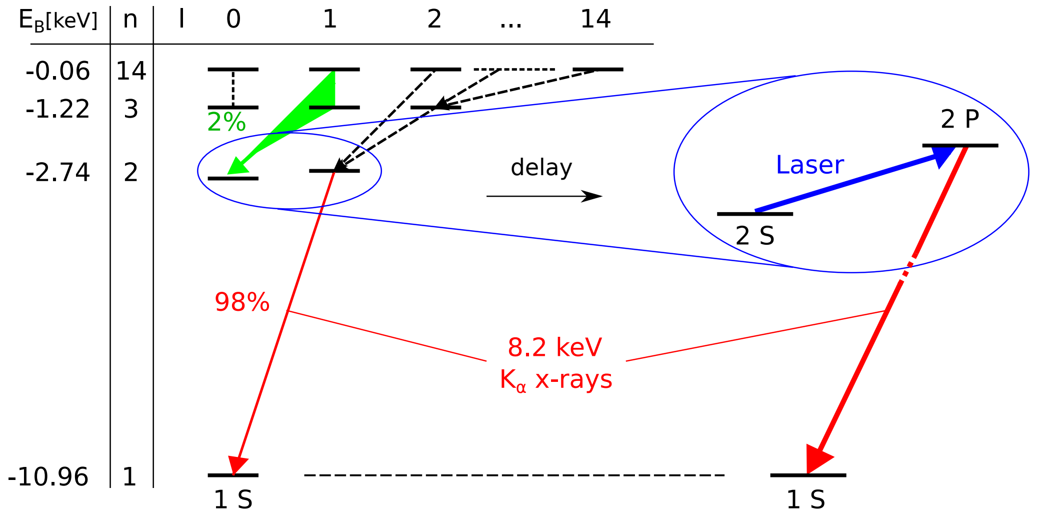

Figure 3.1: Atomic cascade and experimental principle. Left: Scheme of the atomic cascade taking place in muonic atoms and ions. Muons are captured in highly excited states around $n \sim 14$. From there, they cascade towards the ground state, undergoing radiative-, Coulomb- and Auger-transitions. Paths meeting the high-l-end of the spectrum (black arrows) end up in the $1S$ ground state and are lost for the experiment. Only roughly 2 % of all initial ions end up in the $2S$-state fed by Balmer transitions (green arrows) [70]. Right: Sketch of the experimental principle. Muonic ions in the $2S$-state are then transferred to the $2P$-state via laser excitation. From there they immediately decay to the ground state under the emission of a $\mathbf{K}_\alpha$ x-ray. This florescence is in time-coincidence with the laser and serves as signal.

The vacuum lifetime of surviving $2S$-states is limited on the one hand by the lifetime of the muon $\tau_\mu = 2.197\ \mu$s [71, 72] and on the other hand by the two-photon decay to the ground state $\lambda_{2\gamma} = 1.18 \cdot 10^5\ \mathrm{s}^{-1}$ [54]. In gaseous environments however, the lifetime is strongly influenced by quenching effects that scale with the surrounding gas pressure $\lambda_{quench} \sim 10^4\ \mathrm{s}^{-1}$ at a few hPa [51]. The $2S$-ions can be quenched by collisional Stark mixing of the $2S$ and $2P$ states followed by prompt emission of a $\mathbf{K}_\alpha$ x-ray [69]. To guarantee large enough surviving $2S$-populations for the delayed laser excitation, low gas pressures are therefore needed (e.g. 2 hPa for $\tau_{2S} = 1.71\ \mu$s, see App. C).

3.2 Realization of the Setup

To fulfill the needed experimental conditions in our setup, low energy muons with a few keV are led into a low pressure helium gas target operated at around 3 hPa. Before entering the target, the incoming muons are registered using a non-destructive detection scheme involving stacks of ultra-thin carbon foils. These foils emit detectable electrons upon muon pass-through, providing the trigger signal for the data acquisition (DAQ) and laser system.

Upon triggered, a frequency-doubled two stage Yb:YAG thin disk laser system is generating roughly 40 mJ of green light within a few hundred ns [73,74]. This is then used to pump a frequency-seeded Ti:Sa ring-oscillator that provides the actual light for the spectroscopy. After a passing roughly 20 m of laser beam line towards the apparatus in the experimental area, the laser enters the gas target where the muonic atoms have formed. In order to store the photons inside the target long enough to enable interaction with a muonic ion, a sophisticated multi-pass cavity is used, confining the light for about 100 ns [75]. If on resonance, the light drives one of the $2S - 2P$ transitions in the µHe-ion (see Fig. 3.1), and since $2P$-state has a lifetime of a 0.5 ps, it decays immediately under emission of an 8.2 keV $\mathbf{K}_\alpha$ x-ray [76].

These delayed $\mathbf{K}_\alpha$ x-rays constitute the resonance signal and are registered with a pair of detector arrays. Each consists out of 10 large area avalanche photodiodes (LAAPDs) [77–79], with each detector array covering about 15% of the solid angle around the muon stop volume. Once the muonic ion decayed to the ground state, it remains close to its origin in the gas target until the muon decays after a lifetime of 2.197 μs on average [71,72]. This decay happens under emission of an MeV electron that spirals in the magnetic field of a surrounding solenoidal magnet. To reduce background effects within the LAAPDs, muon decay electrons are additionally detected with plastic scintillators surrounding the gas target.

3.3 Low Energy Negative Muon Beamline

One of the initial hurdles for this kind of experiments was to stop muons in a low pressure gas target to obtain a long-surviving $2S$-population. To fulfill the corresponding requirement of muon kinetic energies in the low keV range, a specifically designed low-energy muon beam line was developed at PSI [80]. The schematic overview presented in Fig. 3.2 shows its three major parts: The so-called cyclotron trap (CT) [81] forms a magnetic bottle for incoming pions and muons. The muon extraction channel (MEC) serves as background and momentum filter. The phase space compressor (PSC) houses all the detectors and the low pressure helium target inside a 5 T solenoidal magnet.

Negatively charged, pions at $\sim$100 MeV/c with a momentum spread of a few percent are injected from the accelerator beam line into the upper parts of the cyclotron trap with a rate of roughly $10^8\,\mathrm{s}^{-1}$. The CT's main purpose is to slow down entering negative pions and their succeeding negative muon decay particles. A moderator composed of ceramics and plastic of a total thickness ($\rho = 5.4\,\mathrm{g/cm}^2$) is placed at the

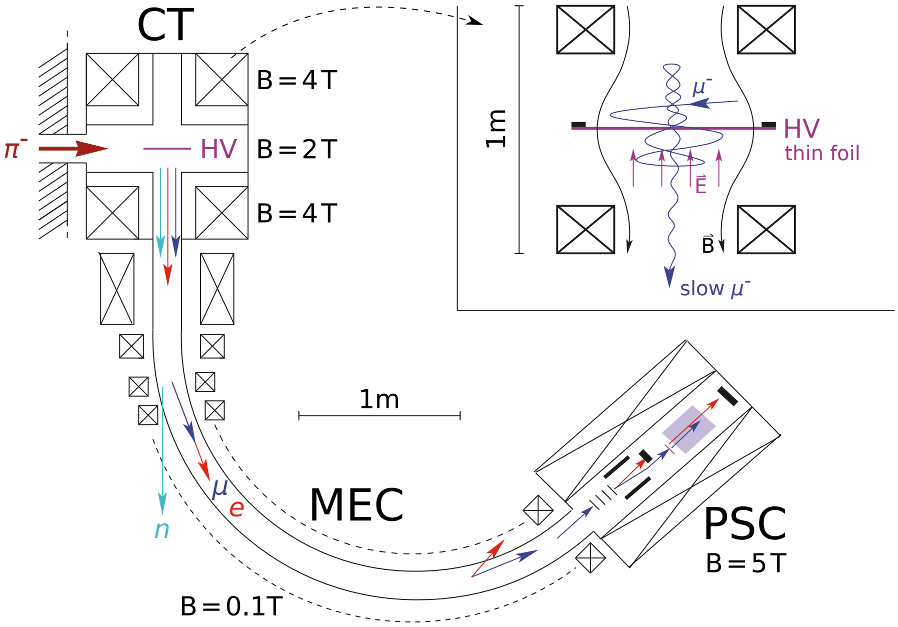

Figure 3.2: Scheme of the low energy muon beam line at PSI. The low energy muon beam line operated in the πE5 area at PSI consists of the cyclotron trap (CT), the muon extraction channel (MEC) and the phase space compressor (PSC; a $B = 5\,\mathrm{T}$ solenoid) [13]. Incoming pions from the accelerator beam line are slowed down by a moderator and successively stored in the CT. The negative muon resulting from pion decay is further slowed down by passing through a thin Formvar foil in the center of the CT (shown in the insert in the top right corner). Low energy muons are extracted with a static electric field and transferred towards the experiment via the MEC. Unwanted particles are discarded due to the momentum selection on the path through the MEC.

entrance of the CT and slows down the initial pions to roughly 50 MeV/c into a captured trajectory. The on-axis field measures 2 T in the middle of the CT and 4 T in the center of the coils, forming the needed field gradient for the bottle potential. 30 % of the initially entering pions are captured long enough to decay into μ^- with kinetic energies of a few MeV. The rest is lost inside the initial moderator during collisions or on impact with the metal walls of the CT.

Surviving decay muons are trapped in the magnetic potential, following helical trajectories around the center of the CT where they are axially and radially confined. A 160 nm Formvar foil in the middle of the trapping potential (shown in the insert of Fig. 3.2) is hit by the muons on each pass through along the longitudinal axis, leading to a continuous loss of kinetic energy. After roughly 100 passes, a high voltage of −20 kV (applied on the foil which is made conductive by a 3 nm thick Ni layer) pushes

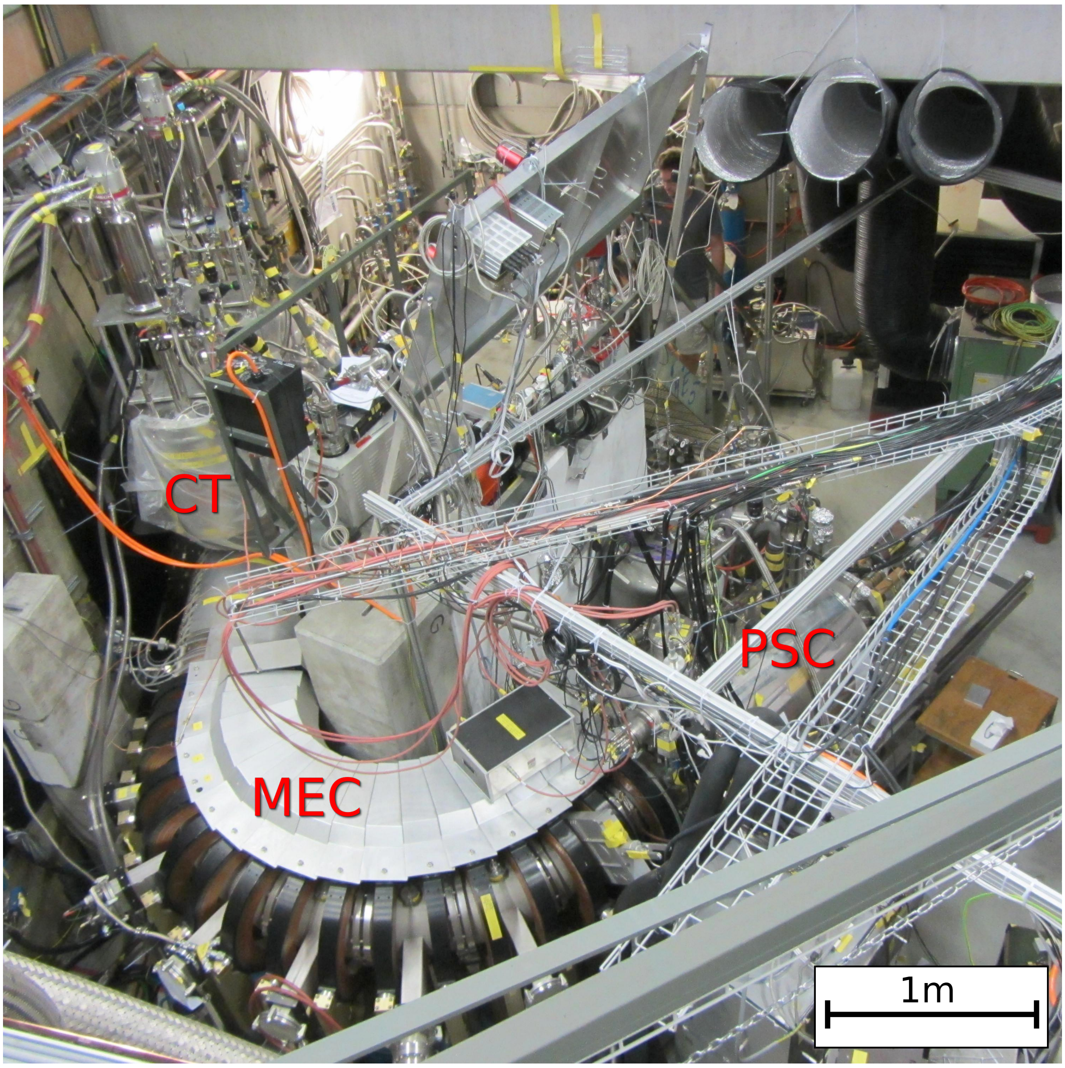

Figure 3.3: Photo of the experimental setup. Picture of the πE5 experimental area at PSI. In the top left corner the CT with its cryogenic cooling system can be seen. The connecting curved structure on the bottom are the coils of the MEC that serve as momentum filter. The right part below the cable trays is the PSC in which the gas target and detectors are located. In the Middle, on top of the concrete block, the helium circulation system is located feeding purified gas to the target inside the PSC.

the remaining 10-50 keV muons out of the magnetic bottle along the field axis [82]. Muons exiting on the unoccupied end of the CT are lost for the rest of the experiment.

Since low energy muons are not the only particles emitted from the CT, additional effort has to be taken to shield the detectors inside the PSC from unwanted background. This background includes neutrons created in pion collisions with the setup walls, high energy electrons from muon decay, as well as keV electrons ejected from the Formvar foil. Therefore a low-field solenoid (MED, B=0.15 T) is located on the left side of the CT, consisting out of 17 normal conducting coils. The created toroidal magnetic field is shaped with a horizontal gradient, forcing charged particles to experience vertical drifts due to different radii of gyration. This is used to separate charged particles with different momenta, discarding unwanted species by using beam blocks placed inside the MEC. Only muons with the desired energy are left for the experiment. A picture of the entire apparatus in the 2014 configuration can be seen in Fig. 3.3.

3.4 Target Volume and Detectors

From the MEC, the low energy muons transit into the 5 T magnetic field of the 1 m long PSC magnet. This increase in magnetic field strength ensures that the radius of the spiraling muon motion is shrunk from some centimeters inside the MEC, to a few mm inside the PSC. This drastically reduces the radial size of the muon stop volume, and consequently also reduces the volume that has to be illuminated by the laser. Since the bore of the solenoid itself is only 20 cm in diameter, the entire setup was realized in a very compact manner.

3.4.1 Incoming Muon Detection

Due to the small matrix elements in muonic helium (see Tab. 2.4), the laser fluence inside the gas target has to be high to get a sufficient excitation probability for the experiment. Continuous wave (CW) lasers are not able to fulfill this condition so that a pulsed laser has to be used for the spectroscopy. Triggering such a system would normally be realized with a constant repetition rate that is synchronized to the atom/ion source. This is however not possible in the CREMA experiments. The worldwide only place with pion beams of sufficiently high intensities is at PSI, whose proton accelerator operates in a quasi-CW regime (pulsed at 50 MHz) which is not suitable for laser synchronization in our case. This leads to a stochastic distribution of incoming particles in the gas target, so that triggering has to occur on each individual muon.

To provide a trigger signal for the experiment, the incoming keV muons are detected non-destructively while passing through two sets of charged steel rings, the so-called

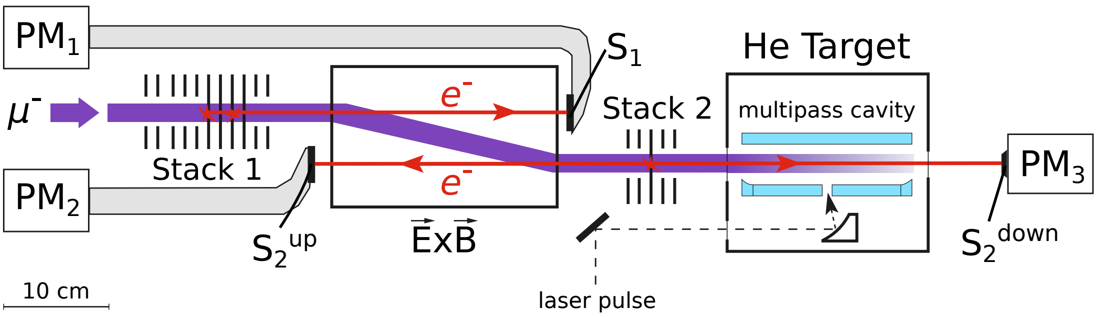

Figure 3.4: Incoming muon detection system. Picture describing the non-destructive detection scheme used as trigger for the laser system [13]. Potentials applied to Stack 1 and Stack 2 lead to longitudinal cooling of the incoming muon beam. Muons passing thin carbon foils located within the stacks expel secondary electrons from the foil that propagate in both the up- and downstream direction. These electrons are used to create a trigger signal for the experiment. An additional $\vec{E} \times \vec{B}$ filter separates the muon beam from the signal electrons before they are detected with scintillators (S1, $S2_{\mathrm{up}}$, and $S2_{\mathrm{down}}$) and the photomultiplier tubes (PM_1, PM_2, and PM_3).

stacks. Some of the rings are spanned with thin carbon foils ($d = 4\,\mu\mathrm{g/cm}$) to provide resistance for the passing muons.

While passing the carbon foils, the incoming muons expel electrons that are used as trigger signal for the experiment. These electrons are accelerated by the potential applied on the steel rings. An additional $\vec{E} \times \vec{B}$ velocity filter placed between both stacks separates these electrons from the negative muons, and shifts the μ^- roughly 8 mm downwards to the entrance window of the target. Since the fast keV electrons are quasi unaffected by the electric potential in the filter, they hit two plastic scintillators ("S_1" and "S_2^{up}") placed next to the muon beam path on both sides of the $\vec{E} \times \vec{B}$ filter. These scintillators are read out via light guide and photomultiplier tubes.

An additional scintillator & photomultiplier combination is placed along the shifted muon beam axis, 10 cm behind the gas target ("S_2^{down}"). This detector catches additional electrons emitted by the second stack in forward direction. The signal efficiency for all scintillators is increased by applying a positive high voltage on a wire-cage in front of the scintillators to accelerate the electrons before the impact. A scheme of the entire muon detection apparatus is seen in Fig. 3.4.

For initial alignment procedures of the setup, Stack 1 can be replaced by a separate scintillator that is read out via a Geiger-mode avalanche photo diode. This detector is directly sensitive to the muons coming from the MEC and has a bigger area of acceptance than the normally used detectors. The new detector was successfully used in the end of the 2014 beam time to measure positive muons that were created inside the CT under altered experimental conditions.

3.4.2 Gas Target and Circulation System

Once the muon passed the non-destructive detection system to provide a trigger, it arrives in the gas-filled target volume near the end of the solenoid. Here, collisional processes with the surrounding helium atoms slow down the incoming muon further, before the muon is eventually captured and forms a muonic ion.

The target itself consists out of an 8 mm strong aluminum casing that provides mounts for the multi-pass laser cavity and its diagnostics system on the inside, and for the x-ray and electron detectors on the outside. Along the muon beam axis, two $5 \times 12\,\mathrm{mm}^2$ openings allow the entrance of muons and electrons on the upstream end, as well as the downstream exit of electrons created by Stack 2 that travel downstream. In order to keep the needed gas pressure of 1-3 hPa in the target volume, two ultra-thin Formvar foils seal the entrance and exit openings, while only weakly interacting with the passing muons and electrons.

For the second beam time in 2014 the possibility to mount an additional second set of matching entrance and exit windows was realized, together with a differential pumping scheme. This system was conceived in case the target tightness was not sufficient to perform the $\mu^3\mathrm{He}^+$ experiment. In the actual data taking runs this was not installed since the target was found to be sufficiently tight and no additional measures were necessary to avoid losses of the rare isotope.

On top and bottom of the $5{\times}12{\times}190\,\mathrm{mm}^3$ big muon stop volume, two 1 µm thin polypropylene foils are mounted, coated with a 700 nm layer of aluminum on both sides. These foils allow the transmission of x-rays to the detectors placed on the outside, while shielding the x-ray detectors from scattered laser light inside the multi-pass cavity.

The gas on the inside has to be kept as pure as possible in order to avoid quenching of the $2S$-state in collisions with higher mass elements [69]. This was achieved by continuously flushing the target with fresh and clean helium gas. In the 2013 measurement campaign, a ^{4}He gas bottle was connected to the inlet of the apparatus while the exhaust was directly removed by pumping on the other end. Even though the waste of multiple bar·l of gas per day by this procedure is acceptable for the readily available ^{4}He, the ^{3}He needed for the second part of the experiment is rare and expensive. An

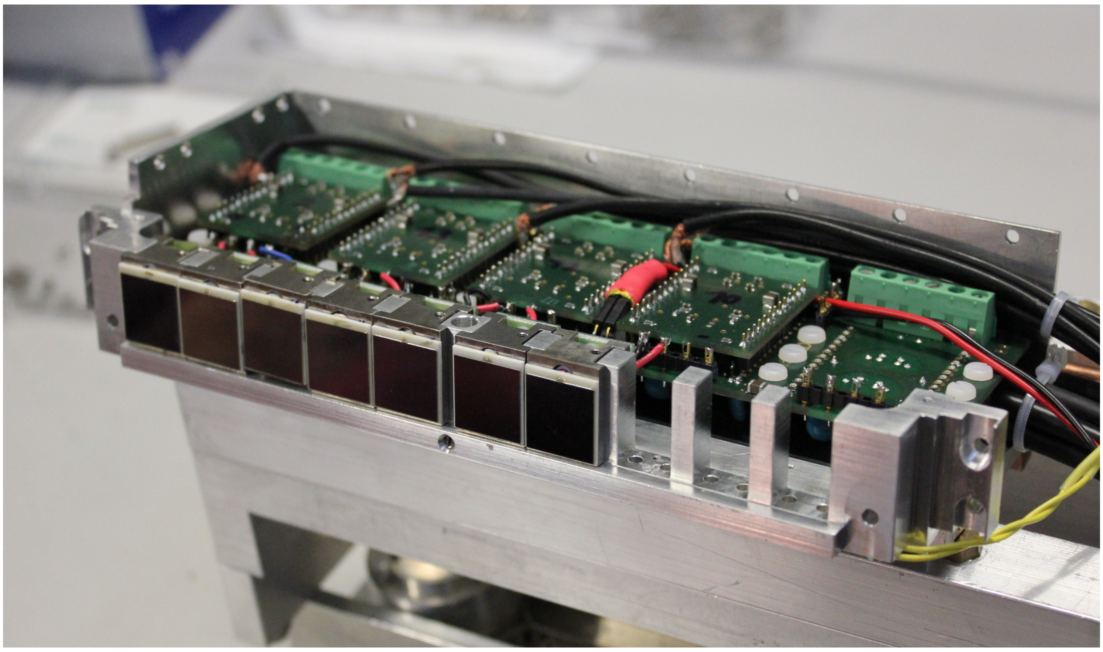

Figure 3.5: Photo of partially assembled LAAPD array. Top mounted (A-side) x-ray detector array used during the 2014 beam time in the muonic helium Lamb shift experiment. Three APDs are currently being replaced in the picture. Each diode is mounted on a separate titanium piece for easy removal and efficient cooling. On the back side, custom built charge sensitive preamplifiers are mounted to increase the recorded signal strength. Signal and voltage cables on the right side lead towards the upstream part of the experiment where they leave the vacuum vessel.

alternate solution, using a closed gas circulation system, was therefore implemented for the entire 2014 data taking run. To guarantee cleanliness, a liquid helium cold trap was used to purify the gas in flow. Since there were still minor losses through the muon entrance and exit windows the gas pressure inside the system had to be adjusted once the pressure in the target dropped below 2.5 hPa. The overall loss of ^{3}He-gas through the entire one-month long measurement campaign was below 5 bar·l in total.

3.4.3 X-ray Detectors

In order to measure the resonance signal from the laser induced $2S - 2P$ transition, a set of x-ray detectors is placed on the outside of the gas target. Muonic x-rays are detected by twenty large area avalanche photo diodes (LAAPDs) with an active area of $14{\times}14\,\mathrm{mm}^2$ each [77, 78]. A picture of one APD array can be seen in Fig. 3.5 . APDs are silicon solid state detectors with the ability to convert photons into a free charge current [83]. The initial photon conversion takes place in the depletion region on the active surface of the APD (see Fig. A.1 in App. A). In this low voltage p-doped

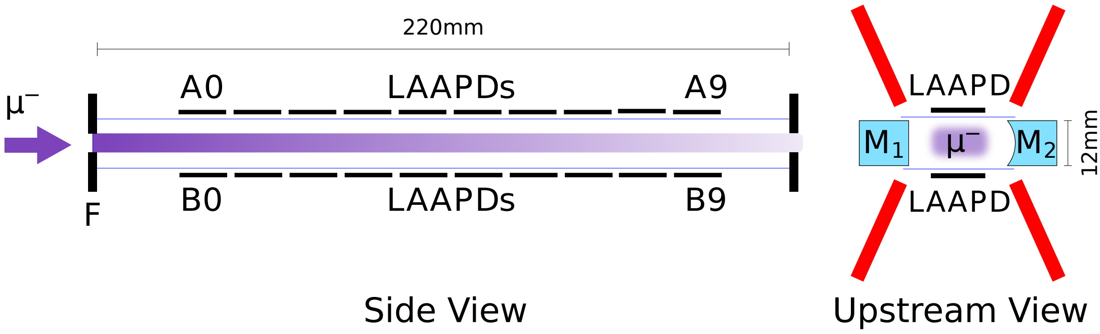

Figure 3.6: Detector geometry around the gas target. Scheme showing the different detectors around the gas target [13]. Two arrays of ten LAAPDs each are mounted above and below the target to detect muonic x-rays. Four additional plastic scintillator paddles are placed in an x-shape (red in the figure) to detect muon decay electrons spiraling in the magnetic field.

area, the absorption length of entering photons varies with their respective energy, affecting the detectors efficiency and energy linearity. Differences in thickness of this absorption layer give rise to sensitive changes in detector energy acceptance. A high bias p-n junction is placed on the back side of the active volume to provide additional gain for the converted photo electrons. In this avalanche region electron impact ionization leads to a multiplication of free charge carriers increasing the signal output [83]. More information on the used APDs and their working principle is provided in App. A.

Two detector arrays consisting out of ten APDs from the manufacturer *Radiation Monitoring Devices* are mounted on top and on bottom of the muon stop volume in a face-to-face manner (see Fig. 3.6). Their distance from the muon beam center measures 8 mm in order to maximize the available detection solid angle. Custom built charge sensitive pre-amplifiers are mounted directly on the back side of the APDs to increase the recorded signal strength. Both detector arrays are cooled by an external ethanol circulation system, and actively temperature stabilized to $-30°$ C to achieve the optimal gain and energy resolution. Measured energy resolutions for 8.2 keV $\mu^4\text{He}^+$ $\mathbf{K}_\alpha$ x-rays were around 16% full width half maximum (FWHM) on average [79]. The used bias voltage for the different APDs varied between 1700 V and 1760 V to achieve similar gain for all detectors. After leaving the vacuum vessel, the measured signals are further amplified by gain 2 linear post-amplifiers, before being recorded in different channels of CAEN V1720 waveform digitizers (WFDs). The APDs themselves are labeled with A0 – A9 on the top side, and B0 – B9 on the bottom, A0/B0 being the most upstream detectors.

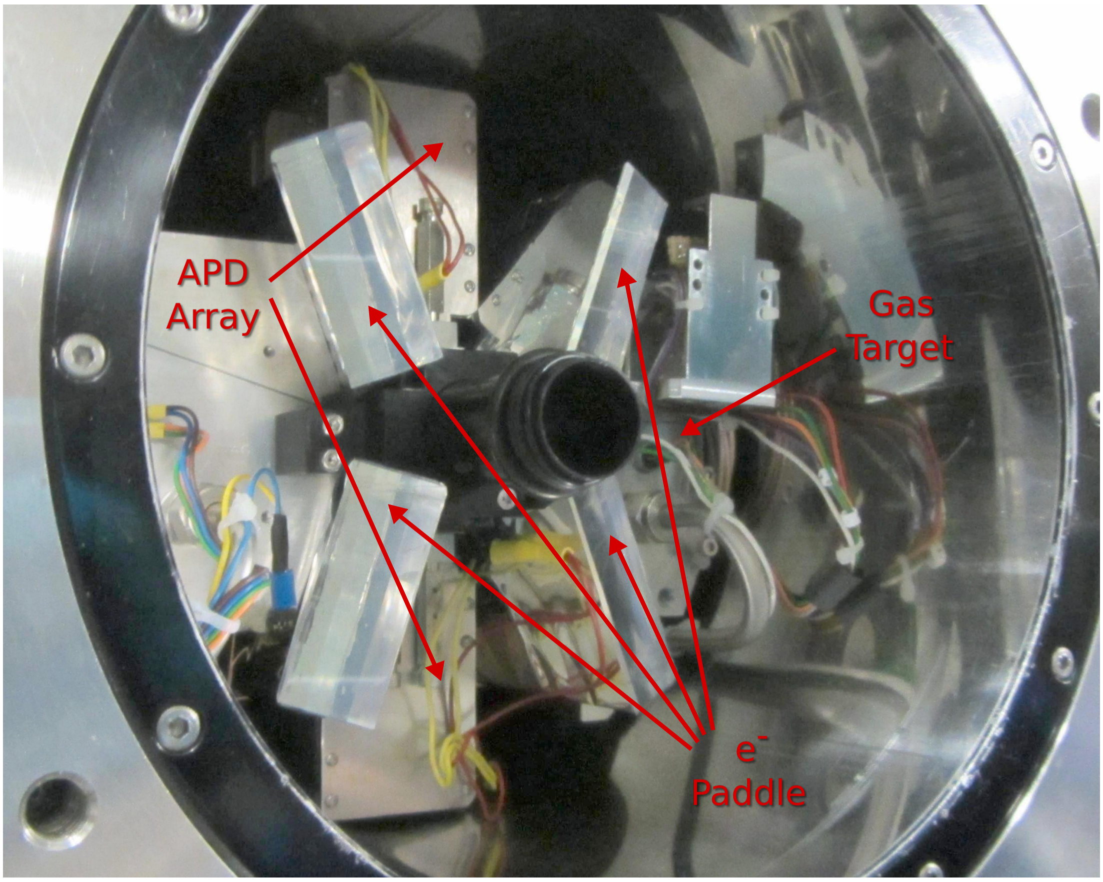

Figure 3.7: Photo of the PSC interior. View in upstream direction into the PSC. The gas target is visible together with the different mounted detectors. Centered above and below the gas target both APD arrays are visible (with mounted preamplifiers). The four scintillator paddles forming an X-shape along the muon beam axis are used for muon decay electron detection and identification.

3.4.4 Electron Detectors

The main source of background for the spectroscopy experiment stems from MeV muon decay electrons depositing energy in the APDs on pass-through. To reduce this effect in the offline analysis, electrons are also registered by four surrounding plastic scintillator paddles. This allows the identification of electron signals in order to apply background reducing cuts, described in Sec. 4.2. The electron detectors form an X-shape around the targets central axis, as can be seen in Fig. 3.6 and Fig. 3.7. They are read out via light guide and photomultiplier tubes located on the downstream part of the setup. Both scintillators on the left and right side, are connected to one photomultiplier and are denoted with $\mathrm{E}^{\mathrm{left/right}}$ respectively. The respective signals pass four differently scaled discriminator thresholds and the corresponding signal timings are recorded in channels of a CAEN 767 multi-hit time to digital converter (TDC). They are tagged with $\mathrm{E}^{\mathrm{left/right}}_{\mathrm{low/m1/m2/hi}}$ for further use in the analysis, depending on the registered amplitude.

During data taking, an issue in the used CAEN 767 TDCs was observed, leading to a saturation of the internal processing chips, when the signal rate was too high. The gate length for the high rate signals $\mathrm{E}^{\mathrm{left/right}}_{\mathrm{low/m1}}$ was increased compared to signals of the higher thresholds to avoid chip saturation. The low rate signals $\mathrm{E}^{\mathrm{left/right}}_{\mathrm{m2}}$ were separately recorded with another chip, to have a certain degree of redundancy. Additionally an appropriately scaled sum of all the $\mathrm{E}^{\mathrm{left}}$ and $\mathrm{E}^{\mathrm{right}}$ gate signals was recorded in a CAEN 1720 wave form digitizer (WFD) during the $\mu^3\mathrm{He}^+$ data taking in 2014.

3.5 Laser System

In order to drive the $2S{-}2P$ transitions in $\mu^4\mathrm{He}^+$ and $\mu^3\mathrm{He}^+$, laser wavelengths between 800 nm and 1100 nm are required, corresponding to frequencies between 347.7 THz and 272.5 THz, respectively (see Tab. 2.4). To cover this large range of optical transitions, a widely tunable laser system is required. In theory, the emission spectrum of a Titan-Sapphire (Ti:Sa) crystal spans the range between 600 nm and 1100 nm, making it ideally suited for the experiment [84]. Our laser system implementation provided excellent wavelength tunability between 800 nm and 970 nm, allowing the measurement of all µHe transitions except for $2S^{F=0}_{1/2} - 2P^{F=1}_{1/2}$ without significant modifications. The Ti:Sa system also showed very good long term stability and reliability that had to be guaranteed for continuous time spans up to months of active operation.

To measure all the accessible transitions with roughly one third of their saturation intensity, a laser fluence of $2\,\mathrm{J/cm^2}$ is required [2] (see also Tab. 2.4). These high fluence requirements are a direct consequence of the low matrix elements in the muonic helium transitions. Even though the used multi-pass cavity provides significant enhancement, these values correspond to a Ti:Sa output pulse energy of up to ~14 mJ for our setup [2]. The laser was able to provide this high output reliably even though it was mostly operated at lower values in order to avoid damage on the cavity mirrors.

Another important requirement the laser system successfully met is the provision of the required optical power with a repetition rate of 500 Hz on statistically distributed triggers. With lower repetition rates many events suited for spectroscopy would be lost during intervals where the laser system is not ready to fire. Additionally, the timing delay between laser trigger and pulse arrival in the target cavity had to be comparable to the lifetime of the $2S$ state in the µHe isotopes (~1 µs) to successfully drive the transition with a sufficient rate.

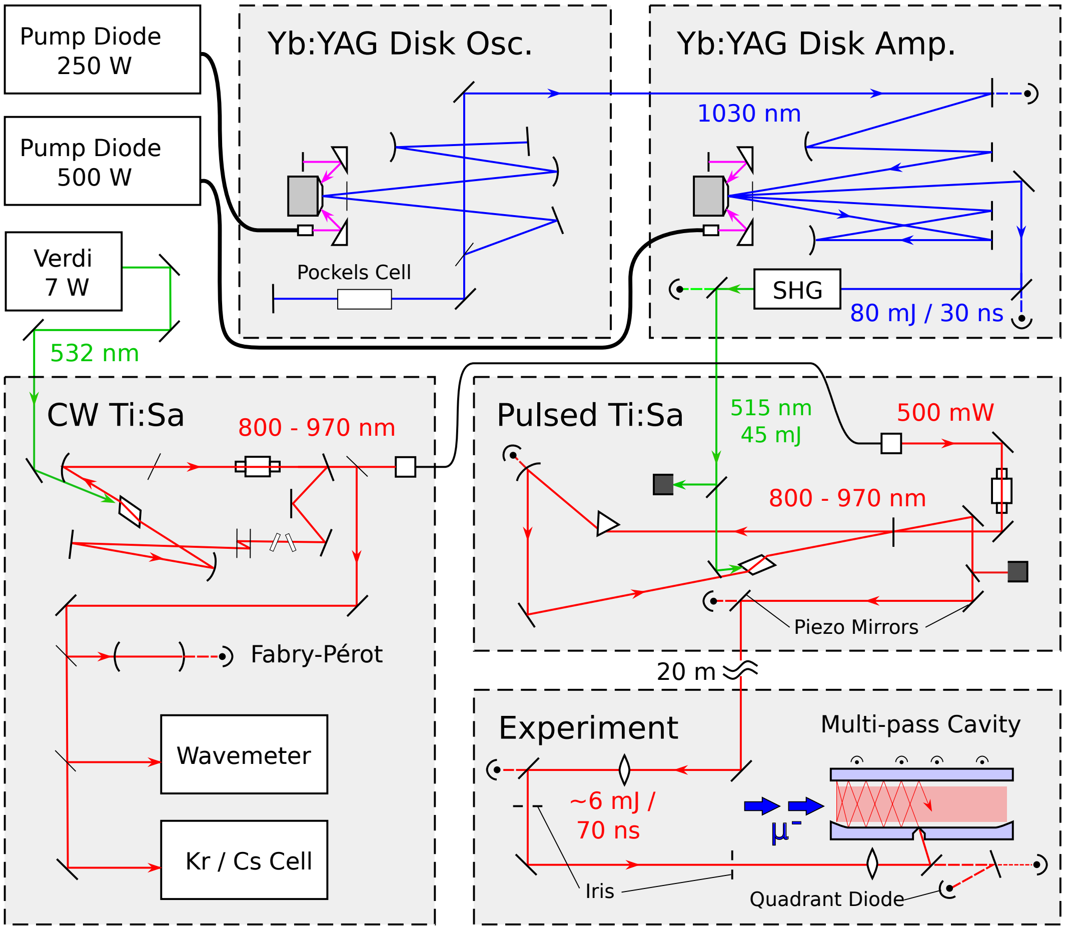
Pump Diode 250 W
Pump Diode 500 W
Verdi 7 W
532 nm
Yb:YAG Disk Osc.
Pockels Cell
Yb:YAG Disk Amp.
1030 nm
SHG
80 mJ / 30 ns
CW Ti:Sa
800 - 970 nm
Fabry-Pérot
Wavemeter
Kr / Cs Cell
Pulsed Ti:Sa
515 nm
45 mJ
500 mW
800 - 970 nm
Piezo Mirrors
20 m
Experiment
Multi-pass Cavity
~6 mJ /
70 ns
μ^-
Iris
Quadrant Diode

Figure 3.8: Laser system schematic. The pump light for the pulsed spectroscopy laser is generated by a two-stage Ytterbium-YAG (Yb:YAG) thin disk laser system. A Q-switched oscillator provides pump pulses with a delay of $\sim$250 ns that are further amplified in a multi-pass amplifier. The light required for the spectroscopy is provided by an injection seeded Titan:Sapphire (Ti:Sa) ring laser. The laser cavity is locked to the wavelength that is provided by another highly stable continuous wave (CW) Ti:Sa ring laser. The CW laser is itself stabilized to a temperature-controlled Fabry-Pérot cavity, and additional stabilization is done via wavemeter readout in a servo loop. The Ti:Sa spectroscopy light is propagated to the experiment via a 20 m long beam line before it enters the non-resonant multi-pass cavity illuminating the muon stop volume.

An overview of used laser system is given in Fig. 3.8. The first component is a two-stage Ytterbium-YAG (Yb:YAG) thin disk laser system. It consists out of an oscillator and a 12-pass amplifier setup that provides up to 145 mJ of 1030 nm infrared light per pulse [73, 74]. Second harmonic generation (SHG) in a lithium triborate (LBO) crystal was used to produce 515 nm green light with 55 % efficiency. This light is used to pump a pulsed Ti:Sa ring oscillator that provides up to 10 mJ of output pulse energy. The emission frequency of the pulsed Ti:Sa is given by an actively stabilized continuous wave (CW) Ti:Sa laser that is seeding the pulsed Ti:Sa ring oscillator. The CW laser itself is locked to a temperature-controlled high finesse Fabry-Pérot cavity as reference, while its frequency is continuously measured by three independent wave meters. Calibration of the setup was done by performing saturated absorption spectroscopy of lines in Cesium and Krypton (see Sec. 5.3.3) and with a calibrated High Finesse wavemeter.

The pulsed light provided by the Ti:Sa system is transferred via a 20 m long evacuated beam line over to the main part of the experiment inside the PSC. There, a non-resonant multi-pass cavity illuminates the muon stop volume with a confinement time of roughly 100 ns [75]. Upon entrance in the target, the light is focused through a 630 µm diameter hole in the center of one of the cavity mirror substrates. After a few 100 successive reflections the light is more or less evenly distributed inside the volume due to the angular divergence of the in-coupled beam. PIN-photodiodes placed behind the cylindrical mirror monitor the fluence distribution inside the cavity at all times and are used for laser energy calibration (see Sec. 3.5.4).

3.5.1 Thin Disk Laser Setup

The pulsed laser system is pumped by an upgraded version of the Yb:YAG thin disk laser unit that was successfully used in the muonic hydrogen Lamb shift experiment [85]. In the µHe experiment, an improved design provided a factor of three more pulse energy at 1030 nm than the one used in the previous setup [74]. During the experiment it was operated at lower output to avoid damage to the second harmonic generation crystal. This overall increase in performance was made possible by improved thermal contacting of disk and heat sink as well as by pumping the Yb:YAG crystal on the zero-phonon line, leading to a significant decrease in waste heat production [86].

The disk laser setup consists out of two main components: A Q-switched master oscillator and a multi-pass amplifier. The key part used in both systems is the disk-laser technology [87]. A 0.2 mm thick disk of gain material (Yb:YAG) is optically bonded to a water cooled diamond surface. The thin profile together with the direct connection to the heat sink reduces heating effects significantly. This in turn increases the effective

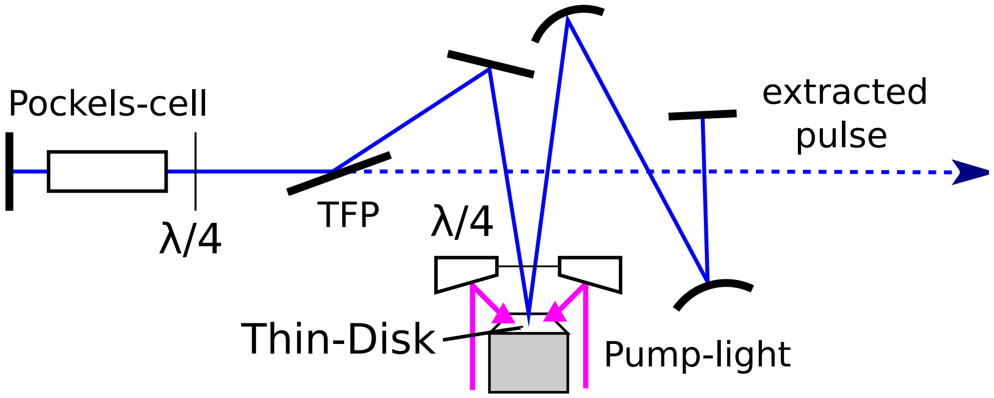

Figure 3.9: Disk oscillator working principle. Scheme of the disk oscillator used to pump the laser system [13]. A Pockels-cell with a wave plate and thin film polarizer is used to Q-switch the system and to close/open the cavity for pulse buildup and extraction. When not triggered, the laser is operated in CW pre-lasing mode.

damage threshold of the crystal and helps avoiding thermal lensing effects and accompanied phase distortions. In order to be able to form a laser cavity perpendicular to the disk surface and to allow for efficient pumping, the disks back side is coated with a high reflectivity coating (HR) for both pump and emitted light at 940 nm and 1030 nm, respectively. The pump light used for the oscillator is provided by CW-operated commercial laser diodes and is reflected onto the disk twelve times in order to maximize efficiency.

Q-switching the oscillator is realized using a Pockels-cell (PC) consisting out of a barium beta borate (BBO) crystal and kV-electrodes. The PC can change the intra cavity polarization using the Pockels effect in the birefringent crystal on a ns time scale. A thin film polarizer (TFP) together with a $\lambda/4$–plate can either act as cavity closing mirror, or as output coupler for the transmitted light, depending on the polarization setting of the PC. The cavity measures 1 m in length, passing the gain medium inside the thin disk effectively four times. An additional $\lambda/4$–plate is placed directly in front of the gain medium to circularize the polarization near the disk. This avoids interference between incoming and outgoing beams since the reflection on the disk reverses the polarization of the reflected beam compared to the incoming light. A scheme of the working principle of the disk laser system is shown in Fig. 3.9.

The disk laser is operated in “CW pre-lasing mode” where a few W of CW light circulate within the cavity and 250 W of 940 nm pump light constantly illuminating the disk. When a muon trigger is received, the cavity is closed by applying a 4 kV high voltage on one PC electrode to allow for intra cavity energy build up. This mode of

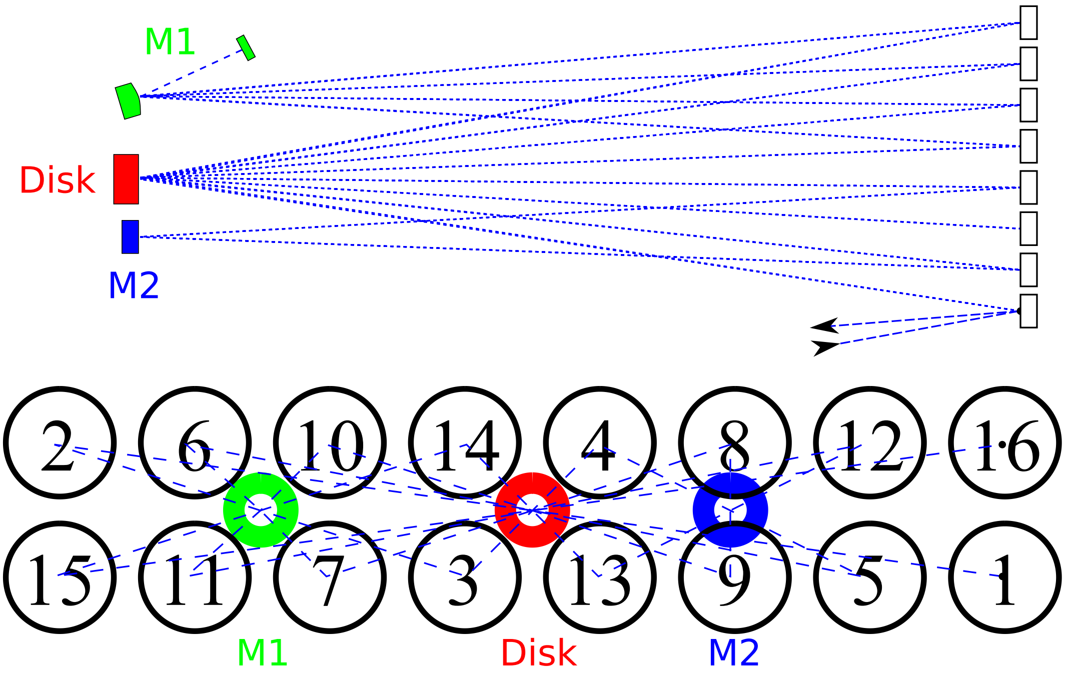

Figure 3.10: Disk multi-pass amplifier. Scheme illustrating the mirror array in the multi-pass disk laser amplifier (top and side view) [13]. The numbers indicate the sequence in which the mirrors are hit by the laser beam. The light path (blue dashed line) passes the curved mirrors (M1 & M2) and the disk multiple times while maintaining a stable beam profile each pass.

operation has a high number of photons circulating in the cavity at all times, leading to very short 250 ns delay upon triggering. Each round trip inside the cavity corresponds to a measured gain factor of 1.52 (1.25 per disk reflexion) and the extracted pulses have a duration of 30 ns. After the 250 ns the cavity is opened by applying high voltage on the second electrode of the PC. The circulating light pulse is then transmitted through the TFP towards the amplifier. The oscillator needs roughly 1 ms to reach the required initial inversion again, satisfying the repetition rate requirement of <500 Hz.

The disk oscillator is operated at only relatively low output energies in order to avoid damage to its optical components. To compensate for this an additional multi-pass amplifier system is implemented to reach the required total pulse energy [74]. The integration of the active medium is realized in the same manner as in the oscillator: A back-reflecting thin Yb:YAG disk pumped by 500 W of 940 nm light from another commercial diode laser. A set of intrinsically stable optical paths is realized by using a curved mirror (M1), a flat mirror (M2) and the disk itself (see Fig. 3.10). The distance of 3.2 m between mirror M1 and and the disk forms a Galilean telescope that is equivalent to a free propagation distance of 11m. An additional array of 16 mirrors allows

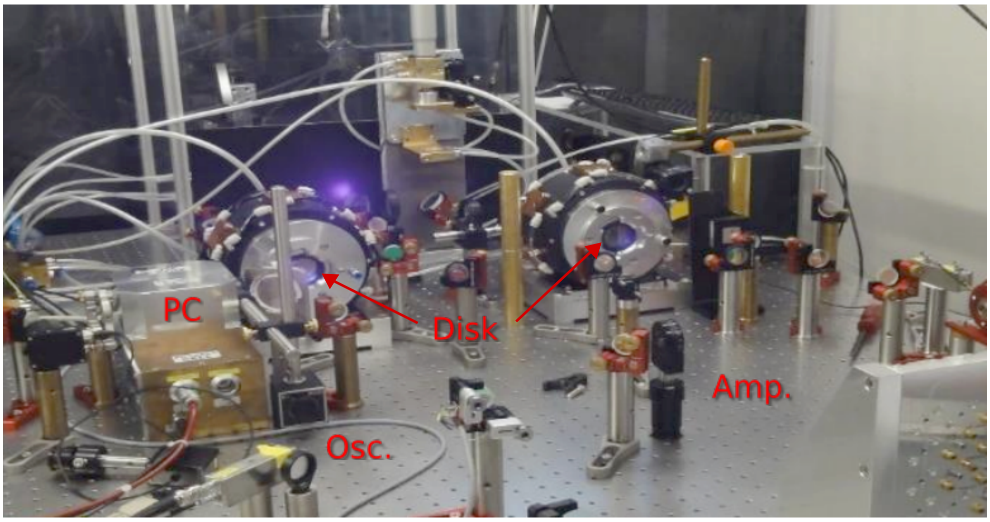

Figure 3.11: Photo of the disk laser system. Photo of the used Yb:YAG disk oscillator (Osc) and amplifier (Amp) [13]. Thin Yb:YAG disks and pump optics are housed in the cylindrical boxes in the back of the picture. The oscillator on the left side is Q-switched by a Pockels-cell (brown box, PC) to produce laser pulses. The light is then propagated to the multi-pass amplifier on the right side. The back side of the multi-pass amplifiers mirror array is visible in the lower right corner.

for the repeated usage of the optical elements to create a compact and stable 12-pass amplifier setup. Each round trip between both end mirrors has the same beam profile, facilitating a constant laser mode size inside the gain medium independent of its focal power. This removes damage threshold critical effects in the crystal which could otherwise be created by thermal lensing. The gain of the amplifier setup was measured to be 3.2 (1.16 per pass) and the the total time delay of the oscillator-amplifier combination was measured to be around 500 ns.

The infrared output of the setup is then frequency doubled to 515 nm within a water cooled LBO crystal (efficiency of 55 %). This light is then used to pump the pulsed Ti:Sa oscillator that provides the spectroscopy light at wavelengths between 800 nm and 970 nm. A picture of the disk oscillator-amplifier setup can be seen in Fig. 3.11.

3.5.2 Ti:Sa Laser System

The light used for the spectroscopy on µHe is created by a two stage Ti:Sa laser. A widely tunable CW ring laser pumped with 7 W of green light from a commercial neodymium-doped yttrium ortho-vanadate (Nd:YVO4) diode laser is used to produce seed light of the required wavelengths between 800 nm and 1000 nm [84]. The majority of the emitted light is transferred to a pulsed ring laser to serve as seed for stimulated emission and as reference on which the pulsed cavity is stabilized. A small part of the CW light is branched off to a temperature stabilized Fabry-Pérot cavity with a free spectral range of 1.497 GHz that serves as reference for the CW laser frequency (details in Sec. 5.3.3). During the 2013 and 2014 data taking runs, the pulsed ring laser cavity consisted out of a flat mirror, a curved mirror, a wavelength selective BK7 dispersive prism, and a flat output couplers. Different output couplers with reflectivities between 60 % and 90 % were used depending on the desired wavelength range. The pulsed oscillator cavity was lengthened once in 2014 from 3 m to 4 m to provide increased stability in the wavelength range required for the spectroscopy of the $\mu^3\mathrm{He}^+$ transitions (850 nm to 960 nm). Additionally, this served to increase the pulse duration to avoid damage threshold related problems at higher pulse energies. These higher energies were needed due to the smaller excitation probabilities in $\mu^3\mathrm{He}^+$ compared to the $2S_{1/2} - 2P_{3/2}$ transition in $\mu^4\mathrm{He}^+$ (see Tab. 2.4).

During normal operation, green pulses of up to 45 mJ were used to pump the Ti:Sa crystal, leading to an average output energy between 3 mJ and 10 mJ depending on the wavelength. The pulse durations were measured to be 70 ns and 90 ns for the short and long cavity setup, respectively. Since the oscillator provided enough pulse energy for the experiment, no additional amplifier was needed (in contrast to the 2009 experiment [1]). The laser beam passes some final steering and shaping optics before entering the vacuum chamber inside the solenoid (PSC).

3.5.3 Non-resonant Multi-pass Cavity

Inside the PSC, the incoming light is guided towards the helium gas target where it is injected into a non-resonant multi-pass cavity [75]. This cavity serves as a means to illuminate the pencil shaped muon stop volume and to drive the spectroscopic transitions in µHe. It consists out of two 190 mm long mirrors placed alongside the muon stop volume with a spacing of 25 mm. One mirror is of cylindrical shape with a radius of curvature $R = 110\,\mathrm{mm}$ that takes care of vertical light confinement. Since the radius of curvature is no multiple of the mirror spacing, recurring spot patterns are avoided. The second mirror features a mostly flat shape except for cylindrical end caps ($R = 100\,\mathrm{mm}$) placed on the up and downstream part of the mirror. To achieve this geometry, it was assembled manually out of the three individual parts that were screwed together and glued with ultra high vacuum compatible epoxy glue (Epotek 353ND). This assembly confines the light horizontally by retro-reflecting the beam on both ends. The flat mirror part features a centered 0.63 mm diameter hole on the optical surface that serves as injection point for the incoming laser radiation. The hole diameter on the mirror backside is increased in multiple steps to allow for the required in-coupling angles of $\sim 50\,\mathrm{mrad}$. Fig. 3.12 shows the layout and working principle of the target cavity.

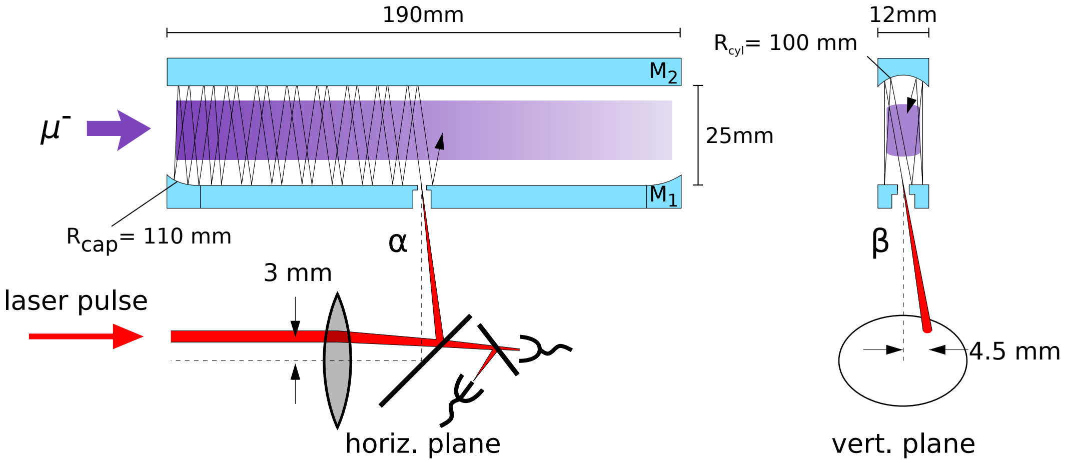

Figure 3.12: Principle of the multi-pass cavity. Scheme visualizing the in-coupling of light into the multi-pass cavity as used in 2014 [13]. The multi-pass cavity itself consist out of two 190 mm long mirrors. A focusing optical element is used to inject the light through the 0.63 mm large hole in one of the mirrors. The cylindrical mirror (top) creates vertical confinement for the incoming laser beam while the end caps of the flat mirror (bottom) create horizontal confinement. Injection under a finite angle in horizontal and vertical direction is used to illuminate the enclosed volume appropriately for the experiment.

Both mirrors are coated with a high quality broadband dielectric coating ($R = 99.98\%$ between 800 nm and 1000 nm, provided by Advanced Thin Films) to achieve the highest possible confinement time inside the cavity. Including the losses from the entrance hole and seams on the flat mirror substrate, the lifetime of the stored light for the initial cavity mirrors set was measured to be around 70 ns. For the measurements of the $2S_{1/2}^{F=0} - 2P_{3/2}^{F=1}$ and $2S_{1/2}^{F=1} - 2P_{1/2}^{F=1}$ transitions in $\mu^3\mathrm{He}^+$, new cavity mirrors were produced, featuring dielectric coating with a more narrow wavelength range that provided an increased lifetime of 110 ns (corresponds to roughly 1300 reflections; coating by Layertec).

The laser light is focused through the injection hole. During the 2013 measurement campaign, this was done by using a $f = 50.8$ mm gold coated off-axis parabolic mirror placed just before the entrance hole. Assuming an incoming parallel beam, this leads to a desired spot size of $\omega = 0.1$ mm at the injection point with the added feature of being insensitive to parallel shifts of the incoming laser beam. The total coupling efficiency through the injection hole was measured to be 95 %. In order to illuminate the muon stop volume optimally, the spot position on the parabolic mirror is shifted 3 mm vertically and 2 mm horizontally (for the 2013 setup). This leads to an even distribution of light inside the cavity with a total height of 6.5 mm.

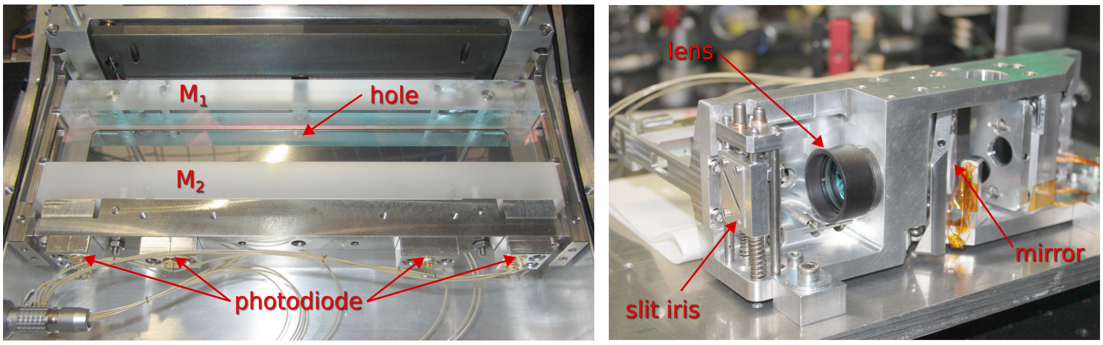

Figure 3.13: The non-resonant multi-pass cavity. Left: multi-pass cavity installed in the gas target together with its fluence monitoring system. The muon beam axis passes in horizontal direction between both mirrors. Right: New in-coupling optomechanics for the cavity with additional detectors. The slit-shaped irises in front of the in-coupling lens guarantee that the laser is only able to pass under correct alignment conditions in order to avoid damage to the cavity mirrors.

The laser power was increased in the end of 2013 to study additional systematic effects and the lifetime of the $2S$-state in $\mu^4\mathrm{He}^+$. Hereby the off-axis parabolic mirror was significantly damaged. The injection scheme was discarded for the 2014 data taking run and an anti reflective (AR) coated lens ($f = 75\,\mathrm{mm}$) together with a high reflective (HR) mirror was used to avoid further damage threshold related problems (Fig. 3.12). This method featured the same principle characteristics as the off-axis parabolic mirror method with more degrees of freedom. Slit irises in front of the coupling mirror provided additional safety against possible damage from beam-poiting drifts. A picture of the new in-coupling system is shown in Fig. 3.13.

3.5.4 Laser Monitoring and Pointing Stabilization

In order to be able to reduce laser power fluctuations, a number of provisions were realized in the setup. The first was implemented by externally stabilizing the beam path between the laser and the experiment. A commercial 4D beam pointing stabilization system by *TEM-Messtechnik* was installed to make sure that no significant angular and position changes of the laser beam occur in the 20 m long path between the Ti:Sa laser and the experimental setup. Position sensitive quadrant photo diodes were placed directly after the pulsed Ti:Sa laser oscillator and near the entrance of the vacuum chamber to monitor the beam drift. Two piezo driven mirrors placed in the beam path were used to correct the pointing, depending on the offset signal recorded from the position sensitive detectors. The average short term pointing drift of the laser could be reduced by more than a factor of two using this scheme.

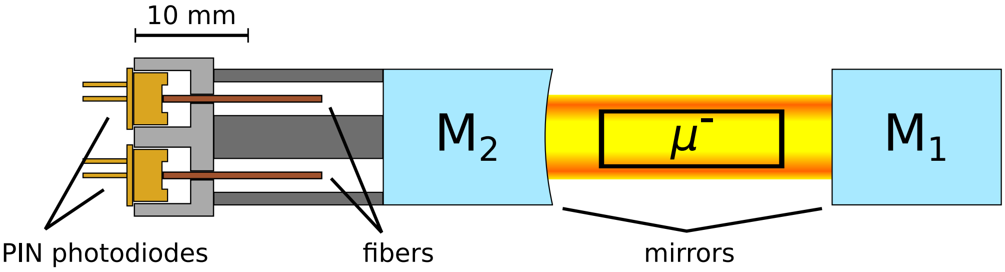

Figure 3.14: Cavity fluence monitoring. Scheme showing the working principle of the installed fluence monitoring system for the non-resonant multi-pass cavity [88]. In total six photodiodes are placed behind the curved mirror M_2 to observe the light distribution inside the cavity. Optical fibers limit the angle of incidence in front of the diodes to be more sensitive to small misalignments of the cavity. The diodes are placed in such a way that they are most sensitive to the local fluence maxima on the top and bottom edges of the illuminated volume.

Another important upgrade to the setup with regard to the laser power monitoring was the active measurement of the intra cavity fluence with a newly developed photo diode detector system (shown in Fig. 3.14). The idea behind the new monitoring system was to measure the transmitted light intensity through the coating of the cylindrical mirror at selected points of the light distribution in the cavity. This allows to deduce the alignment state of the cavity at all times without requiring manual intervention. As can be seen in Fig. 3.15, the light distribution inside the target cavity has distinct maxima in the vertical direction on the edge of the overall light distribution. These high-field areas are very sensitive to misalignment since even minor changes in mirror angle will significantly shift them vertically. Two photo diodes were placed on both the up- and downstream side, monitoring the top and bottom maxima. Since normal PIN-photodiodes have a large acceptance angle, drastically limiting the resolution of the position measurement, optical multi-mode fibers with a length of 20 mm and a diameter of 0.4 mm were placed in front of the detectors. The rest of the detector surface was shielded to limit the angle of incidence. Ideal vertical separation of the measurement points was determined using a Monte Carlo simulation of the light distribution inside the cavity, providing positions of 3.9 mm above and below the center of the beam axis [88]. Horizontally, the measurement points were chosen to be 150 mm apart to provide the maximum lever arm possible without seeing scattered light from the seams on the flat mirror. Additionally, two more diodes were placed directly on the beam axis with only 90 mm of separation to monitor the fluence in the middle of the distribution. Since laser power stability was a non-issue in 2013, the obtained diode readout was monitored on an oscilloscope and correlated with direct laser power measurements on an approximately two-hour basis.

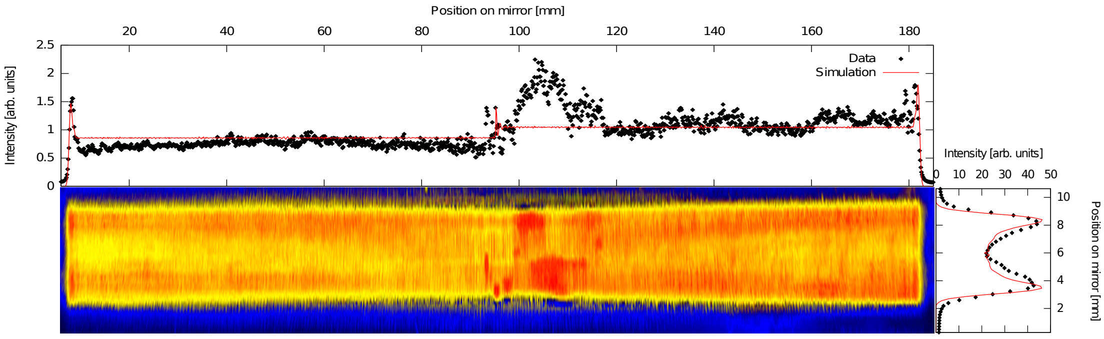

Figure 3.15: Intra cavity fluence distribution. Horizontal and vertical light distribution inside the multi-pass cavity with ideal alignment [13]. The horizontal profile shows two maxima near the edges of the illuminated volume. Near the entrance in the middle of the volume, the first reflections of the laser are still resolved leading to higher intensities.

In the end of 2013, significant damage on the edges of the in-coupling hole of the multi-pass cavity was observed. This lead to concerns about the actual stability of the beam propagation. Since the laser system is run in pulsed operation, it is only possible for the pointing stabilization system to regulate a chain of succeeding pulses. Singular stray pulses were created when the laser fired after long down times between muon triggers. These pulses can not be singled out using only the stabilization system. To get rid of this limitation, movable slit-irises (width $D = 2\,\mathrm{mm}$) were mounted directly in front of the in-coupling mirror of the target cavity, and outside the vacuum tank (see in Fig. 3.8). This geometry made it impossible for the laser to touch the edges of the injection hole without being blocked by one of the irises first.

While implementing this effort, more laser detectors were placed inside the gas target. The first one was another position sensitive quadrant photo diode behind the in-coupling mirror (see Fig. 3.12) that facilitated the in-coupling procedure into the target cavity. Another highly sensitive PIN-photodiode was installed to measure the overall transmission of the laser light through the irises.

Additional photo diodes inside the laser system provided readout values for each of the different stages of the system: disk oscillator, disk amplifier, second harmonic generation and pulsed Ti:Sa laser output. These signals were fed into different analog digital converter (ADC) channels and directly recorded in the data acquisition system. Two independent signals of the intra cavity monitoring system were additionally recorded as waveform traces to allow offline studies of the cavity lifetime.

Chapter 4

Data Acquisition and Analysis

In order to produce a laser resonance and to condense the terabytes of data that were written during the measurement periods, a lot of effort has been put in the conception of a data acquisition system (DAQ) and the analysis software. These efforts also include a number of different cuts to reduce background contributions, in order to achieve the best signal to noise ratio possible. Of special interest is a newly implemented cut that uses intrinsic physical features of the used x-ray detectors (APDs) we found to provide a clear differentiation between particle signals (published in [79]). Using this cut, the main background source for the laser resonance measurement, high energy muon decay electrons, can be discarded with high fidelity. This improvement was needed, since x-ray conversion efficiency is lower for the observed 8 keV µHe x-rays than for the previously studied 2 keV photons in the muonic hydrogen case.

4.1 Event Generation and Muon Trigger

The recording of an event takes place after the arrival of a muon in the gas target. This is signaled by a coincidental click in both muon detectors (S1 and $S2_{\text{up}}/S2_{\text{down}}$, see Chap. 3), starting a so-called **event**. Electrons from slow muons that are able to stop in the gas target create low amplitude signals below ∼100 mV in the readout photo multipliers of the detectors S1 and S2. Possible fake signals stemming from neutrons and charged particles that manage to pass the MEC show significantly higher amplitudes and can be discarded by voltage thresholds. The time of flight of usable keV muons is around ∼140 ns between both stacks. Therefore, a good muon entry signal is given by a click in the S1 detector and either one of the S2 detectors, with a the mentioned time difference. This signal coincidence creates a common timing signal for the event if the computer and readout electronics are ready (**T1**). When the laser system is also available, the command to Q-switch the disk laser (see Chap. 3) is given by the fire laser signal (**FL**).

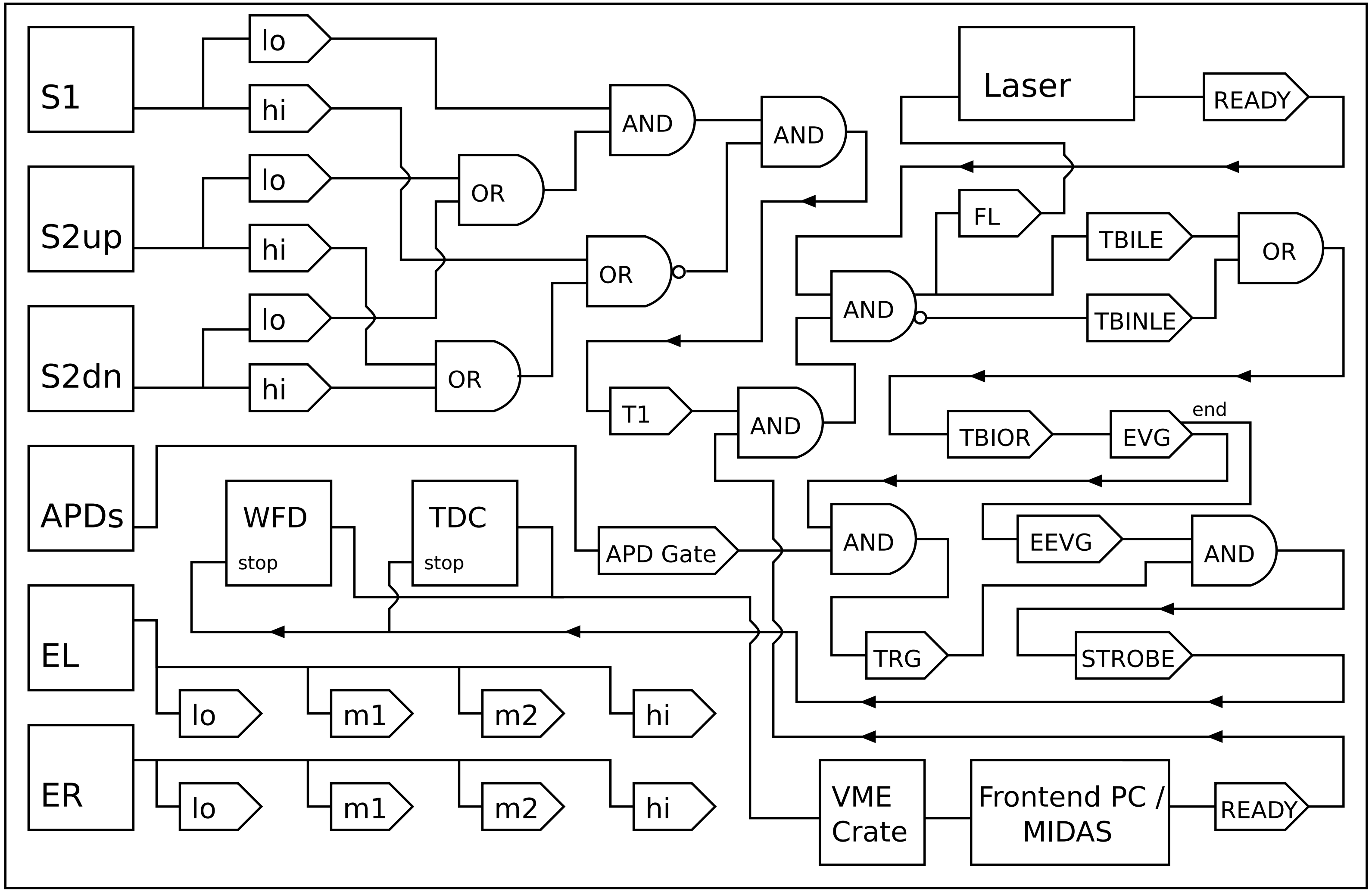
S1
S2up
S2dn
APDs
EL
ER
lo
hi
AND
OR
Laser
READY
FL
TBILE
TBINLE
T1
TBIOR
EVG
end
WFD
stop
TDC
stop
APD Gate
EEVG
TRG
STROBE
m1
m2
VME Crate
Frontend PC / MIDAS

Figure 4.1: Data acquisition system. Simplified scheme of the used DAQ setup in the µHe-Lamb shift experiment. All detector timings are read out using CAEN V767 time- to-digital converters. The APD waveforms are stored using CAEN V1720 waveform digitizers. Signal abbreviations are the following: T1: muon entry time / EVG: event gate / FL: fire laser / TRG: APD trigger / EEVG: end of event gate / TBILE: laser event / TBINLE: non laser event / STROBE: DAQ readout trigger

To reduce the amount of data to be recorded, detector signals are only read out when an APD hit was registered within a 15 µs time window after the muon entry. This time period, in addition with a 5 µs head start before the **T1** signal, makes up the so-called event gate (**EVG**). A crossing of the APD signal threshold of ∼100 mV (varying between the different APDs) during the **EVG** creates the **STROBE** signal after the end of the event gate (**EVG**), leading to a readout of the TDC modules as well as the respective WFD channels with the APD signals. By only recording in this time period around the muon entry, the data volume can be reduced drastically compared to continuous readout. When the APD signal threshold is not crossed during the **EVG**, the ADC modules are reset. For a good **event**, all gate and detector timings are stored in different TDC channels, while the traces from the x-ray detectors are stored in separate WFD channels. A sketch of the electronics used in the DAQ system is given in Fig. 4.1.

To process and store the recorded detector clicks, the DAQ system uses MIDAS [89], software developed by PSI and TRIUMF for high statistics particle physics experiments. Using this framework, recording, storing and processing of data was separated onto multiple computers. I wrote a new analysis software based on CERN ROOT [90] that processes the recorded data and apply the cuts needed to extract a resonance.

4.2 Background Reduction and Cuts

During the 2013 and 2014 measurement campaigns APD signals were recorded with a rate of roughly 2×10^5 events per hour. In contrast, the expected rate of successful $2S - 2P$ laser excitations in both muonic helium isotopes is only on the order of 10 events per hour [2]. This means that a background reduction of at least 10^4 is required to see indications of the driven transition signal in a reasonable amount of time.

APD signal analysis: The first step in this process is the analysis of the recorded APD waveform traces. To extract energy and timing information of the x-ray and electron signals, a software routine performs a fit of the recorded trace with previously prepared standard responses for each APD. The used procedure is further explained in App. A.

X-ray identification: To improve the signal to noise ratio of detected x-rays, they have to be separated from the contribution of muon decay electrons. All signals that show a timing coincidence (δt ∼20 ns) between the measured APD timing and one of the additional electron plastic scintillators (see Chap. 3) are flagged as electrons and removed from the x-ray spectrum. The same happens for all signals with energies >10 keV, since the relevant x-ray energy for the spectroscopy measurement stems from

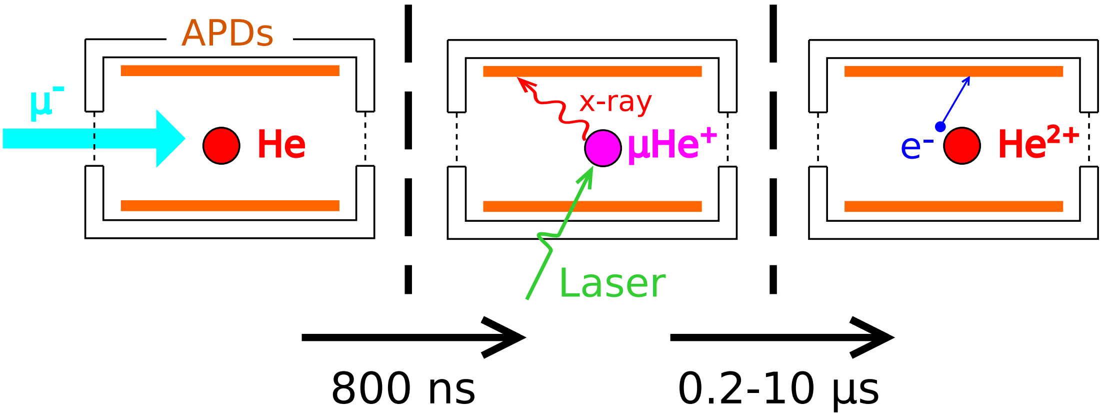

Figure 4.2: Principle of the delayed electron cut. An ideal event in the experiment consists out of the following processes: A muon enters the low pressure gas target, stops, and forms a muonic helium ion. Then, after a time delay of roughly 800 ns, the laser pulse arrives in the target, excites the Lamb shift transition and the escaping $\mathbf{K}_\alpha$ photon is detected in coincidence with the laser. After a 2.2 µs, the bound muon decays under the emission of an MeV electron. The detection of this electron 0.2-10 µs later serves as validation mechanism for the muonic x-ray.

the µHe $\mathbf{K}_\alpha$ photons at 8.2 keV and larger signals are caused by electrons with very high probability.

It was found that the employed APD trace fitting routine can also be directly used to provide a high fidelity separation between recorded x-ray and electron signals, by using the shape of the recorded pulse. This feature is also further discussed in App. A.

Delayed electron cut: As mentioned, the main source of background for the resonance measurement stems from muon decay electrons that are hard to differentiate from real x-ray signals. The fact that only one electron is created in the muon decay however can be used to differentiate the real x-ray signals from the background. If a recorded APD hit is followed by another signal from the muon decay electron in a delayed time window, the first signal is verified as x-ray. Since the muon lifetime is 2.2 µs on average [71] the software looks for electron signals up to 10 μs after first signals in order to provide verification. Fig. 4.2 visualizes the principle of the delayed electron cut. The class of signals surviving this cut is called **x-ray + del-e** and trades off roughly 40% x-ray statistics for a significantly better signal to noise ratio.

Second muon cut: Another background contribution is caused by so-called second muons. These second muons enter the gas target after an event gate has already been opened, form muonic ions, and undergo the atomic cascade creating prompt x-rays.

Due to their statistical distribution, the emission of secondary $\mathbf{K}_\alpha$ x-rays shows up as a flat contribution in time. By correlating all eligible delayed $\mathbf{K}_\alpha$ photons with signals from the muon entry detector S1, about 80% of the second muon background can be discarded. This is done by requiring that there was no hit in the S1 detector in a suitable time window together with the detected x-ray.

Energy cut: After discarding most electron signals and signals from secondary muons, an optimized energy cut on the $\mathbf{K}_\alpha$ peak in the energy spectrum removes all x-ray contributions that are not of interest for the experiment. An example for these would be the µHe $\mathbf{L}_\alpha$ x-rays at 1.5 keV that are emitted during the atomic cascade.

LTW cut: The final step to prepare the resonance is to normalize the remaining signals in the laser time window (LTW, ∼1 µs after muon entry) with the number of prompt **x-ray + del-e** $\mathbf{K}_\alpha$ events (directly after muonic atom formation) recorded for the same laser frequency. It is very important to use the same cuts on the prompt and delayed events to accurately cancel out differences in acquired statistics for different laser frequencies. During the measurement periods, the timing for the LTW cut was obtained by observing low energy signals in the APDs, created by stray photons coming from the multi-pass cavity that show the same timing as the fluorescence x-rays. In the offline analysis, the LTW-cut was directly optimized with regard to the observed laser induced $2S-2P$ events. Fig. 4.3 summarizes the effect of all used cuts, while the details and parameters are given in App. B.

4.3 Line Shape Model and Fitting of the Resonance Signal

The basis for the resonance fit are binned x-ray time spectra in which all events of different measurement runs for the same laser frequency are summed. When the previously discussed cuts are applied on this spectrum, the events are divided in Laser-On and Laser-Off data points, according to whether the laser was ready and firing during the recording of the event, or not. While Laser-On data contains the actual information for the resonance determination, Laser-Off data serves as means to determine the background level of the measurements with higher precision. The ratio between Laser-On and Laser-Off data was approximately 4:1 for both measurement campaigns.

Since the absolute number of $\mathbf{K}_\alpha$ x-rays in the LTW is used for the fit, variations in statistics for the different data points have to be accounted for. These deviations are created by varying measurement run lengths and differences in accelerator performance during the data taking. Additionally, changes in laser pulse energy between data points have to be considered as well. Both of this is done by the line shape model (LSM) that

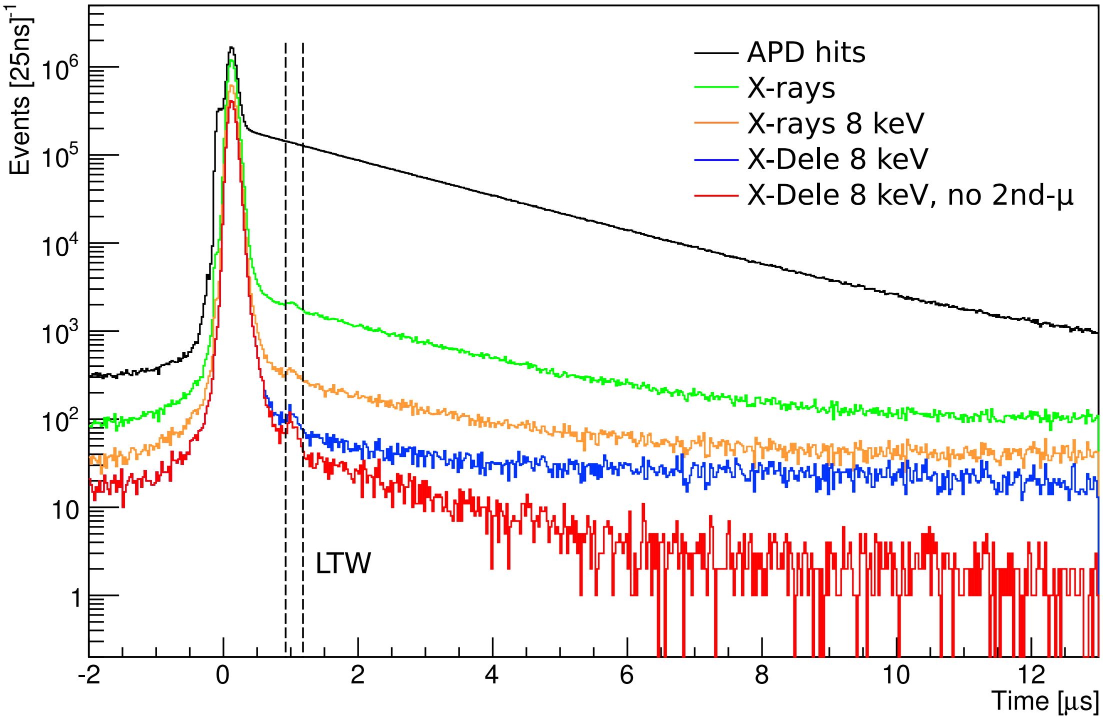

Figure 4.3: Efficiencies of the used cuts. A corresponding plot for the 2009 muonic hydrogen analysis can be found in [31]. Due to improved noise hunting efforts, the flat background contribution to the raw APD signals is significantly reduced in the muonic helium dataset. With the new trace fitting routine described in App. A, the x-ray cut has an increased efficiency that was previously partly covered by the delayed electron cut. The second muon cut has lower efficiency due to unwanted laser signals that prevented the use of the S2 photo multipliers for the cut. The resonance from the laser measurements is visible in the LTW around 1 µs.

scales the Lorentzian line profile with the acquired statistics per frequency and the average laser energy of the contributing measurement runs.

A simultaneous binned log-likelihood fit of both the laser-On and laser-Off data is performed using the MINUIT parameter minimization package implemented in CERN ROOT. The used fit function based on a Lorentzian is given by:

$$N_{prompt}(\nu) \cdot \left(\frac{P_{las}(\nu)}{\langle P_{las} \rangle} \cdot \frac{\mathbf{AMP} \cdot (\mathbf{FWHM}/2)^2}{(\nu - \mathbf{CNTR})^2 + (\mathbf{FWHM}/2)^2} + \mathbf{BGR} \right). \tag{4.1}$$

The four free fit parameters (**AMP** = Signal amplitude; **BGR** = Background level; **CNTR** = Center frequency; **FWHM** = Resonance width) are appropriately scaled to avoid problems caused by insufficient machine precision in the minimization process.

The Lorentzian resonance amplitude of the fit is scaled with the fraction of measured laser pulse energy per frequency to the global average pulse energy $(P_{las}(\nu)/\langle P_{las}\rangle)$. Since the experiment operates only at one third of both transitions saturation fluence power broadening is not considered. The added flat background parameter accounts for a constant fraction of fake signals registered in the x-ray detectors due to muon decay electrons.

The total fit function is scaled with the number of recorded prompt $\mathbf{K}_\alpha$ x-rays per frequency to accurately describe the data. All Laser-off data points are summed and treated as additional point on the background far off-resonance. The fitting results for both the $2S_{1/2} - 2P_{3/2}$ and $2S_{1/2} - 2P_{1/2}$ transition are given in Chap. 6.

Systematic studies of various input datasets for both resonances are given in App. E. The fit results were found to be very stable under variation of multiple different parameters of the analysis.

Chapter 5

Systematics

In order to verify the extracted rms charge radius obtained from the measured resonances (see Chap. 6) thorough systematic studies have to be performed. Due to the high enhancement of the finite size effect within the Lamb shift in muonic ions, only relatively low spectroscopic accuracies are needed to get relevant information on the charge radius of the measured nucleus. This, together with the large linewidth of the measured transitions (320 GHz) leads to the fact that many effects that have to be considered in electronic atom and ion spectroscopy can safely be neglected due to their diminishing size in comparison to the obtainable statistical accuracy. This chapter provides upper limits for possible systematic effects, together with a discussion of the uncertainty that is given by laser calibration.

5.1 Resonance Linewidth

The size of both the $2S_{1/2}-2P_{3/2}$ and $2S_{1/2}-2P_{1/2}$ transitions is given by their natural width. It is dominated by the lifetime of the decaying $2P$ state that can be calculated using Fermi's Golden Rule in first order perturbation theory. The corresponding decay rate is $W_{\mathrm{fi}} \approx 2.02 \cdot 10^{12} s^{-1}$, with a lifetime of the $2P$ state that is $\tau_{2P} \cong 0.50$ ps. This leads to an effective natural linewidth of [91, 92]:

$$\Gamma(2P-1S) \approx \frac{1}{2\pi\tau_{2P}} \approx 318\,\mathrm{GHz}. \tag{5.1}$$

For a combination of natural linewidth and additional Gaussian broadening effects usually a Voigt profile (convolution of Lorentzian & Gaussian) is used for data fitting. The fit employed to obtain the results presented in Chap. 6 however uses only a simple Lorentzian line profile. This is valid since the biggest additional broadening effect is given by the laser bandwidth of 840 MHz (400 times smaller than the natural linewidth) as will be shown in this chapter.

5.2 Physical Systematic Effects

Even though the frequency uncertainty of the measured resonances is only influenced by the statistical uncertainty and bandwidth of the spectroscopy laser (see Sec. 5.4) other physical effects caused by the experimental environment have to be studied in order to verify their contribution.

5.2.1 Zeeman Effect

As already mentioned in Chap. 3, the entire spectroscopy takes place in a 5 T magnetic field along the direction of the muon beam axis. This high field environment can exert shifts on the measured energy levels that are studied here. The level structure of normal atoms in this field would be significantly altered due to the breakdown of the spin and angular momentum coupling. In muonic atoms this is not the case however, since the potential created by the external magnetic field is still small in comparison to the one created by the enhanced fine structure coupling. The shift of different energy levels by the anomalous Zeeman effect can be written (in first order) as [82]:

$$\Delta E = g_{J/F} \cdot m_{J/F} \cdot \left(\frac{e\hbar B}{2m_\mu} \right). \tag{5.2}$$

Here B is the surrounding magnetic field, $m_{J/F}$ is the alignment of the total angular momentum, and $g_{J/F}$ are the Landé g-factors in fine- and hyperfine structure basis, respectively [93]:

$$g_J = g_L \frac{J(J+1) - S(S+1) + L(L+1)}{2J(J+1)} + g_S \frac{J(J+1) + S(S+1) - L(L+1)}{2J(J+1)} \tag{5.3}$$

$$g_F = g_J \frac{F(F+1) - I(I+1) + J(J+1)}{2F(F+1)} + g_I \frac{\mu^{3He}}{\mu^{\mu}} \frac{F(F+1) + I(I+1) - J(J+1)}{2F(F+1)}, \tag{5.4}$$

Here μ^{3He} and μ^{μ} are the magnetic moments of the helion and muon, and the indices S and I are the electron- and nuclear spin. The used atomic Landé factors are $g_S = 2.002$, $g_L^{4He} = 0.97$, $g_L^{3He} = 0.96$ $g_I^{3He} = 4.26$, and the magnetic moment ratio in $\mu^3\mathrm{He}^+$ is $\mu^{3He}/\mu^{\mu} = 0.24$. The resulting shifts together with the values for the total angular momenta $m_{J/F}$ are given in Tab. 5.1. 90% π-polarization can be assumed to be realistically achieved in the experiment, therefore the effect on the measured transitions is drastically smaller than the upper limits given in Tab. 5.1. Additionally, since all initial $m_{J/F}$ sub-states are equally populated in the $2S$ state with positive and negative sign, some canceling occurs between the different Zeeman sub-levels. Line broadening due to the shifts of individual $m_{J/F}$ sub-levels is still present, but negligible compared to the experimental accuracy.

$\mu^4\mathrm{He}^+$	g_J		m_J	$\lVert\Delta\nu\rVert$[MHz]	Transition	$\lVert\Delta\nu(\pi)\rVert$[MHz]	$\lVert\Delta\nu(\sigma)\rVert$[MHz]
$2S_{1/2}$	2.00		1/2	338	$2S_{1/2} \rightarrow 2P_{3/2}$	116	560
$2P_{3/2}$	1.31		1/2	222	$2S_{1/2} \rightarrow 2P_{1/2}$	231	445
$2P_{3/2}$	1.31		(3/2)	(444)			
$2P_{1/2}$	0.63		1/2	107			
$\mu^3\mathrm{He}^+$	g_J	g_F	m_F	$\lVert\Delta\nu\rVert$[MHz]	Transition	$\lVert\Delta\nu(\pi)\rVert$[MHz]	$\lVert\Delta\nu(\sigma)\rVert$[MHz]
$2S^{F=0}_{1/2}$	2.00		0	0	$2S^{F=1}_{1/2} \rightarrow 2P^{F=2}_{3/2}$	95	511
$2S^{F=1}_{1/2}$	2.00	1.51	1	511	$2S^{F=0}_{1/2} \rightarrow 2P^{F=1}_{3/2}$	0	466
$2P^{F=2}_{3/2}$	1.31	1.23	1	416	$2S^{F=1}_{1/2} \rightarrow 2P^{F=1}_{1/2}$	237	511
$2P^{F=2}_{3/2}$	1.31	1.23	(2)	(832)			
$2P^{F=1}_{3/2}$	1.31	1.38	0	0			
$2P^{F=1}_{3/2}$	1.31	1.38	(1)	(466)			
$2P^{F=1}_{1/2}$	0.61	0.81	1	274			

Table 5.1: Zeeman shift in muonic helium. Absolute shifts of the measured transitions and corresponding initial and final levels in the $\mu^4\mathrm{He}^+$ and $\mu^3\mathrm{He}^+$ ions for a magnetic field strength of 5 T. Upper limits $\lVert\Delta\nu\rVert$ for possible shifts are given for each transition, both for the π and σ polarization state. Since all $m_{J/F}$ are equally populated in the initial state, possible systematic Zeeman shifts are canceled in the measured transitions, contributing only to line broadening.

5.2.2 Doppler Shift and Broadening

All measured muonic helium resonances are one-photon transitions, therefore the first order effect of ion velocity on the measured frequency has to be considered. If the observed particles move along the laser propagation axis, the relativistic effect that describes the measured frequency ν_{meas} for a velocity class of particles in comparison to the actual frequency of the transition ν_{act} is given by the first order Doppler shift:

$$\frac{\nu_{\mathrm{meas}}}{\nu_{\mathrm{act}}} = 1 \pm \frac{v}{c}, \tag{5.5}$$

Even though incoming muons enter the gas target with kinetic energies of roughly a few keV, they lose most in inelastic collisions with surrounding helium atoms before the muonic atom formation. The kinetic energy of the bound muonic atom directly after the formation process is lower than a few eV [69] (see Sec. 3.1). Elastic collision cross sections with the remaining $\mu\mathrm{He}^+$-ions are greatly enhanced compared to the neutral muonic hydrogen [94, 95]. Since the laser pulse arrives in the target roughly 1 µs after muonic ion formation, the $\mu^4\mathrm{He}^+$ and $\mu^3\mathrm{He}^+$ systems are thermalized with the surrounding gas. During the measurement, the target is temperature stabilized to 20° C (293 K) and therefore spectroscopy ions can be assumed to have the same temperature. The mean velocity of thermalized helium ensemble is given by:

$$v_{\mathrm{mean}} = \sqrt{3\frac{k_{\mathrm{B}}T}{m}} \approx 1100\,\mathrm{m/s}, \tag{5.6}$$

Here k_B is the Boltzman's constant, T is the temperature in Kelvin and m is the mass of the µHe$^+$-ion. Since muonic ion movement is isotropic after thermalization, the Doppler effect does not contribute to a systematic shift but only to a broadening (FWHM) that can be calculated as [96]:

$$\frac{\delta\nu}{\nu} = \frac{2}{c}\sqrt{\frac{2k_\mathrm{B}T\ln 2}{m}} = 6\cdot 10^{-6}. \tag{5.7}$$

For the measured $2S_{1/2} - 2P_{3/2}$ transition, this results in an additional broadening of 2.3 GHz. This is well below the line width accuracies of the measured transitions.

As mentioned, systematic shifts of the line position due to the Doppler effect can be excluded since the muonic ions are thermalized inside the target. In order to get a non vanishing Doppler shift a correlation between the incoming muon beam and the spectroscopy ions would be needed. If the maximal remaining muon energy after initial capture would be inelastically transferred to the created muonic helium ion (25 eV, ≈ 25000 m/s), the measurable Doppler shift would be 80 ppm assuming complete collinearity with the laser. Even though not possible in the experiment, such effects would be drastically reduced by our laser geometry. The laser beam inside the multi-pass cavity illuminates the spectroscopy ions under a quasi perpendicular angle (injection angle $\phi \leq 40$ mrad) leaving only a small fraction of the input laser intensity parallel to the muon beam axis. Additionally, the propagation direction along the muon beam axis is reversed after roughly 100 reflections, leading to only 25 % laser energy asymmetry parallel to the muon beam when a reflectivity of $R = 99.9\%$ for the mirrors is assumed [31]. This reduces the mentioned shift by at least a factor of 10^3, rendering Doppler shifts irrelevant even if a correlation between muon and µHe$^+$ momentum existed.

5.2.3 DC Stark Shift

Within the setup, the measured ions are not experiencing any significant electric fields from the experimental apparatus due to the target being on ground potential. Nevertheless, their movement inside the mentioned 5T magnetic field can lead to an experience of an electrical potential due to Lorentz transformation effects. The electric field seen by ions moving perpendicular to the magnetic field direction can be calculated by (in natural units) [31]:

$$\mathrm{E}_\mathrm{ind} = \frac{\beta B_\perp}{\sqrt{1-\beta^2}}, \tag{5.8}$$

with $\beta = v/c$. Using the already mentioned thermalized temperature of 293 K and the corresponding average velocity of $v_\mathrm{avg} = 1100\,\mathrm{m/s}$ this leads to $\mathrm{E}_\mathrm{ind} \approx 0.5 \times 10^4\,\mathrm{V/m}$

in the surrounding 5 T magnetic field. Since the Lamb shift in muonic helium is even larger than in muonic hydrogen one can follow the calculation of the DC Stark effect from [31], without violating any assumptions:

$$\Delta E_{\mathrm{DC}} \approx \frac{2|H_{SP}|^2}{(E_P - E_S)_{^4\mu\mathrm{He}}} = 5.3 \cdot 10^{-18}\,\mathrm{eV}. \tag{5.9}$$

The induced energy shift between the $2S$ and $2P$ state is $(E_P - E_S)_{^4\mu\mathrm{He}} = 1.52$ eV for the DC-perturbation of the induced electric field $H_{SP} = 3\,e\,a_\mu|\mathrm{E}_{ind}| = 2.0 \times 10^{-9}\,\mathrm{eV}$ ($a_\mu = 132\,\mathrm{fm}$ is the Bohr radius of the $\mu^4\mathrm{He}^+$ system). Resulting values of the DC Stark shift are below the Hz-range for muonic helium and therefore negligible.

5.2.4 AC Stark Shift

Energy levels of atoms present in an oscillatory electric field are shifted due to the AC Stark effect (also called light shift). The effect is best described in quantum mechanics within a dressed state framework and can be investigated by solving the time dependent Schrödinger equation using the rotating wave approximation. For a two level system with infinite state lifetime and an influencing monochromatic laser field, the shifts of the ground- and excited state are given by:

$$\Delta E_{g,e} = \frac{\hbar}{2}(-\delta \pm \Omega'), \tag{5.10}$$

where δ is the frequency detuning of the laser with respect to the resonant transition and $\Omega' = \sqrt{\Omega^2 + \delta^2}$ is the generalized Rabi frequency. Ω is the unmodified Rabi frequency that depends on the strength of the surrounding electric field created by the laser:

$$\Omega = \frac{-e|\mathrm{E}|}{\hbar} \langle e|\hat{r}|g\rangle \,, \tag{5.11}$$

with $e\hat{r}$ as the dipole operator and $\langle e|\hat{r}|g\rangle = \sqrt{6a_\mu^2}$ as the transition matrix element between the ground- and excited state [2]. Using the pulse duration of 50 ns and the saturation fluence of the $2S_{1/2} - 2P_{3/2}$ transition ($1.1\,\mathrm{J/cm^2}$) as upper limit, one can calculate the electric field seen by the muonic ions: $|\mathrm{E}| = 2.5 \times 10^6\,\mathrm{V/m}$. This leads to a Rabi frequency of $\Omega = 2.0 \times 10^8\,s^{-1}$.

The shift in absolute transition energy is given by the summed shifts of the ground and excited level: $\Delta E_{tot} = \hbar\,\Omega'$. In the limit of small and large detunings this simplifies to, respectively:

$$\Delta E_{|\delta|\ll\Omega} = \mathrm{sgn}(\delta)\,\hbar\Omega \quad \text{and} \quad \Delta E_{|\delta|\gg\Omega} = \frac{\hbar\Omega^2}{2\delta}. \tag{5.12}$$

The maximum possible frequency shift for the transitions is given in the low-δ limit. For real detunings in the measurement ($\delta \approx \Gamma/2 = 160\,\mathrm{GHz}$) the shift is small:

$$\Delta\nu_{|\delta|\gg\Omega} = \frac{\Omega^2}{4\pi\delta} = 20\,\mathrm{kHz}. \tag{5.13}$$

Since the transition energy shift depends on the sign of the laser detuning as can be seen in Eq. 5.12, the AC Stark shift only leads to a broadening in one-photon transitions. The calculated broadening is not resolvable in the experiment and is therefore neglected.

Solutions of the two level system with an infinite lifetime can only be regarded as an approximation, since the $2P$ state is short lived. The influence of the short $2P$-state lifetime was already investigated for muonic hydrogen that shares very similar properties to the muonic helium ion. It was found in [31] that the ps lifetime of the excited state leads to a dampening of the Rabi-oscillations between the $2S$ and $2P$ state. This causes the absolute AC Stark shift for the muonic bound system to vanish. Non-resonant coupling to the other respective $2P$-state can be ignored for both the $2S_{1/2} - 2P_{3/2}$ and $2S_{1/2} - 2P_{1/2}$ transitions since they are far enough separated (~ 100 line widths).

5.2.5 Pressure Shift and Broadening

The influence of collisional effects on the measured µHe transitions has been studied in [97]. Due to the finite gas pressure of a few hPa in the experiment, the observed µHe$^+$-ions interact with the surrounding helium atoms. The interruption of the excitation process from the $2S$ state by collisions leads to a shift in the resonance position as well as to an additional broadening of the line profile. For µ^{3}He$^+$ and µ^{4}He$^+$ these effects were calculated at a gas pressure of 100 hPa using a fully quantum-mechanical close-coupling approach [97]. These calculations serve as upper limit for the significantly lower gas pressure in the experiment.

Fig. 5.1 shows the temperature dependence of both the calculated resonance shift, and the line broadening for the measured µ^{4}He$^+$ resonances. The pressure shifts of the $2S_{1/2} - 2P_{3/2}$ and $2S_{1/2} - 2P_{1/2}$ transitions were calculated to be 35 MHz and 33 MHz respectively for a gas pressure of 100 hPa [97]. Conservatively, effects in our experiment can therefore be estimated to be 1 MHz. The induced broadening of ≈3 MHz is negligible for the resonance determination.

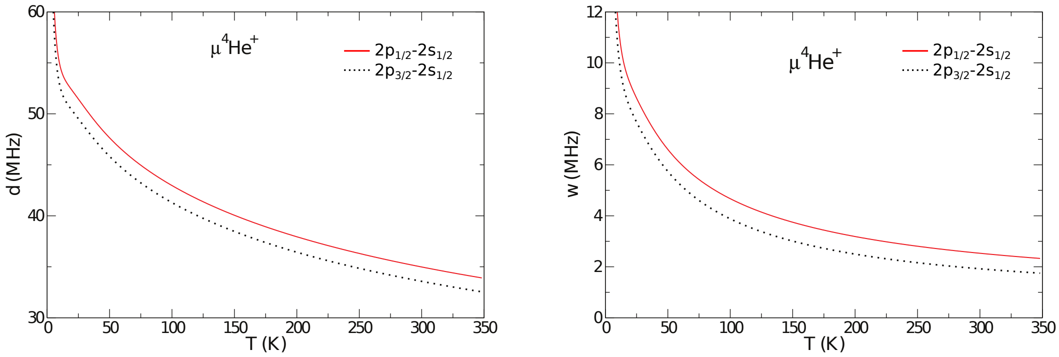

Figure 5.1: μ^4He$^+$ pressure shift and broadening. Left: Pressure shift (d) of both $2S-2P$ transitions plotted versus temperature (T) for a gas pressure of 100 hPa [97]. Right: Pressure broadening (w) versus temperature (T) for the same transitions with the same ambient pressure [97].

5.3 Laser Parameters

The only relevant systematic contributions to the experimental extraction of the different Lamb shift transitions stems from uncertainties in frequency determination of the pulsed spectroscopy laser. Additional effects from the extended bandwidth of the laser, as well as the frequency offset (chirp) between the CW and pulsed laser have also been studied.

The bandwidth of the pulsed Ti:Sa laser system was evaluated at multiple pulse energies by comparing the width of the laser frequency spectrum to the free spectral range ν_{fsr} of the stabilized Fabry-Pérot cavity. It was found that the bandwidth does not correlate with the observed pulse energy and the average value was measured to be:

$$\Delta\nu_{(\mathrm{FWHM})} = 840 \pm 100\,\mathrm{MHz}. \tag{5.14}$$

5.3.1 Laser Chirp

The pulsed spectroscopy laser is only indirectly stabilized by seeding with an actively stabilized, highly accurate CW laser and locking its cavity to a matching transmission fringe. By this, the center frequency of the pulsed oscillator is determined by the frequency of the already circulating photons from the CW light (in a dispersion free environment). In reality however, the laser medium, the mirrors and the air which surrounds the oscillator components create dispersion, leading to a dependence of the laser frequency on the intra-pulse timing. This chirp is created by a change in propagation velocity for different components in the pulse frequency spectrum, leading to an observable mean frequency shift. This shift, as well as additional broadening of the

Rep. rate[Hz]	Mean frequency[THz]	Fluctuation [MHz]	Frequency shift[MHz]
CW	369.402374		
10	369.402317	±19	-57
100	369.402313	±24	-61
300	369.402312	±16	-62

Table 5.2: Pulsed Ti:Sa laser pulse chirp. Measurement of the output frequency of the pulsed Ti:Sa oscillator with respect to the frequency CW operated seed laser for different repetition rates. Effects of the measured laser chirp are small compared to the accuracies of the Lamb shift determinations.

introduced laser chirp has been studied since the laser frequency is not monitored on an event-to-event basis.

For a frequency close to the first $\mu^4\mathrm{He}^+$ transition ($2S_{1/2} - 2P_{3/2}$), the output of the pulsed laser and its seed were compared using a commercial wavemeter (Finesse WS-7) while the seed laser was actively stabilized to the reference Fabry-Pérot cavity of the experiment. Measurements were repeated for several repetition rates to account for different thermal conditions within the laser medium. Each measurement was performed over a time range of 10 minutes, recording 5×10^4 values per repetition rate for randomly selected pulses. A summary of these measurements can be seen in Tab. 5.2. It was found that the measured chirp leads to a negative frequency shift of $\Delta\nu = -60\pm25\,\mathrm{MHz}$.

Supplementary chirp measurements were performed using saturated Kr absorption spectroscopy at 811 nm for different pulse energies. This data set resulted in a chirp value of $\Delta\nu = -87 \pm 56\,\mathrm{MHz}$ that agrees with the spectrometer method although with larger uncertainty. This value is negligible in comparison to the statistical uncertainty of the measurement.

5.3.2 Laser Pulse Energy Calibration

Due to low excitation rates of the measured transitions (on the order of 10-20 events/h) laser stability and laser energy measurements in regular intervals are paramount to achieve a good accuracy of the extracted resonance frequency. A significant difference in laser power seen by the ions for different near-resonance frequencies can lead to an asymmetry in the observed signal. This effect can be corrected by a line shape model, if average power measurements are available for each data point.

As already discussed in Sec. 3.5.3, a newly developed monitoring system was installed to measure the laser fluence inside the target cavity. For the determination of the first

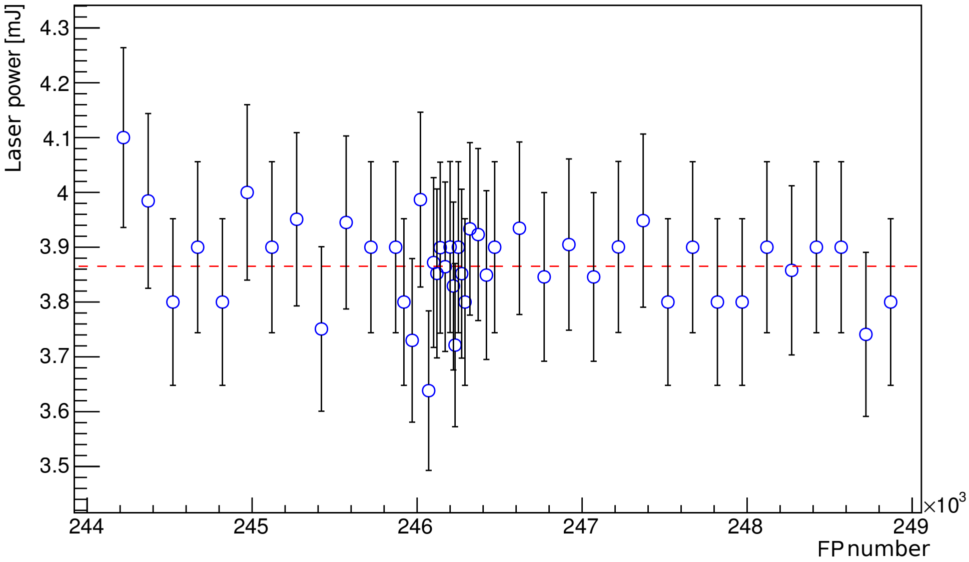

Figure 5.2: Ti:Sa pulse energy measurements. Values of the Ti:Sa output energies per Fabry-Pérot fringe in the $2S_{1/2} - 2P_{3/2}$ measurement campaign. On average, the laser system provided 4 % rms energy stability over the entire measurement campaign. The dashed red line shows the average pulse energy of 3.87 mJ. For the other transitions, one of the multi-pass cavity fluence monitoring diodes was used to provide this information

μ^4He^+ line ($2S_{1/2} - 2P_{3/2}$) this system was only used as a crosscheck for measurements of the pulsed Ti:Sa laser output. Pulse-to-pulse stability of the laser output was determined to be better 4 % rms. Pulse energy measurements with a 100 Hz trigger were undertaken on a 1-2 hour basis at each change in laser frequency. Drifts between interruption-free successive measurements were below 10%.

The average pulse energy per measured frequency fluctuated less than 15% over the entire measurement range, as can be seen in Fig. 5.2. The laser power asymmetry between both sides of the $2S_{1/2} - 2P_{3/2}$ resonance was measured to be (1.0 ± 1.2) %. This would lead to 1.5 ± 1.8 GHz shift in the determination of the resonance position when fitting a normal Lorentzian. This is however already covered by the LSM (see Sect. 4.3).

For the rest of the measured transitions in μ^4He^+ and μ^3He^+, a number of additional laser energy detectors were implemented and read out on a event-per-event basis (see Sec. 3.5.4) in contrast to the manual measurements in 2013.

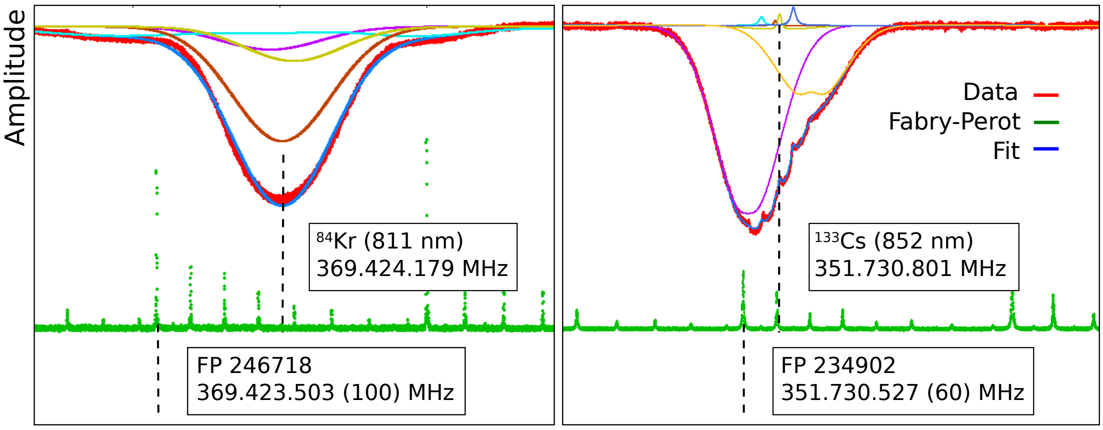

Figure 5.3: Saturated spectroscopy of Kr and Cs for calibration. Two recorded spectra of saturated absorption spectroscopy of the $5s^{J=2}_{[3/2]}$-$5p^{J=3}_{[5/2]}$ line in the different Kr isotopes (left) and the $6S_{1/2}$-$6P_{3/2}$ hyperfine transitions in ^{133}Cs (right) [98]. The biggest contribution in Kr stems from ^{84}Kr, the isotope with the highest natural abundance (orange) and was used as reference. In Cs, the $F = 3 \rightarrow F = 3$ transition was used as reference (frequency indicated by the vertical dashed line). The green spectrum shows the transmission fringes of the stabilized Fabry-Pérot cavity. The highest peaks correspond to the TEM_{00} modes.

5.3.3 Frequency Calibration

For the determination of the $2S_{1/2} - 2P_{3/2}$ transition in μ^4He^+ the measure of laser frequency was given by the fringes of an actively stabilized Fabry-Pérot cavity (FP). This provided a stable frequency reference for the CW seed laser. Calibration of the individual FP fringe positions was done using a commercial wavemeter. The wavemeter itself was calibrated using transitions measured in saturated Kr and Cs spectroscopy. The used lines are located at 810 nm and 811 nm for Kr [99, 101] and around 852 nm for Cs [100]. A fit of two used transitions together with the respective FP fringes is shown in Fig. 5.3. A quadratic fit of 60 neighboring FP fringes was done to obtain the parameterization used for the calculation of the set laser frequency:

$$\begin{aligned}
\nu_{\text{FP}}(N) &= \nu_{\text{quad}} \cdot N^2 + \nu_{\text{fsr}} \cdot N + \Delta\nu_{\text{off}} && (5.15)\\
\nu_{\text{quad}} &= -5.2594864228 \cdot 10^{-7} \quad \text{MHz} && (5.16)\\
\nu_{\text{fsr}} &= 1.4976121928 \cdot 10^{3} \quad \text{MHz} && (5.17)\\
\nu_{\text{off}} &= -3.2532092343 \cdot 10^{4} \quad \text{MHz} && (5.18)
\end{aligned}$$

The linear component ν_{fsr} corresponds to the free spectral range $L = c/2L$ of the FP between 800 nm and 820 nm, and gives the spacing of two neighboring TEM_{00} fringes. The offset and quadratic term serve as means to account for slight variations of the free spectral range due to the mirror coating. Calibration in this range was found to be

Line / Fringe (N)	meas. Freq. [MHz]	calc. Freq. [MHz]	Diff. [MHz]
^{84}Kr 5s$^{J=2}_{[3/2]}$-5p$^{J=2}_{[5/2]}$	369 813 049 [99]		
246 978	369 812 577 (100)	369 812 627	-50
^{84}Kr 5s$^{J=2}_{[3/2]}$-5p$^{J=3}_{[5/2]}$	369 424 179 [99]		
246 718	369 423 460 (100)	369 423 315	+144

Line / Fringe (N)	meas. Freq. [MHz]	calc. Freq. [MHz]	Diff. [MHz]
^{133}Cs 6S$^{F=3}_{1/2}$-6P$^{F=3,4}_{3/2}$	351 730 801 [100]		
234 902	351 730 527 (50)	351 730 801	-414
^{133}Cs 6S$^{F=4}_{1/2}$-6P$^{F=3,4}_{3/2}$	351 721 835 [100]		
234 896	351 722 351 (50)	351 723 037	+779

Table 5.3: Measured calibration lines. Top: Fabry-Pérot calibration for the $2S_{1/2}-2P_{3/2}$ transition measurement. ^{84}Kr lines served as calibration points for the frequency. The accuracy of the calibration is given by the position uncertainty of the used lines and is satisfactory around the measured resonance. Bottom: Additional calibration measurements in a lower frequency range. The free spectral range of the Fabry-Pérot is altered due to phase effects within the multilayer coating that was not optimized for this frequency range. This leads to offsets from the calibration determined at 370 THz . For this reason the Fabry-Pérot was abandoned for the frequency measurements of the remaining µ^{4}He$^+$ and µ^{3}He$^+$ transitions. These were done directly with the calibrated wavemeter.

accurate on a 100 MHz level and agreed with the previous calibration used in the 2009 muonic hydrogen measurement. As secondary reference for the $2S_{1/2}-2P_{3/2}$ transition measurement, additional out of loop wavemeter recordings were taken for each measurement point.

Table 5.3 summarizes the transitions used for calibration. As can be seen, there is a significant difference between the measured and calculated positions of the FP fringes at 852 nm (∼351 THz). This is due to degrading mirror quality in this frequency range, leading to significant phase shifts at each reflection but does not influence the calibration near the $2S_{1/2}-2P_{3/2}$ transition. For the measurement of the second µ^{4}He$^+$ transition ($2S_{1/2}-2P_{1/2}$), as well as all remaining µ^{3}He$^+$ transitions, the Ti:Sa seed laser was directly stabilized on the output of the previously calibrated commercial wavemeter with an accuracy of 60 MHz to circumvent this problem The lock on individual FP fringes was still used for rough stabilization, while the wavemeter output provided fine control for the servo loop of the CW laser.

5.4 Total Uncertainty Budget

All systematic effects on the determination of the muonic helium Lamb shift are negligible for the targeted accuracy of 50 ppm. Frequency shifts caused by the properties of the laser system are also well below the measurable limit in the frequency determination. The biggest uncertainty is created by the limited statistics available for the fit of the line position. This leads to the absolute achievable accuracy as summarized in Tab. 5.4. The systematic uncertainties of the measurements are a factor 100 smaller than the statistical limits and therefore negligible.

Effect	$2S_{1/2} - 2P_{3/2}$		$2S_{1/2} - 2P_{1/2}$	
	Shift [GHz]	Unc. [GHz]	Shift [GHz]	Unc. [GHz]
Statistics	0	16.8	0	14.0
Zeeman Shift	0	≤ 0.1	0	≤ 0.1
Doppler Shift	0	≤ 0.03	0	≤ 0.03
AC Stark Shift	0	$\leq 2 \cdot 10^{-5}$	0	$\leq 2 \cdot 10^{-5}$
DC Stark Shift	0	$\leq 1 \cdot 10^{-9}$	0	$\leq 1 \cdot 10^{-9}$
Pressure Shift	0	$\leq 1 \cdot 10^{-3}$	0	$\leq 1 \cdot 10^{-3}$
Laser Chirp	-0.06	0.03	-0.06	0.03
Laser Freq. Cal.	0	0.1	0	0.06
Laser Energy Cal.*	0	0	0	0
Total (syst.)	-0.06	0.15	-0.06	0.15

* Included in LSM.

Table 5.4: Uncertainty budget for the μ^4He$^+$ $2S_{1/2} - 2P_{3/2}$ and $2S_{1/2} - 2P_{1/2}$ lines. Values and uncertainties of the different systematic effects for the measurement of the μ^4He$^+$ Lamb shift. Uncertainties originating from the laser are still well below the statistical uncertainties of the two measured resonances. All additional broadening contributions from the experimental environment are negligible due to the width of both transitions (320 GHz).

Chapter 6

Results and Discussion

The data of both measured Lamb shift transitions in $\mu^4\mathrm{He}^+$ and the fit results of their respective energies are presented in this chapter. From the measurements it is possible to extract two independent values of the alpha particle rms charge radius by either using the $2S_{1/2} - 2P_{3/2}$ transition and subtracting the calculated fine structure, or by using the $2S_{1/2} - 2P_{1/2}$ transition directly as Lamb shift value. Alternatively, both transitions can be used to extract the fine structure of the 2P-state.

Towards the end of this chapter an overview of the measured $\mu^3\mathrm{He}^+$ transitions will be provided. These were investigated during later stages of the experiment. Since data analysis and theory in $\mu^3\mathrm{He}^+$ are still in a preliminary state, no definite results for the rms radius or the hyperfine splitting in $\mu^3\mathrm{He}^+$ are given.

6.1 The $\mu^4\mathrm{He}^+$ $2S_{1/2} - 2P_{3/2}$ Transition

Using the line shape model and fitting routine explained in Sec. 4.3, the pre-processed data for the $2S_{1/2} - 2P_{3/2}$ transition were analyzed using a binned log-likelihood fit as given in Form. 4.1. The position and width of the resonance were determined (given in units of the Fabry-Pérot free spectral range):

$$N_{\mathrm{Pos}} = 246208(11), \tag{6.1}$$

$$N_{\mathrm{FWHM}} = 229(36). \tag{6.2}$$

The recorded signal to noise ratio is 2.5 : 1, with a good $\chi^2_{\mathrm{red}} = 1.25$ ($\chi^2 = 52.7$ for 42 normalized degrees of freedom) and the overall significance of the resonance is $14.5\,\sigma$. Using the parameterization of the Fabry-Pérot fringe position determined in Sec. 5.3.2, the centroid frequency and width of the $2S_{1/2} - 2P_{3/2}$ transition are:

$$\underline{\nu_{\,2S_{1/2}-2P_{3/2}} = 368.660(17)_{\text{total}}\,\text{THz},} \tag{6.3}$$

$$\Delta\nu^{\,\text{FWHM}}_{\,2S_{1/2}-2P_{3/2}} = 340(53)_{\text{total}}\,\text{GHz}. \tag{6.4}$$

Uncertainties represent the statistical errors of the fit, since all other contributions are negligible as seen from Tab. 5.4. The measured linewidth is in very good agreement with the predicted linewidth of 318 GHz (see Sec. 5.1). The resonance position determination from the offline analysis is only $0.4\,\sigma$ smaller than the value of the online analysis during data taking. We see this as independent verification of the result.

A plot of the entire spectrum between $\nu_{\text{min}} = 365.5\,\text{THz}$ and $\nu_{\text{max}} = 373.0\,\text{THz}$ is shown in Fig. 6.1. Solid markers correspond to the Laser-on events, while the empty markers show fits of the Laser-off data. The error-bars of the Laser-On data correspond to the Gaussian error of the number of counted events. This is just for visual purposes, the fit uses the correct log-likelihood statistics. The sum of the Laser-off data is used as additional point on the background. The frequency resolved Laser-off data points in the plot are provided by a time spectrum fit of events in the LTW using an exponential background decay model in $0.9 - 8\,\mu\text{s}$ time-window after the muon entry. The points only serve as visual reference and are not part of the fit.

6.2 The µ^{4}He$^+$ $2S_{1/2} - 2P_{1/2}$ Transition

The second resonance in µ^{4}He$^+$ was analyzed identically to the first one, except for the fact that the measurement was done with the CW seed laser directly stabilized to a commercial wavemeter. Therefore the additional step of converting FP fringes back to actual frequency values is not necessary. A plot of the fitted $2S_{1/2} - 2P_{1/2}$ resonance is given in Fig. 6.2. The values extracted for the center frequency and resonance linewidth of the $2S_{1/2} - 2P_{1/2}$ transition are:

$$\underline{\nu_{\,2S_{1/2}-2P_{1/2}} = 333.352(16)_{\text{total}}\,\text{THz},} \tag{6.5}$$

$$\Delta\nu^{\,\text{FWHM}}_{\,2S_{1/2}-2P_{1/2}} = 292(54)_{\text{total}}\,\text{GHz}. \tag{6.6}$$

The signal to noise ratio of 3.2 : 1 is similar to the fit of the $2S_{1/2} - 2P_{3/2}$ transition. The factor of two smaller matrix element of the second transition was compensated by improvements to the DAQ electronics and a factor of 1.5 increase in laser power.

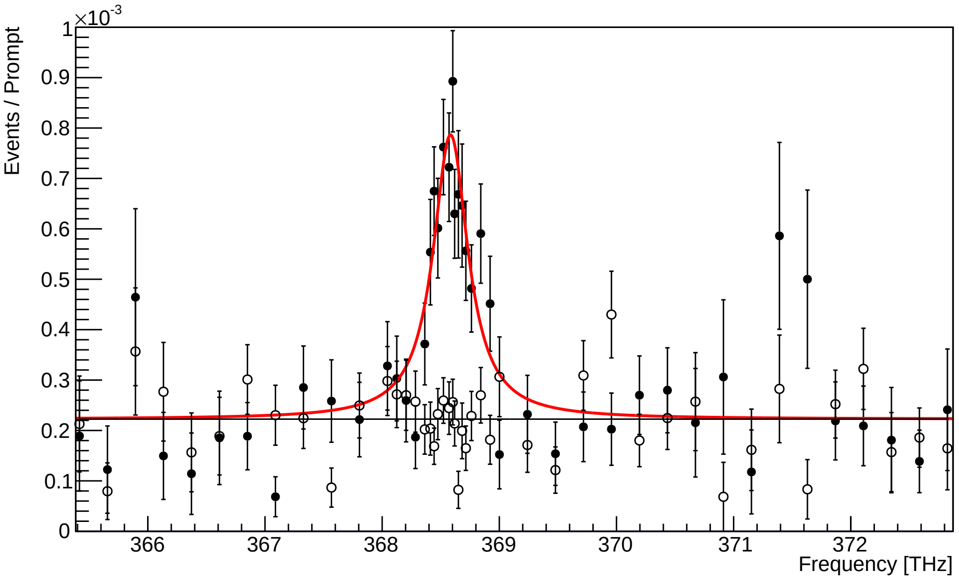

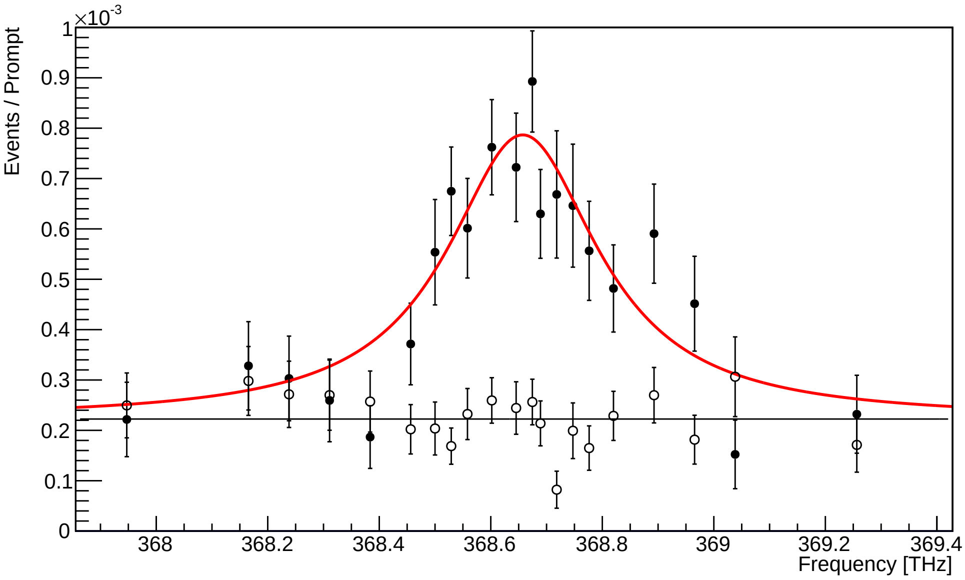

Figure 6.1: The μ^{4}He$^+$ $2S_{1/2} - 2P_{3/2}$ resonance. Fit of the experimental data used to determine the position of the $2S_{1/2} - 2P_{3/2}$ transition in μ^{4}He$^+$. Top: Entire data used in the position determination of the resonance. Bottom: Zoomed view on the relevant part of the resonance. Both data sets for Laser-on data (full circles) and Laser-off data (empty circles) are shown. Laser-off points are extracted using a fit of the time dependent x-ray background and serve only as verification for the Laser-On data.

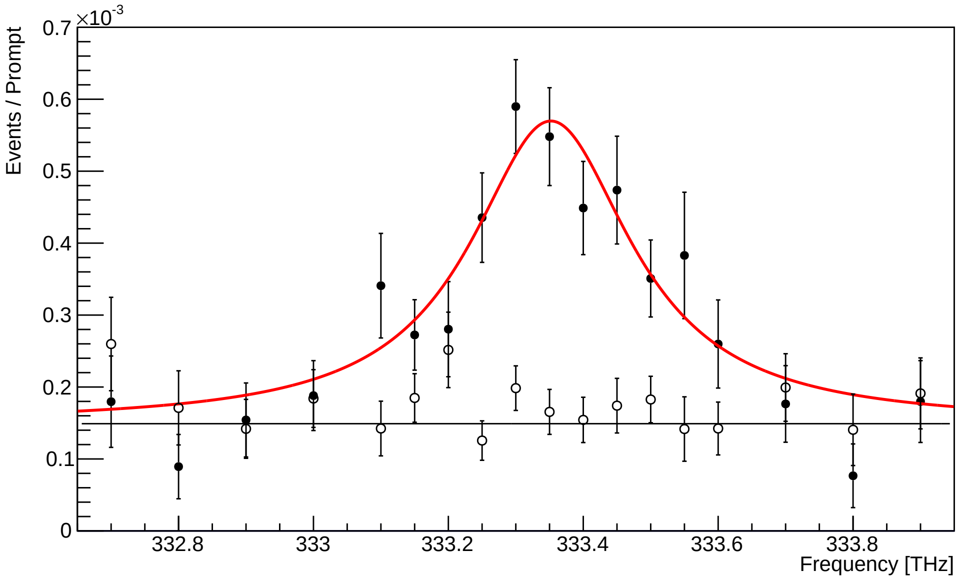

Figure 6.2: The μ^{4}He$^+$ $2S_{1/2} - 2P_{1/2}$ resonance. Fit of the experimental data used to determine the position of the $2S_{1/2} - 2P_{1/2}$ transition in μ^{4}He$^+$. Both laser-on data (full circles) and laser-off data (empty circles) are shown.

The $\chi^2_{\text{red}} = 1.07$ ($\chi^2 = 16.1$ for 15 normalized degrees of freedom) value is also very good for the low number of data points. The measured resonance linewidth is also in good agreement with the prediction.

6.3 Extracted Value of the ^{4}He Charge Radius

Using the measured transitions it is possible to extract two independent values of the Lamb Shift in μ^{4}He$^+$. The first one is obtained by using the energy difference of the $2S_{1/2} - 2P_{3/2}$ transition and subtracting the theoretical fine structure energy difference ΔE_{FS} (see Sec. 2.3). Alternatively, the measured $2S_{1/2} - 2P_{1/2}$ energy difference can be used to determine the $2S - 2P$ Lamb shift directly without involving the theoretical fine structure calculation. The Lamb shift determinations of both measurements are:

$$\Delta E_{\text{LS}}^{2S_{1/2}-2P_{3/2}} = 1378.463(70)\,\text{meV}, \tag{6.7}$$

$$\Delta E_{\text{LS}}^{2S_{1/2}-2P_{1/2}} = 1378.633(66)\,\text{meV}. \tag{6.8}$$

The two extracted values are in agreement, $1.75\,\sigma$ (combined) separated from each other. This allows averaging of the LS values using the statistics of both measurements:

$$\underline{\Delta E_{\,\mathrm{LS}} = 1378.553(48)\,\mathrm{meV}}. \tag{6.9}$$

Using the summary of Lamb shift QED contributions given in Tab. 2.1 and Tab. 2.2 the rms charge radius of the ^{4}He nucleus can be extracted:

$$r_{^4\mathrm{He}} = 1.67829(14)_{\mathrm{exp}}(52)_{\mathrm{theo}}\,\mathrm{fm}, \tag{6.10}$$

$$\underline{= 1.67829(54)_{\mathrm{total}}\,\mathrm{fm}}. \tag{6.11}$$

The experimental uncertainty is significantly smaller than the uncertainty induced by theory. This is caused by the not accurately known nuclear structure dependent polarizability term. Compared to the previous determination of the ^{4}He nuclear rms charge radius of 1.681(4) fm [67], our value is on average 0.3 % smaller but also more than seven times more accurate. This corresponds to an 0.7 σ offset to the electron scattering value, therefore being in good agreement. After further improvements of the nuclear structure theory in muonic helium, the extracted rms charge radius will be able to provide a more than factor of ten smaller uncertainty than the current electron scattering value.

6.4 The μ^4He$^+$ Fine Structure Splitting

From measurements of both the $2S_{1/2}-2P_{3/2}$ and the $2S_{1/2}-2P_{1/2}$ transition, the first experimental deduction of the $2P$ fine structure in muonic atoms can be performed. The $2P_{3/2}-2P_{1/2}$ fine structure value is given by the energy difference of both measured transitions ($\Delta E_{2S_{1/2}-2P_{3/2}} - \Delta E_{2S_{1/2}-2P_{1/2}}$):

$$\underline{\Delta E_{\mathrm{FS}}^{(\mathrm{Exp})} = 146.022(96)\,\mathrm{meV}}. \tag{6.12}$$

This can be compared to the theoretical $2P_{3/2} - 2P_{1/2}$ value that was obtained from QED calculations (summarized in Tab. 2.3):

$$\Delta E_{\mathrm{FS}}^{(\mathrm{QED})} = 146.192(13)\,\mathrm{meV}. \tag{6.13}$$

The newly provided experimental value is in agreement with theory and the small 1.75 σ offset is the same as already seen in the two independent Lamb-shift determinations.

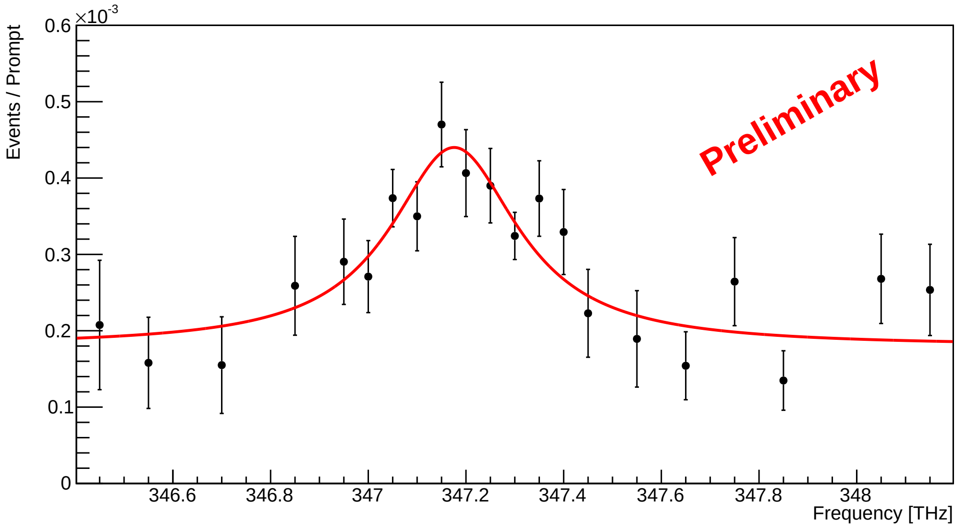

Figure 6.3: Preliminary µ^{3}He$^+$ $2S_{1/2}^{F=1} - 2P_{3/2}^{F=2}$ resonance. Plot of the first measured transition in µ^{3}He$^+$. Shown is only the laser-on data with Gaussian errors and a χ^2 fit determining the line shape and position.

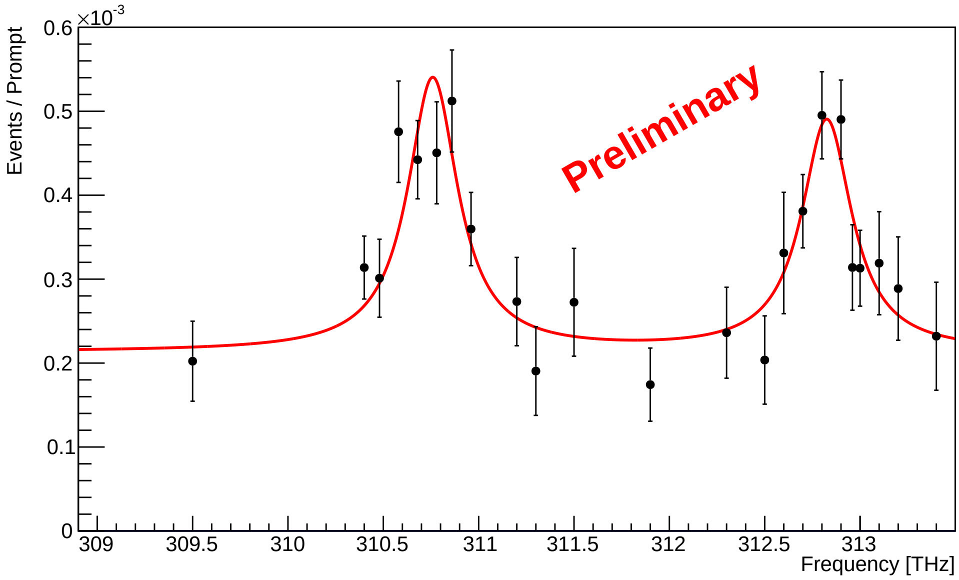

Figure 6.4: Preliminary µ^{3}He$^+$ $2S_{1/2}^{F=0} - 2P_{3/2}^{F=1}$ and $2S_{1/2}^{F=1} - 2P_{1/2}^{F=1}$resonances. The remaining data on µ^{3}He$^+$. The background level is slightly higher compared to the first µ^{3}He$^+$ measurement due to probably laser related problems that still have to be investigated.

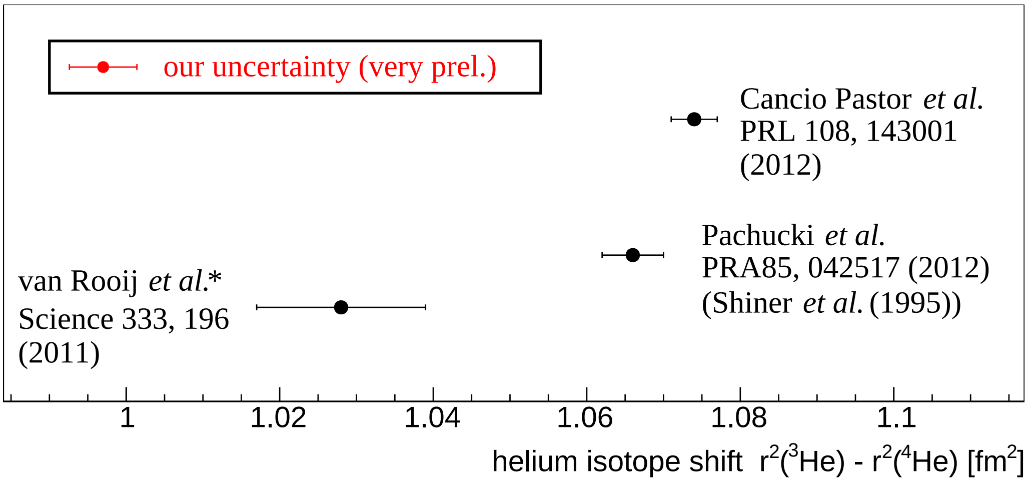

Figure 6.5: Isotope shift in helium. Experimental measurements of the ^{3}He-^{4}He charge radius difference from electronic spectroscopy. The result obtained by [102] shows a more than $3\,\sigma$ deviation from the other two available determinations. The * indicates that the value was slightly shifted due to a theory change after the initial publication. The value of the Shiner measurement [103] was also recently shifted after the theory update [104] and agrees now with the most recent experimental result [105].

6.5 Preliminary μ^3He$^+$ Results

As mentioned in previous chapters, during the 2014 data taking campaign multiple measurements on μ^3He$^+$ were performed. In total three Lamb shift transitions were investigated: $2S_{1/2}^{F=1} - 2P_{3/2}^{F=2}$, $2S_{1/2}^{F=0} - 2P_{3/2}^{F=1}$, and $2S_{1/2}^{F=1} - 2P_{1/2}^{F=1}$. Since data analysis of these measurements is still in a very early phase, only some preliminary results are given here in Fig. 6.3 and Fig. 6.4. The $2S_{1/2}^{F=1} - 2P_{3/2}^{F=2}$ transition was measured with 50 ppm of accuracy while the other transitions were measured with 70 ppm and 90 ppm, respectively.

From these results we will also be able to extract the ^{3}He nuclear rms charge radius with significantly improved accuracy compared to the electronic scattering value of 1.973(16) fm [106], as well as to determine the fine and hyperfine structure in μ^3He$^+$. With both muonic measurements of the ^{4}He and ^{3}He Lamb shifts, the isotope shift between both nuclei can be evaluated in muonic systems. This is an interesting comparison to discrepant results from electronic atom spectroscopy [102–105], see Fig. 6.5. Here, one of the more recent measurements of the helium isotope shift made by laser spectroscopy in a quantum degenerate helium gas shows a significant ($> 3\,\sigma$) offset from other determinations.

6.6 Conclusion

After more than three years of effort, the muonic helium Lamb shift experiment performed by the CREMA collaboration was able to achieve all its goals within just two beam times at PSI. We measured both $\mu^4\mathrm{He}^+$ Lamb shift transitions and were able to determine a new value of the rms charge radius of the alpha particle with more than seven fold improved accuracy compared to previous determinations from electron scattering.

From the measurements, the first experimental determination of the fine structure splitting in muonic atoms could be made. The extracted $\mu^4\mathrm{He}^+$ $2P$ fine structure value is in agreement with the theoretical predictions, being slightly smaller by $1.75\,\sigma$. This could be a hint that there are still uncovered QED terms not accounted for in the summary shown in Tab. 2.3. This will be tested further by the $\mu^3\mathrm{He}^+$ measurements. A possible explanation for the slight offset could also be the increased laser power instability during the data taking of the $2S_{1/2} - 2P_{1/2}$ resonance. Even though drifts were monitored as good as possible (see Sect. 3.5.4), reliable compensation for the total duration of the hour long measurement runs has proven to be difficult. Better long term stability of the Ti:Sa output power and pointing are desirable for future experiments in muonic atoms and ions.

The measured positions of both the $2S_{1/2} - 2P_{3/2}$ and $2S_{1/2} - 2P_{1/2}$ transitions in $\mu^4\mathrm{He}^+$ exclude the previous results reported by Carboni et al. [48, 53] by more than $10\,\sigma$ (for example: $811.68(15)\,\mathrm{nm} \mathrel{\widehat{=}} 369.35(7)\,\mathrm{THz}$, see Fig. 6.6, blue curve). The prediction deduced by postulation of a light vector boson as proposed by Batell et al. [46] could also be excluded. This rules out this particular beyond standard model explanation as a possible solution to the Proton Radius Puzzle (see Fig. 6.6; indicated in purple).

The rms charge radius of the $^4\mathrm{He}$ nucleus extracted in this work is in agreement with the $1.681(4)\,\mathrm{fm}$ value obtained by electron scattering [67] (see Fig. 6.6; indicated in green). Due to the large uncertainty of the electron scattering measurement ($\mathrel{\widehat{=}} 350\,\mathrm{GHz}$ in the $\mu^4\mathrm{He}^+$ LS) it is not possible to exclude a frequency shift comparable in size to the offset that created the proton radius puzzle in muonic hydrogen (75 GHz).

Three Lamb shift transitions in $\mu^3\mathrm{He}^+$were measured in addition which will allow the extraction of the helion rms charge radius and shed light on the discrepancy between the helium isotope shift measurements [102–105].

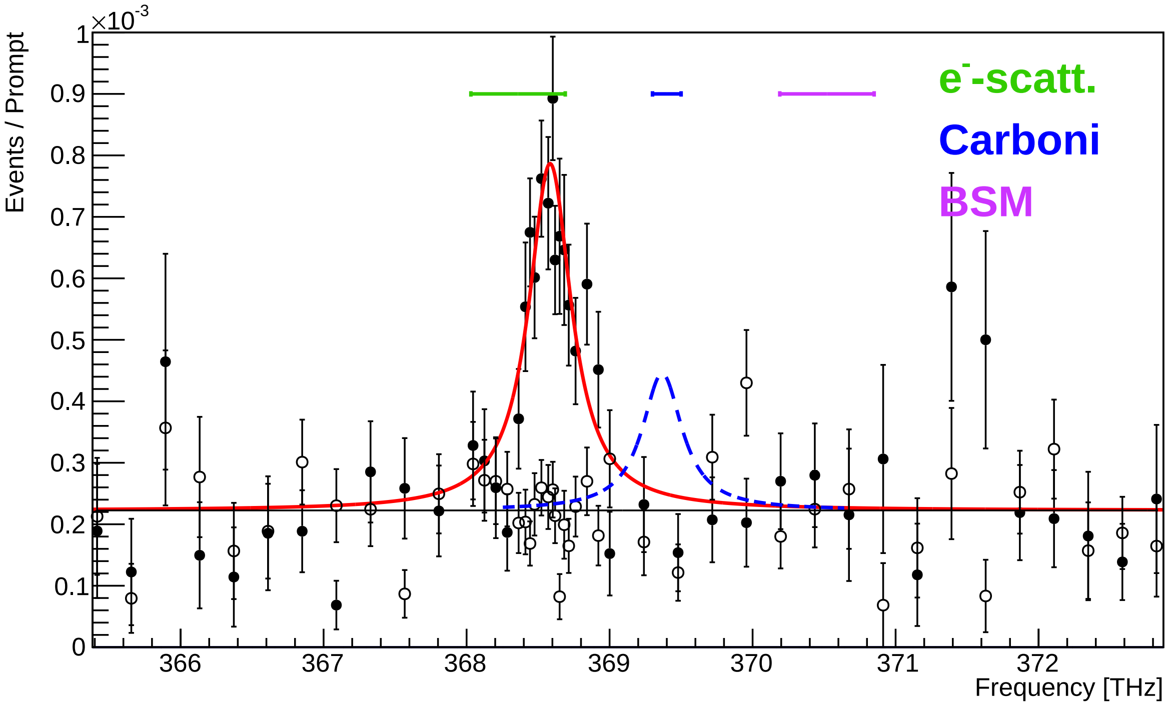

Figure 6.6: Comparison of our data with predictions. Experimental results of the $2S_{1/2} - 2P_{3/2}$ transition with respect to the position reported by the CERN experiments [48, 53] (blue), the calculated position using the ^{4}He nuclear rms charge radius of 1.681(4) [67] (green) and the prediction given by the discussed BSM effect, that could solve the proton radius puzzle in hydrogen [46] (purple; see Sec. 1.2). The amplitude of the indicated CERN resonance corresponds to the signal to noise level in their experiment applied to our background level. The position of our resonance is in agreement with the electron scattering value (green), but there is no significant indication of signals at the CERN measurement and the BSM model.

Appendix A

APD Signal Processing

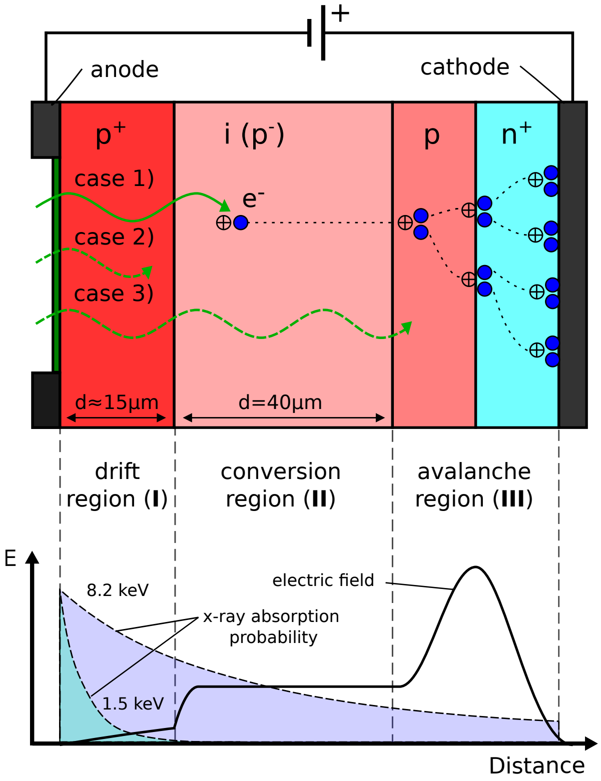
+
anode
cathode
p+
i (p-)
p
n+
case 1)
case 2)
case 3)
e-
d≈15µm
d=40µm
drift region (I)
conversion region (II)
avalanche region (III)
E
8.2 keV
1.5 keV
electric field
x-ray absorption probability
Distance

Figure A.1: Planar APD working principle. Working principle of avalanche photodiodes based on a p^+-i-p-n^+ doping profile. The weakly doped intrinsic part (i) serves as conversion region for most incoming x-rays (case 1). Created photoelectrons are transferred towards the avalanche region. In this high field area, secondary electrons are generated through impact ionization providing charge gain. Low energy x-rays have a high probability of being stopped in the initial drift region (**I**) (case 2). These experience additional signal delay and reduced gain. Some photons convert in the avalanche region (**III**), which also leads to reduced signal amplitudes (case 3). More about this effect can be found in [83]. The lower graph shows the electric field profile in the regions of the APD together with the x-ray absorption profile for 1.5 keV and 8.2 keV x-rays convoluted with the average angle of incidence in our experiment [107].

This chapter is about details in the APD signal analysis that are not directly discussed in the main part of the thesis. To understand the taken measures, a quick overview of the APD working principle is given and depicted in Fig. A.1. In the conversion region (**II**), incoming photons produce primary photo electrons. Differences in the thickness of layer (**II**) give rise to changes in detector energy acceptance. A p-n junction is placed

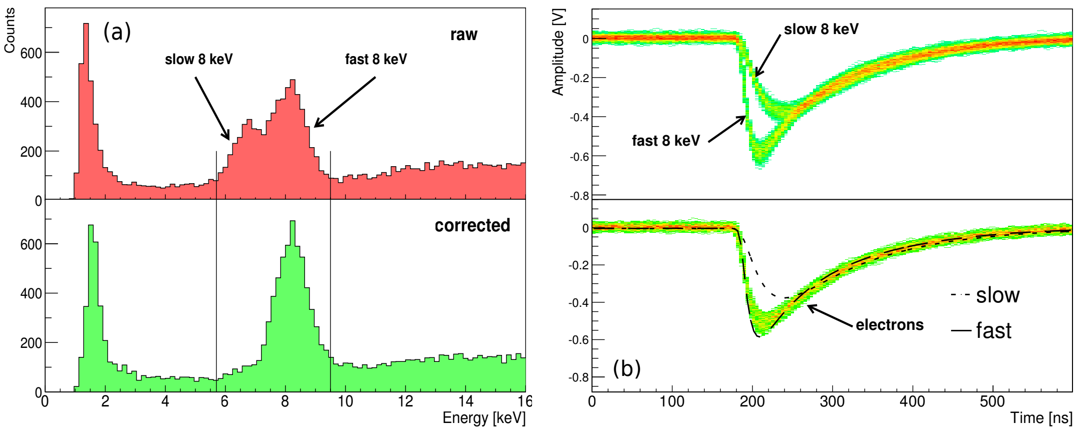

Figure A.2: Energy spectrum and standard traces. Left: X-ray energy spectrum of a single APD before and after applying our improved calibration. The first spectrum is obtained by integrating over the recorded pulse amplitude in a 200 ns time window after the leading edge. A difference in extracted energy for **slow 8 keV** and **fast 8 keV** x-rays is clearly visible. Improved energy calibration managed to unite both responses and improve the energy resolution by up to a factor of 2 (from 32% to 16% FWHM at 8.2 keV for this APD). Right: Typical APD responses for 8.2 keV x-rays (top). Even though incoming x-rays are quasi mono energetic, the APDs show two distinct responses. The **fast 8 keV** component has a rise time of about 35 ns while the **slow 8 keV** component shows a rise time of about 70 ns. Bottom: Electron induced signals that correspond to an x-ray energy of 8.2 keV after calibration. The dashed curves show the average of the **slow 8 keV** and **fast 8 keV** x-rays. One can observe that the electron trace constitutes a mixture of both the other standard responses.

on the back side of the active volume creating high local field strengths. Inside this avalanche region (**III**) electron impact ionization at the high field p-n$^+$ junction leads to a multiplication of free charge carriers, providing gain for the initially converted primary photo electrons [108]. The absorption length for 8 keV x-rays is similar to the APD layer thicknesses and therefore leads to a number of different effects on the APD output, depending on the region where the photon is absorbed. The different possibilities are also shown and explained in Fig. A.1.

The largest part of the recorded 8 keV x-rays stops in the conversion region (**II**) and follows the normal APD working principle that provides high charge collection efficiency and fast amplification. Nevertheless, some x-rays are absorbed either in the drift layer (**I**) or in the avalanche region (**III**). An energy spectrum showing the influence of this effect on the APD energy resolution can be seen in Fig. A.2 (a). The x-rays absorbed in region (**III**) undergo only partial amplification resulting in low amplitudes, possibly down to zero. X-rays absorbed in region (**I**) generate electrons which are slowly transferred to the following region (**II**) due to lower field strengths in (**I**). Defects in this region may hold electrons for non-negligible times, lengthening the pulse and causing a reduction in amplitude [83]. These two contributions of 8.2 keV photons are labeled **slow 8 keV** and **fast 8 keV** respectively, depending on their rise time properties. The shape of the resulting different APD traces can be seen in Fig. A.2 (b).

In order to compensate for these effects and to provide the best possible energy and timing resolution for the x-ray and electron signals recorded by the APDs, a fit of each recorded pulse had to be performed. Since fitting the signals with an analytical shape is a large effort computation wise, standard traces for each APD were created. This facilitated the fitting process drastically by fixing the shape of the fitted pulse, only requiring to match the signal timing and amplitude.

To create the mentioned standard traces, a set of roughly 2.5×10^4 x-ray traces was recorded per APD. The used analysis routine starts with an edge finder (square weighting function with a width of 200 ns) to find the beginning of the pulse in the recorded trace. Then the slope of the leading edge is fitted with a linear function. Using a χ^2 criterion the accuracy of the slope determination is improved by varying the start time of the pulse within 20 ns while keeping the fitting window fixed. An example of typical fits for different amplitudes is given in Fig. A.3.

When the rise time is plotted versus the integral of the pulse, four different contributions to the spectra can be identified as seen in Fig. A.4 (a). The two most prominent peaks are created by **slow 8 keV** and **fast 8 keV** photons. For these peaks a clear difference in rise time and integral is seen while most of the low energy 1.5 keV x-rays show a slow rise time. The rise time distribution for small signals is broadened due to low amplitudes and noise. The last visible component is generated by high energy (up to 50 MeV) electrons. These electrons deposit energies up to 50 keV in the APDs and their signals display a third kind of standard pulse shape, namely a mixture of fast and slow x-ray pulse shapes.

To further analyze the two classes of 8.2 keV x-rays, two sets of APD traces for **slow 8 keV** and **fast 8 keV** were created by selecting the respective peaks in Fig. A.4 (a) with adequate cuts. For each of the two x-ray classes, traces were numerically averaged after shifting each trace to correct for the variation of the pulse starting time. This averaging created the standard traces of the subsets ($\mathbf{Tr_{slow}}$ & $\mathbf{Tr_{fast}}$). The same was done for a set of electron induced signals providing the standard trace $\mathbf{Tr_{elec}}$.

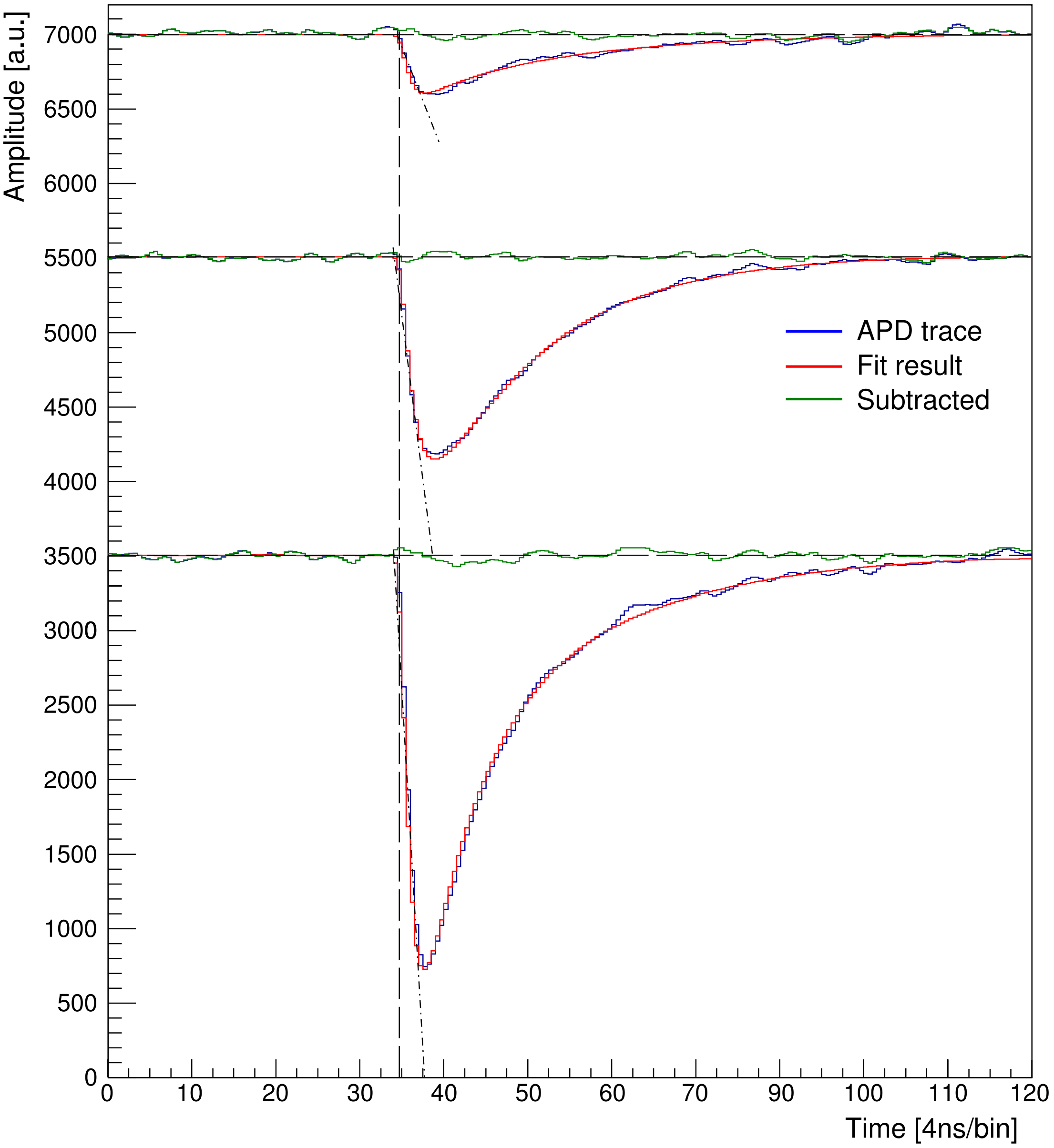

Figure A.3: APD trace fitting results. Results of the fitting routing for three pulses of different amplitude. The first two pulses stems from a 1.5 keV $\mathbf{L}_\alpha$ (top) and 8.2 keV $\mathbf{K}_\alpha$ (middle) x-rays. The largest amplitude signal (bottom) is created by a MeV electron passing through the APD. The dashed lines indicate the baseline level and pulse starting time registered by the routine while the dash-dotted line shows the determined slope of the pulse.

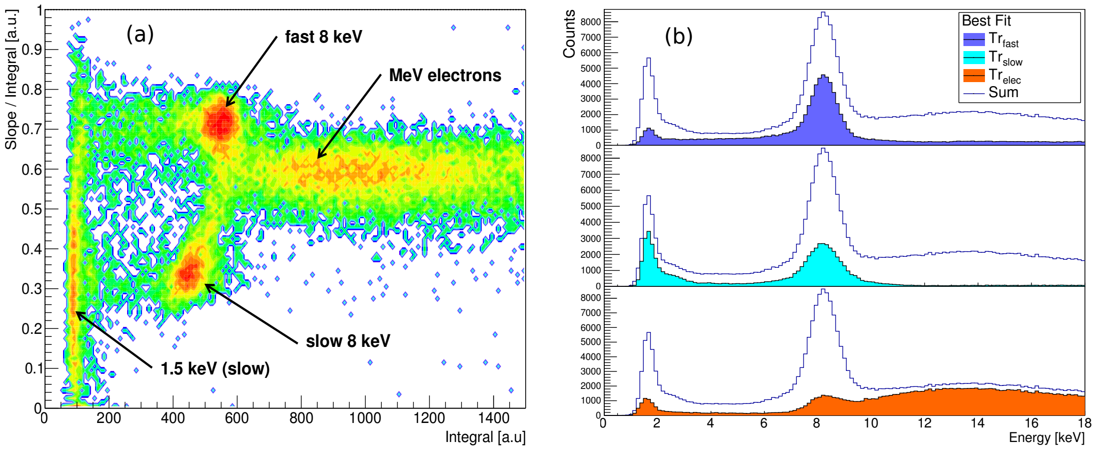

Figure A.4: Rise time spectrum and signal classification. Left: Normalized slope of the rising edge plotted versus the integral of the pulse. Integrals are roughly proportional to the deposited energies of the registered x-rays. Four contributions are visible: Low energy 1.5 keV x-rays show integrals below 200. The recorded 8.2 keV x-rays create two different responses in the APD, one with slow rise time (slope ≈ 0.3), and one with significantly faster rise time (slope ≈ 0.7). The last contribution with an integral above 700 arises from MeV electrons depositing keV energy in the APD. Right: APD signals categorized by the standard trace which provides the lowest χ^2 in a range of 200 ns after the leading edge of the pulse. The fast rising component provided by $\mathbf{Tr_{fast}}$ in dark blue consists mostly out of 8.2 keV x-rays. The light blue distribution stands for all traces that were best described by the slow rising pulse shape $\mathbf{Tr_{slow}}$ and consists mostly out of 1.5 keV x-rays and some 8.2 keV x-rays mixed in. Signals best matching the electron trace $\mathbf{Tr_{elec}}$ are shown in the orange division.

For the final analysis, each APD pulse is fitted with all available standard traces. The timing is then varied and the χ^2 is recorded for each fit. To save computational effort that would arise for a 2-parameter fit (amplitude and time), the amplitude of the standard trace is always fixed by matching its integral to the integral of the signal in a 200 ns wide time window (after baseline subtraction). Finally, the minimal χ^2 between the various standard traces is used to separate the pulses into different classes: **slow 8 keV**, **fast 8 keV** and electrons. The result from the best-fitting class is used to get amplitude, integral and timing values of the recorded signal. The allocation of the recorded APD signals in the **slow 8 keV** and **fast 8 keV** classes according to the fit routine can be seen in the top parts of Fig. A.4 (b). Calibration of the two x-ray spectra created by the $\mathbf{Tr_{slow}}$ and $\mathbf{Tr_{fast}}$ fits is done by matching the peaks to the respective energy of 8.2 keV in separately produced integral spectra for each trace type. As expected, the **fast 8 keV** component of x-rays is the largest part of the recorded signals in our setup as seen in Fig. A.4 (b). The observed 1:1.7 ratio of **fast 8 keV** to **slow 8 keV** x-rays agrees roughly with the expected absorption ratio of 1:1.5 estimated

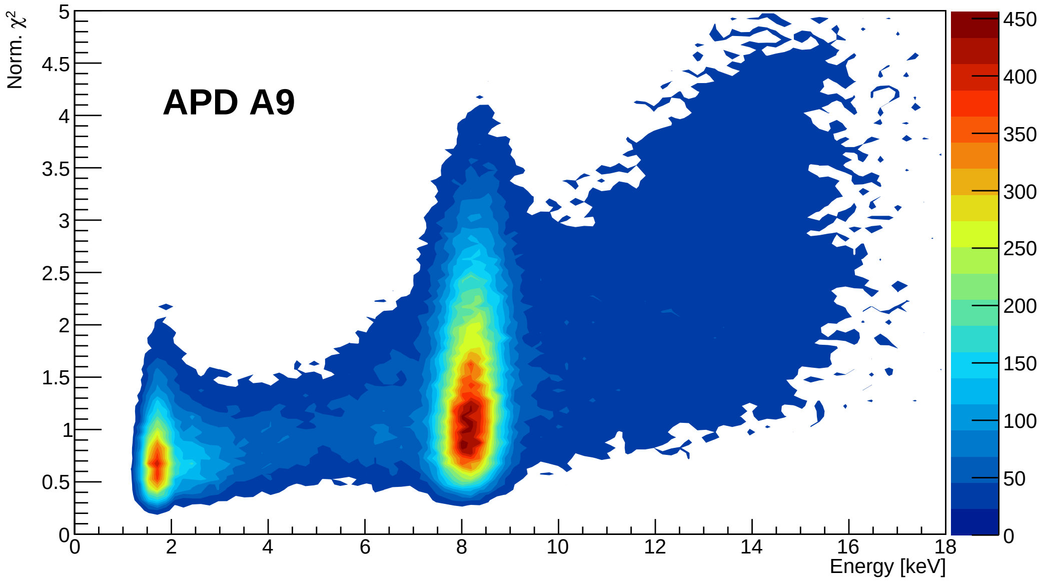

Figure A.5: APD trace fit χ^2 distribution. χ^2 of the trace fitting results of APD A9 normalized to the noise level of the APD channel. The fits of the $\mathbf{K}_\alpha$ (8 keV) and $\mathbf{L}_\alpha$ (1.5 keV) signals provide satisfactory results with χ^2 values close to 1. Since there are no divergently high χ^2 contributions, the fitting routine handles all trace shapes satisfactory. High energy electron signals are fitted worse since the respective standard trace is specifically created for 8 keV signals.

from the thicknesses of layers (**I**) and (**II**). An exemplary χ^2-distribution of the final fits for all mentioned components can be seen in Fig. A.5.

Via the application of the presented fitting and calibration method it was possible to increase the APD energy resolution by a factor of two and therefore drastically reduce the background for the laser spectroscopy measurement.

Appendix B

Cuts and Detector Calibration

The analysis described in Chap. 4 of this work takes terabytes of roughly pre-processed data and transforms it into two resonances of the $\mu^4\mathrm{He}^+$ Lamb shift transitions. A large number of different cuts is required to extract the actual useful events from a huge amount of background. The background stems from a multitude of physical effects but mainly from muon decay electrons. All the cuts required to produce the results shown in Chap. 6 are shortly explained in this appendix, together with the values used to obtain the resonances.

B.1 APD Energy Calibration

The first step ist the energy calibration of all twenty APDs. This has to happen on a run per run basis due to slight drifts in temperature and bias voltage, affecting the gain values of the APDs. For the determination of the second $\mu^4\mathrm{He}^+$ line ($2S_{1/2} - 2P_{1/2}$), the energy calibration shifted within individual runs due to occasional jumps in bias voltage. Muonic helium $\mathbf{K}_\alpha$ x-rays are used for calibrations since they are available with very high statistics and also serve as signal for the spectroscopy. The energy of the $\mathbf{K}_\alpha$ x-rays is known to be 8.22 keV [76] and was therefore used to match the position of the most prominent peak in the energy spectrum (already mentioned in App. A).

B.2 APD Energy Cuts

The measured resonance signals are created by fluorescence x-rays originating from the decay of the 2P-states in the $\mu^4\mathrm{He}^+$ ion. These x-rays are recorded by 20 actively cooled large area avalanche photodiodes and their respective pulses are analyzed with a sophisticated pulse fitting routine as described in App. A. The used routine was able to obtain an energy resolution of 16% (FWHM) for the 8.2 keV $\mathbf{K}_\alpha$ x-rays. Even though this procedure already discards a large part of the background contributions (muon

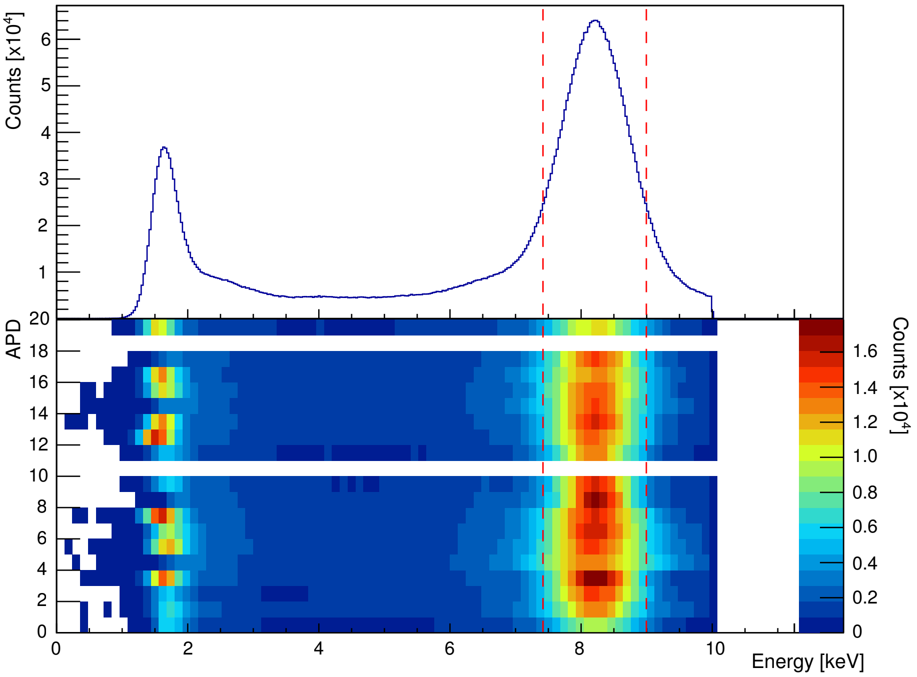

Figure B.1: Analysis APD energy cuts. Energy cuts performed on the different APD spectra. The top plot shows a summed energy spectrum of all 20 APDs, while the bottom one gives an overview over the differences in energy resolution and statistics for the individual APDs. Only detected energies between 7.4 keV and 9.0 keV are eligible to account for µHe $\mathbf{K}_\alpha$ x-rays in the resonance. Signals above 10 keV are directly classified as muon decay electron signals. The energy cut is indicated by the dashed lines. During the 2013 measurement run only 18 APDs were operable since detectors B0 and B8 showed erratic behavior and were therefore disabled.

decay electrons, laser light pulses, etc.) an additional energy cut was placed on the peak signal (see Fig. B.1). This is done to exclude energy regions with too low signal to noise ratios, that are not beneficial for the extraction of the resonance position. The cut providing the best signal to noise ratio on the first measured $2S_{1/2} - 2P_{3/2}$ transition was determined to be 7.4 keV to 9.0 keV. A picture of all APD energy spectra is shown in Fig. B.1 (bottom). It was observed that all 20 APDs share similar energy resolutions, therefore individual energy cuts were not warranted.

Since the APDs are also operating as detectors for muon decay electrons, the energy spectra can be used to pre-identify electrons signals. Even though most electron signals are already correctly identified by the APD signal pulse-shape-analysis (see App. A) some electron background is still present afterwards. Signals with energy larger than 10 keV stem from muon decay electrons with very high probability and are classified as such for further analysis.

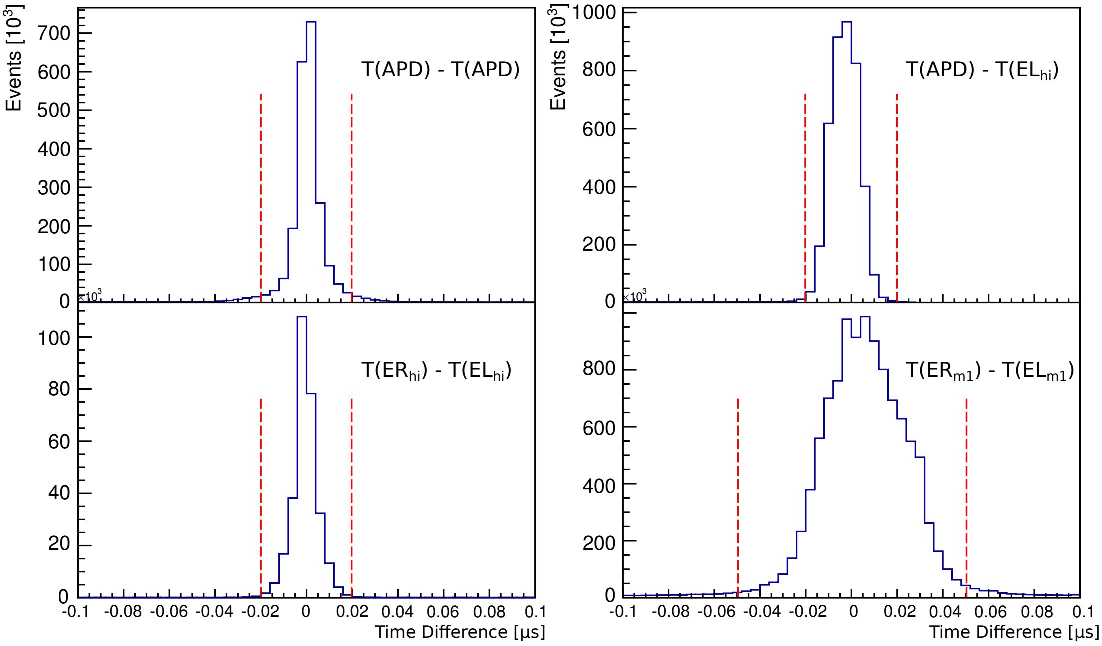

Figure B.2: Coincidence Cuts. Sample time difference spectra between multiple detectors. The dashed lines show the thresholds for the muon decay electron coincidences used as cuts in the analysis.

B.3 Coincidence Cuts

To further reduce the decay electron induced background in the APD spectra coincidences between multiple detectors can be used (see Chap. 4). Muon decay electrons have MeV kinetic energies and can therefore pass multiple centimeters of bulk material. In the strong magnetic field of the experiment (5 T) they perform a spiraling motion with a radius of curvature of a few centimeters on average. On this trajectory they are able to deposit energy in the APDs as well as in the surrounding plastic scintillator paddles.

If a signal is registered in an APD, as well as in one of the electron detector paddles, the APD signal is classified as an electron. For these coincidences all signals in the electron paddles are valid, independent of their amplitude (i.e. their crossed threshold; see Sec. 3.4.4) as long as they are in a matching time window of 40 ns together with an APD signal. An APD signal without coincidence is propagated further as x-ray in the data analysis software.

In addition, coincidences between just two electron paddles are recorded. These electron events show a very good signal to noise ratio up to very late times after the muon

Tidiness	1	2	3	4
Meaning	hi/m2	(m1/lo):(m1/lo)	(hi/m2):(m1/lo)	(hi/m2):(hi/m2)
$\Delta t_{\text{dele\_min}}[\mu\text{s}]$	0.15	0.15	0.15	0.15
$\Delta t_{\text{dele\_max}}[\mu\text{s}]$	6.0	8.0	8.0	8.0

Tidiness	5	6	7	8
Meaning	(APD):(m1/lo)	(APD):(hi/m2)	APD>10 keV	APD$_{\text{e trace}}$
$\Delta t_{\text{dele\_min}}[\mu\text{s}]$	0.15	0.15	0.15	0.15
$\Delta t_{\text{dele\_max}}[\mu\text{s}]$	10.0	10.0	10.0	10.0

Table B.1: Tidiness parameter of the electron classification. Higher tidiness ratings are awarded to electrons that show a more clear electron identification. lo/m1/m2/hi are true electron paddle thresholds and (A):(B) is a signal coincidence between the detectors A and B. Only paddle coincidences with the involments of both left and right paddle are eligible. APD related allocation methods show a better signal to noise ratio compared to signals created only by the electron paddles. Additionally, time difference windows between electrons and x-rays in the delayed electron cut are given for varying electron identification methods. More clean electron classes can have longer windows due to significantly lower background contribution.

entry, while even high amplitude single paddle hits do not. Both are tagged for the further analysis.

The coincidence time window used to find the electron events depends on the time resolution of both the electron paddle scintillator and the APD analysis. To evaluate this time window, the time differences between the sum of all APD signals and the respective crossing of the different paddle thresholds are produced on an event per event basis. Fig. B.2 shows a set of these time difference spectra together with the coincidence window used in the software.

Even though they are not directly necessary for the performed Lamb shift analysis, coincidences between two APD hits are also analyzed and tagged. These events are mostly created by two x-rays emitted during the atomic cascade at prompt times, but can also contain two-photon decay events of the metastable $2S$-state, as will be later discussed in App. C.

B.4 Delayed Electron Cut

Using the mentioned cuts, it is possible to arrange the different detector clicks into so called happenings that correspond to real physical processes in the apparatus [31].

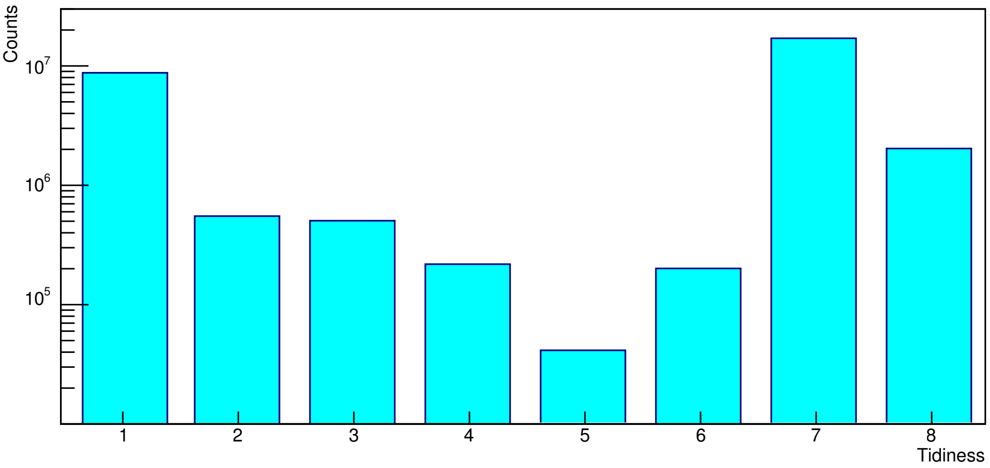

Figure B.3: Electron tidiness distribution. Distribution of the detected electrons sorted corresponding to their tidiness. The biggest contributions are created by APD hits with high energies and single paddle hits (#7 and #1, respectively). Electron signals detected in the trace analysis routine with energies $< 10\,\mathrm{keV}$ provide less statistics (#8, described in App. A).

These can be either created by x-rays or electrons as described in the previous section. In order to avoid double counting of electron signals due to voltage "afterpulsing" created by high amplitude events in the photomultipliers, only signals that are separated by at least a $\Delta t_{same} = 50$ ns are treated as individual particles in the analysis. Additionally, electron happenings are classified by an additional "tidiness" parameter that sorts them according to the best electron determination method that was available for the signal. Tab. B.1 introduces the tidiness parameter and Fig. B.3 gives the respective splitting of electron events in the 2013 measurement run.

Once the classification of x-ray and electron events is completed, the delayed electron cut is employed to further reduce the background. As mentioned in Chap. 4, the requirement of a muon decay electron signal after x-ray emission increases the signal to noise ratio of the measured x-rays drastically. "Fake" x-ray signals created by muon decay electrons can be discarded, since they cannot create a secondary signal in a delayed time window. Therefore, if an additional decay electron is detected significantly after an APD signal, this APD signal stems from a muonic x-ray. These signals are flagged as x-ray + del-e (del-e for delayed electron) and used for the resonance determinations.

Due to different signal to noise ratios of the individual electron identification possibilities, different time windows have to be chosen for the varying tidiness values in order to optimize the overall signal to noise ratio. Tab. B.1 summarizes the eligible time windows for the delayed electron cut.

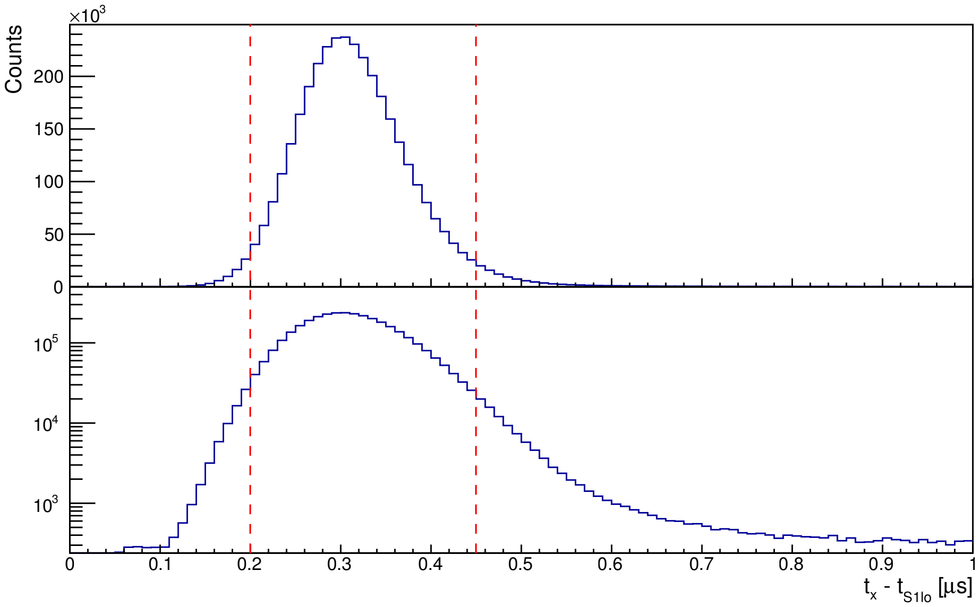

Figure B.4: Second muon cut. Time difference spectrum between the recorded x-rays and the muon entry detector $\mathrm{S1}_{\mathrm{lo}}$ on a linear- and logarithmic scale (top and bottom, respectively). Prompt x-rays are emitted roughly 300 ns after the muon passes the detector. The dashed lines indicate the edges of the second muon cut that is used to discard background events in the laser time window.

B.5 Second Muon Cut

There is a non-negligible probability ($\sim 1\%$) that a second muon enters the gas target during the 20 µs long event-gate. Since the entry time of both muons is completely uncorrelated, the second muon can create unwanted background events in a delayed time window by emitting cascade x-rays. To suppress this effect, the time difference to the last low-amplitude signal of the first muon entry detector $S1_{\mathrm{lo}}$ is recorded for each delayed x-ray. If a signal in S1 is registered ~ 300 ns before the x-ray, this APD signal is flagged as second muon x-ray and is discarded for the analysis. A time difference spectrum between x-rays and the muon entry detector $\mathrm{S1}_{\mathrm{lo}}$ is shown in Fig. B.4 on a linear and log-scale, together with the cut applied in the analysis.

Appendix C

2S-State Lifetime Determination in $\mu^4\text{He}^+$ through Two-Photon Decay

The laser spectroscopy experiment relies strongly on the fraction of µHe-ions that end up in the metastable $2S$-state after the atomic cascade. The biggest influence on the finite lifetime of these ions is given by the decay of the muon. Therefore, the upper lifetime limit is given by the muon lifetime of 2.2 µs [109]. In addition to the muon decay, there is the possibility for the $2S$-state to decay via a two photon quadrupole transition directly to the ground state. The corresponding rate for this process is small ($\Gamma = 1.18{\cdot}10^5\,\text{s}^{-1}$ in muonic helium), four times smaller than the muon decay rate [110]. This decay has previously been studied at 41 hPa [54] and allows the measurement of the μHe $2S$-lifetime directly.

In order to register two-photon events, coincidences between two x-rays have to be observed. The sum of both x-ray energies has to be the $\mathbf{K}_\alpha$ energy of 8.2 keV. The used x-ray coincidence time window is 20 ns, and was determined by observing $\mathbf{K}_\alpha$-$\mathbf{L}_\alpha$ coincidences, happening during the atomic cascade. Fig. C.1 shows a two dimensional energy spectrum for such two x-ray coincidence events for delayed times ($t_x > 0.6$ µs). The recorded spectrum contains the delayed-electron cut and the second muon cut to reduce unwanted backgrounds (see App. B).

Prompt time intervals after muon entry have been excluded for the analysis, since they contain large amounts of $\mathbf{K}_\alpha$-$\mathbf{L}_\alpha$ coincidences that can distort the lifetime determination. To further reduce the background stemming from secondary muons (see App. B), only coincidences were selected where both x-ray energies are above 2.2 keV and below 7.5 keV. This effectively cuts on the two-photon contribution visible in the

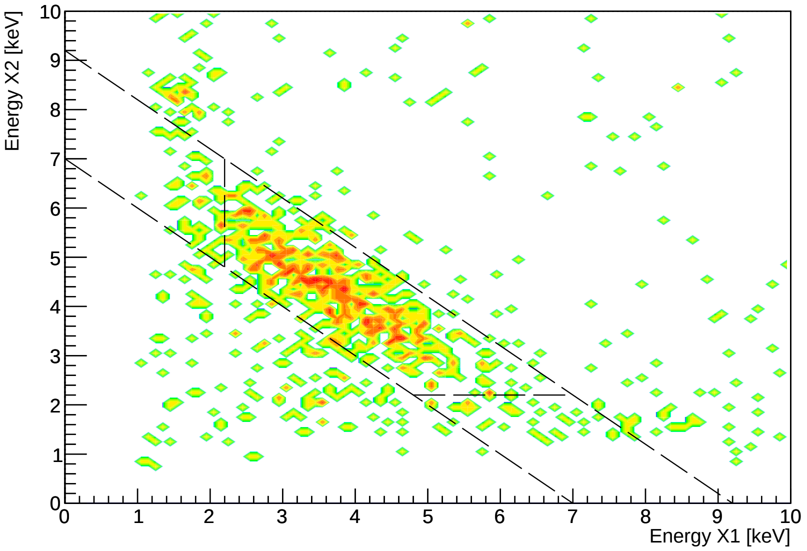

Figure C.1: Energy vs Energy x-ray spectrum of two-photon coincidences. Two dimensional energy spectrum of the first and second x-ray in a two x-ray coincidence at delayed times ($t_x > 0.6\,\mu$s). The diagonal component stems from the two-photon decay of μ^4He$^+$ ions in the $2S$-state. Additional contributions at 1.5 keV are produced by $\mathbf{K}_\alpha$-$\mathbf{L}_\alpha$ coincidences, created by secondary muons undergoing the atomic cascade. The black dashed lines indicate the cuts on the energy sum (diagonal) and the individual x-ray energies (horizontal/vertical).

center of Fig. C.1. A summed energy spectrum of both x-rays involved in the coincidence can be seen in Fig. C.2. A clear peak at the expected $\mathbf{K}_\alpha$ energy is visible.

Additional cuts excluding energies <7.0 keV and >9.5 keV were applied on the summed energy spectrum. From the remaining events a time spectrum was produced to extract the lifetime of the $2S$-state. This spectrum is presented in Fig. C.3 together with an exponential fit of the observed decay. The result of the binned log-likelihood fit gives a total $2S$-state lifetime in μ^4He$^+$ of:

$$\tau(2S)_{\mu^4\mathrm{He}} = 1.71 \pm 0.08\ \mu\mathrm{s}. \tag{C.1}$$

A fit with an additional flat background parameter was performed to verify the previous result. The background value was compatible with zero and did not change the determined lifetime significantly. In total, 542 two-photon coincidences were recorded during the μ^4He$^+$ data taking. This is similar in statistics to the previous measurement at 41 hPa [54] and allows an additional extraction in the 3 hPa regime of our experiment.

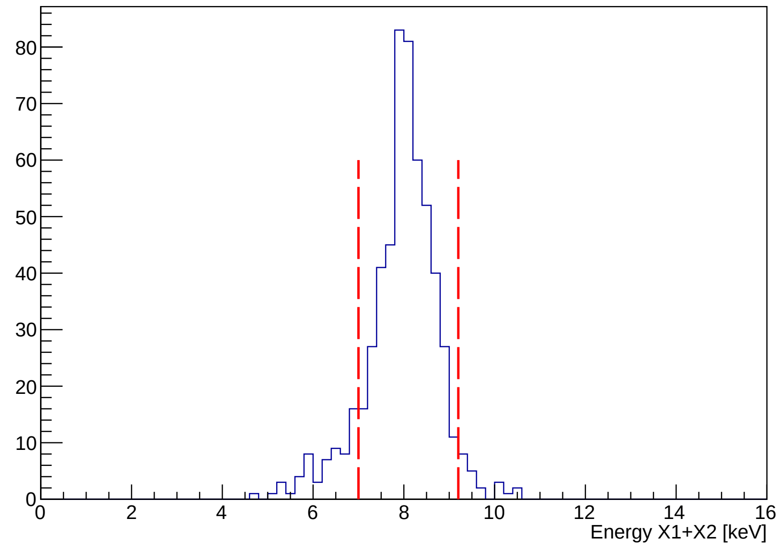

Figure C.2: Summed energy spectrum of two-photon coincidences. Spectrum of the added energy of both x-rays in two x-ray coincidence in a delayed time window ($> 0.6\,\mu$s after muon entry). Only x-ray coincidences with single x-ray energies above 2.2 keV and below 7.5 keV were eligible to avoid $\mathbf{K}_\alpha$-$\mathbf{L}_\alpha$ coincidence in the spectrum. The position matches to the $\mathbf{K}_\alpha$ energy of 8.2 keV. The red dashed line indicates the applied cut for the lifetime extraction.

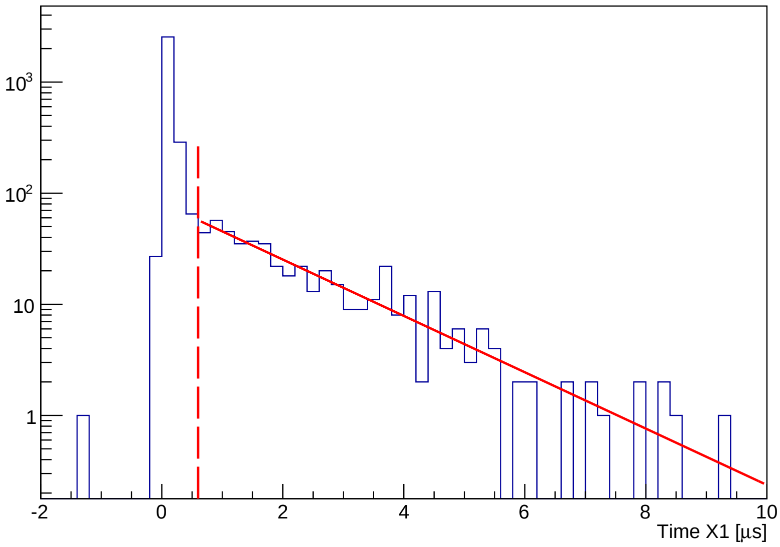

Figure C.3: Time spectrum of two-photon coincidences. Time spectrum of the first x-ray in the selected two-photon events, together with an exponential fit of the determined 1.71 µs lifetime. No significant flat background contribution is visible even at very late times.

Appendix D

Elastic Two-Photon Exchange Contribution to the $\mu^4\mathrm{He}^+$ Lamb shift

The main uncertainty in the extraction of the ^{4}He nuclear rms charge radius is given by the two-photon exchange (TPE) corrections (see in Sec. 2.2). The inelastic polarizability part was already calculated with sufficient accuracy to achieve the goals of the experiment [60]. For the elastic part, the most recent calculation brought up a possible model dependence that depends on the electric form factor (FF) of the alpha particle [55]. The value of the contribution for a gaussian parameterization resulted in 6.61 meV while a dipole model resulted in 7.20 meV [55]. This inconsistency is much larger than the total theoretical and experimental uncertainties, 0.18 meV and 0.07 meV respectively, and had therfore be studied to extract a charge radius with decreased uncertainty from our measurements. In order to investigate this effect, a recalculation of the elastic term was done using Eq. 62 of [55]. To verify the procedure and results, an integration in momentum space was done for a Gaussian and a dipole parameterization of the electric FF [111], providing identical results as the ones in the initial publication. It was found that the elastic TPE contribution only shows a model dependence for momentum transfers <0.5 GeV.

In addition to the FF used in [55], experimentally deduced parameterizations were also studied. One experimental parameterization was taken from [112]:

$$F_\mathrm{e}(q^2) = (1 - (a^2 \cdot q^2)^6) \cdot e^{-b^2 q^2}. \tag{D.1}$$

with the parameters $a = 1.60\,\mathrm{GeV}^{-1}$, $b = 3.42\,\mathrm{GeV}^{-1}$ and where q is the lepton momentum in units of GeV. This parameterization corresponds to a rms charge radius of

1.653 fm.

Additionally a sum of Gaussians (SOG) parameterization of the alpha particle charge density was tested. This parameterization was obtained by a fit of global electron scattering data [113]. Numerical Fourier transformation provided the respective FF parameterization to calculate the elastic TPE contribution. Its series expansion in q^2 was found to be:

$$F_e(q^2) = 1 + a^2 \cdot q^2 + b^4 \cdot q^4 + c^6 \cdot q^6 + d^8 \cdot q^8 + O[q^{10}], \tag{D.2}$$

with the parameters $a = 3.478\,\mathrm{GeV}^{-1}$, $b = 2.883\,\mathrm{GeV}^{-1}$, $c = 2.498\,\mathrm{GeV}^{-1}$ and $d = 2.201\,\mathrm{GeV}^{-1}$. Fig. D.1 gives an overview of the used FF distributions in momentum space. The dipole parameterization significantly deviates from the Gaussian and measured distributions for large momentum transfers. Necessary corrections resulting from the calculations based on the different FF are summarized in Tab. D.1. For momentum transfers >0.5 GeV the two experimental datasets were completed using the values obtained by the Gaussian parameterization. This was done since the accuracy of the Fourier transformation and fit can not be guaranteed for larger momentum transfers. The final value for the elastic TPE contribution was determined by integration in momentum space:

$$\Delta E^{\mathrm{TPE}}_{\mathrm{elastic}} = 1.40(2)\,\mathrm{meV/fm}^3. \tag{D.3}$$

Its uncertainty is given by the spread between the experimental and the Gaussian values. The dipole parameterization is neglected due to incompatibility with the experimental FF shapes.

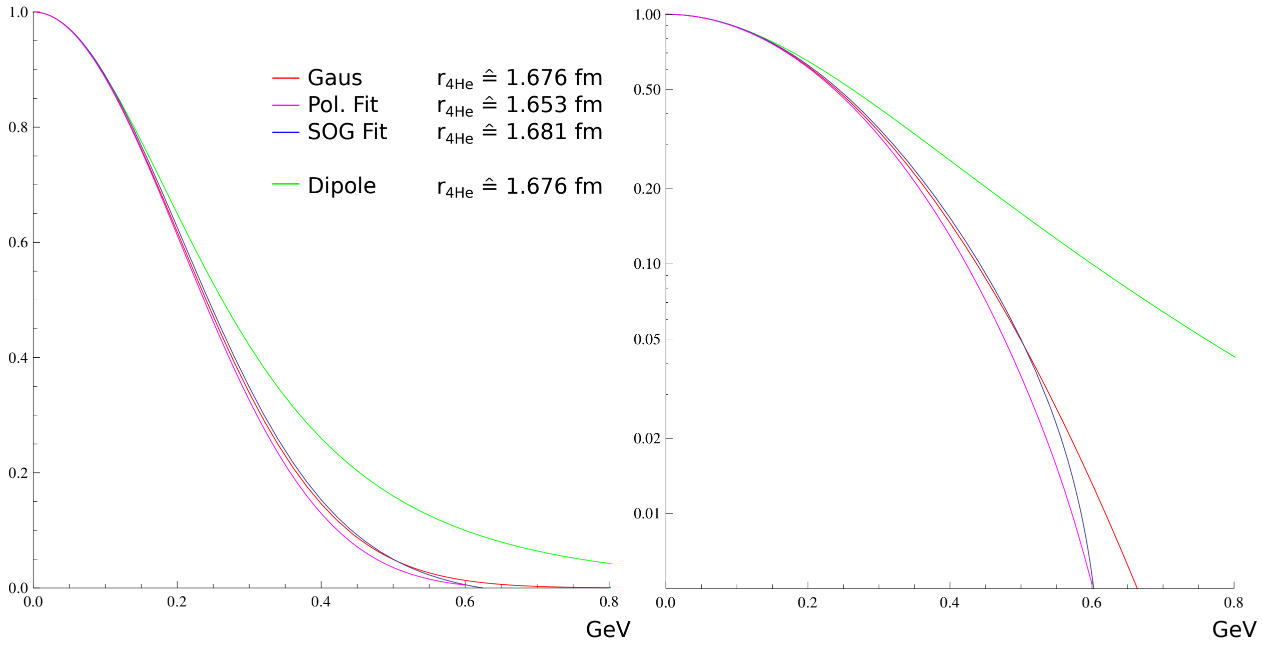

Figure D.1: Form factor functions used for TPE calculation. Parameterizations of the alpha particle electric form factor. Shown are calculated Gaussian and dipole functions together with two experimentally deduced parameterizations [112, 113]. The experimental results agree with the Gaussian shape, but not with the dipole parameterization.

Integration Limits [GeV]		[0,0.01]	[0.01,0.1]	[0.1,0.5]	[0.5,1]	[1,10]	[10,100]	[100,10^3]	[10^3,10^4]		
FF Parameterization	Corresponding rms radius $r_{4\mathrm{He}}$	Resulting corrections [meV]								Sum. corr.	Sum/$r^3_{4\mathrm{He}}$
Gaus	1.676 fm	0.13782	1.20881	3.11877	1.02453	1.00283	0.10670	0.01017	0.00102	6.60562	1.403
Meas. [112]	1.653 fm	0.13063	1.14636	2.98665	*	*	*	*	*	6.40381	1.418
SOG [113]	1.681 fm	0.13571	1.19282	3.11627	*	*	*	*	*	6.81045	1.386
Dipole	1.676 fm	0.17141	1.48526	3.39771	1.02560	1.00284	0.10670	0.01017	0.00102	7.19567	1.528

Table D.1: Elastic TPE values determined from the calculation. Integrals of the elastic TPE correction for different electric form factor models and momentum transfer ranges. Calculations are done for Gaussian and dipole parameterizations of the electric form factor, as well as with a measured shape from electron scattering experiments [112] and a Fourier transformation of an experimental sum of Gaussian (SOG) fit of the alpha particle charge density [113]. Contributions for momentum transfers $\geq 0.5\,\mathrm{GeV}$ were found to be independent of the form factor model. Therefore the values of the Gaussian parameterization were used to fix the experimental values in this region (indicated by *). The summed correction divided by $r^3_{4\mathrm{He}}$ provides the parameter needed to parameterize the elastic TPE contribution.

Appendix E

Systematic Studies of Fit Results

Numerous different cuts and parameters are contributing to the datasets that are fitted using the line shape model described in Chap. 4. Therefore a certain degree of systematic studies has to be done in order to verify the fit results. Using different sub-datasets with varied parameters the stability of the analysis was tested. This included fitting the resonances with the fixed calculated linewidth, the disabling of laser power normalization, fits discarding the laser-off data, etc. The different approaches are summarized in Tab. E.1 and Tab. E.2.

It was observed that none of the results for both the center line position and the linewidth differed by more than 1 σ from the default dataset. The fits are very robust and provide confidence in the accuracy of the results.

During the first data taking period in 2013 the laser time delay had to be changed by about 50 ns. This could lead to a roughly 3 % change in signal amplitude between data points with short and long delay. A shift of the center position by this effect has an upper limit of ≈50 GHz for the $2S_{1/2} - 2P_{3/2}$ resonance. Since the measured frequency in the experiment was chosen evenly on both sides of the resonance between successive runs, effectively reducing the effect, we ignored this possibility.

Slight irregularities were found studying the delayed electron detection in both transitions, as can be seen in Tab. E.1 and Tab.E.2. These irregularities were probably created by unwanted signals in the paddle photo multipliers during the data taking runs that could fake additional delayed electrons events. Corresponding events were mostly avoided in the analysis by discarding events were seemingly multiple electrons appeared during the running acquisition.

Dataset	Center [THz]		Width [THz]		Ampl. [$10^{-}3$]		BG. [$10^{-}3$]	
Default	368.660	± 0.017	0.340	± 0.052	5.64	± 0.51	2.23	± 0.14
Without lasernorm.	368.660	± 0.017	0.341	± 0.053	5.58	± 0.51	2.23	± 0.14
Fixed width	368.658	± 0.016	0.320		5.76	± 0.43	2.24	± 0.13
Without loff	368.661	± 0.017	0.354	± 0.055	5.72	± 0.51	2.12	± 0.18
Allow 2nd xray	368.659	± 0.017	0.343	± 0.054	5.56	± 0.50	2.20	± 0.14
Mintidy = 2 / no padhi	368.683*	± 0.028	0.458*	± 0.086	5.21	± 0.54	1.40	± 0.15
Maxtidy = 1 / only padhi	368.644*	± 0.021	0.250*	± 0.071	6.54	± 1.11	3.30	± 0.25
Allow 2nd electron	368.648*	± 0.017	0.340	± 0.052	5.64	± 0.51	2.23	± 0.14
Tight Ecut (0.74-0.88 keV)	368.657	± 0.017	0.332	± 0.053	5.80	± 0.56	2.03	± 0.14
No secondcut	368.650	± 0.021	0.357	± 0.065	5.41	± 0.55	3.65	± 0.18
Deletime <4 μs	368.674*	± 0.019	0.336	± 0.056	5.13	± 0.52	1.67	± 0.13
Delewindow 0.6-4 μs	368.664	± 0.018	0.352	± 0.055	5.88	± 0.55	1.91	± 0.14
Delewindow >2 μs	368.641*	± 0.022	0.196*	± 0.084	6.24	± 0.97	2.69	± 0.23

Table E.1: $2S_{1/2} - 2P_{3/2}$ **transition fit systematics.** Fit results of various supplementary sub-datasets of the $2S_{1/2} - 2P_{3/2}$ transition. Given are the center frequency, resonance linewidth as well as signal and background amplitudes. The “default” dataset is the one used for the determination of the results in Chap. 6. Fit parameters that vary more than $0.5\,\sigma$ from the normal dataset are indicated with a *.

Dataset	Center [THz]		Width [THz]		Ampl. [10^{-}3]		BG. [10^{-}3]	
Default	333.352	± 0.016	0.292	± 0.054	4.21	± 0.46	1.28	± 0.18
Without lasernorm.	333.347	± 0.015	0.291	± 0.056	4.20	± 0.45	1.16	± 0.19
Fixed width	333.353	± 0.016	0.320		4.12	± 0.41	1.13	± 0.15
Without loff	333.355	± 0.015	0.343*	± 0.067	4.55	± 0.46	1.14	± 0.28
Allow 2nd xray	333.351	± 0.015	0.286	± 0.054	4.06	± 0.45	1.29	± 0.18
Mintidy = 2 / no padhi	333.367*	± 0.017	0.297	± 0.061	4.43	± 0.54	0.79	± 0.20
Maxtidy = 1 / only padhi	333.325*	± 0.032	0.294	± 0.111	3.84	± 0.80	2.18	± 0.44
Allow 2nd electron	333.346	± 0.017	0.346*	± 0.090	3.87	± 0.42	3.22	± 0.22
Tight Ecut (0.74-0.88 keV)	333.333*	± 0.020	0.383*	± 0.110	3.78	± 0.43	1.20	± 0.23
No secondcut	333.356	± 0.018	0.326	± 0.068	4.16	± 0.47	1.90	± 0.23
Deletime <4 μs	333.354	± 0.018	0.321	± 0.062	3.78	± 0.43	0.87	± 0.16
Delewindow <4 μs	333.358	± 0.017	0.296	± 0.054	4.19	± 0.48	1.15	± 0.18
Delewindow >2 μs	333.359	± 0.026	0.277	± 0.115	3.90	± 0.77	1.72	± 0.37

Table E.2: **$2S_{1/2} - 2P_{1/2}$ transition fit systematics.** Fit results of various supplementary sub-datasets of the $2S_{1/2} - 2P_{1/2}$ transition. Given are the center frequency, resonance linewidth as well as signal and background amplitudes. The "default" dataset is the one used for the determination of the results in Chap. 6. Fit parameters that vary more than $0.5\,\sigma$ from the normal dataset are indicated with a *.

Bibliography

[1] R. Pohl et al. “The size of the proton”. *Nature* **466**, p. 213 (2010).

[2] T. Nebel et al. “The Lamb-shift experiment in muonic helium”. *Hyp. Interact.* **212**, p. 195 (2012).

[3] T. Adam et al. “Measurement of the neutrino velocity with the opera detector in the cngs beam”. *arXiv* 1109.4897v4.

[4] J. C. Bernauer and R. Pohl. “The proton radius puzzle”. *Sci. Am.* **310**, p. 32 (2014).

[5] R. Pohl et al. “Muonic hydrogen and the proton radius puzzle”. *Ann. Rev. Nucl. Part. Sci.* **63**, p. 175 (2013).

[6] J. J. Balmer. “Notiz über die Spektrallinien des Wasserstoffs”. *Ann. Phys.* **261**, p. 80 (1885).

[7] N. Bohr. “On the constitution of atoms and molecules”. *Phil. Mag.* **26**, p. 1 (1913).

[8] C. G. Parthey et al. “Improved measurement of the hydrogen 1S-2S transition frequency”. *Phys. Rev. Lett.* **107**. (2011) 203001.

[9] C. G. Parthey et al. “Precision measurement of the hydrogen 1S-2S frequency via a 920-km fiber link”. *Phys. Rev. Lett.* **110**. (2013) 230801.

[10] H. Bethe and E. Salpeter. *Quantum Mechanics of One and Two electron Systems* (Springer, 1957).

[11] W. E. Lamb. “Fine structure of the hydrogen atom by a microwave method”. *Phys. Rev.* **72**, p. 241 (1947).

[12] “Quantum Mechanics Lecture, Utah State University, http://ocw.usu.edu/physics/classical-mechanics/pdf_lectures/31.pdf” Accessed: 2015-07-15.

[13] Courtesy of the CREMA Collaboration.

[14] P. J. Mohr et al. “Codata recommended values of the fundamental physical constants: 2006”. *Rev. Mod. Phys.* **80**, p. 633 (2008).

[15] A. Antognini et al. “Proton structure from the measurement of the 2S-2P transition frequencies of muonic hydrogen”. *Science* **229**, p. 417 (2013).

[16] I. Sick. “On the rms-radius of the proton”. *Phys. Lett. B* **576**, p. 62 (2003).

[17] J. C. Bernauer. “Priv. comm.” .

[18] R. Hofstadter and W. McAllister. “Electron scattering from the proton”. *Phys. Rev.* **98**, p. 217 (1955).

[19] http://www.scholarpedia.org/article/Nucleon_Form_factors Accessed: 2015-04-24.

[20] J. C. Bernauer et al. “High-precision determination of the electric and magnetic form factors of the proton”. *Phys. Rev. Lett.* **105**. (2010) 242001.

[21] R. J. Hill and G. Paz. "Model independent extraction of the proton charge radius from electron scattering". *Phys. Rev. D* **82**. (2010) 113005.

[22] M. Vanderhaegern and T. Walcher. "Long range structure of the nucleon". *arXiv* 1008.4225v1.

[23] I. T. Lorenz et al. "The size of the proton: Closing in on the radius puzzle". *Eur. Phys. J. A* **48**, p. 151 (2012).

[24] F. Biraben et al. "Two-photon spectroscopy of atomic hydrogen new measurement of the rydberg constant". *Europhys. Lett.* **2**, p. 925 (1986).

[25] C. Schwob et al. "Optical frequency measurement of the 2S-12D transitions in hydrogen and deuterium: Rydberg constant and Lamb shift determinations". *Phys. Rev. Lett.* **82**, p. 4960 (1999). Erratum: Phys. Rev. Lett. **86**, p. 4193 (2001).

[26] P. J. Mohr et al. "Codata recommended values of the fundamental physical constants: 2010". *Rev. Mod. Phys.* **84**, p. 1527 (2012).

[27] A. Beyer et al. "Precision spectroscopy of the 2s-4p transition in atomic hydrogen on a cryogenic beam of optically excited 2s atoms". *Ann. Phys.* **525**, p. 671 (2013).

[28] E. Peters et al. "Frequency-comb spectroscopy of the hydrogen 1s-3s and 1s-3d transitions". *Ann. Phys.* **525**, p. L29 (2013).

[29] Palchikov et al. "Measurement of the Lamb shift in H, n=2". *Metrologia* **21**, p. 99 (1985).

[30] E. Hessels. "Progress towards a new microwave measurement of the hydrogen n=2 Lamb shift: a measurement of the proton charge radius". *ECT* Workshop* .

[31] T. Nebel. *The Lamb Shift in Muonic Hydrogen.* Ph.D. thesis, Ludwig-Maximilians University Munich (2010). http://edoc.ub.uni-muenchen.de/12094/.

[32] K. Pachucki. "Theory of the Lamb shift in muonic hydrogen". *Phys. Rev. A* **53**. (1996) 2092.

[33] K. Pachucki. "Proton structure effects in muonic hydrogen". *Phys. Rev. A* **60**. (1999) 3593.

[34] P. Indelicato. "Non-perturbative evaluation of some qed contributions to the muonic hydrogen n=2 Lamb shift and hyperfine structure". *arXiv* 1210.5828v2.

[35] S. G. Karshenboim et al. "Relativistic recoil corrections to the electron-vacuum- polarization contribution in light muonic atoms". *Phys. Rev. A* **85**. (2013) 032509.

[36] A. Antognini et al. "Theory of the 2S-2P Lamb shift and hyperfine splitting in muonic hydrogen". *Ann. Phys.* **331**, p. 127 (2013).

[37] G. A. Miller. "Toward a resolution of the proton size puzzle". *Phys. Rev. A* **84**. (2011) 020101.

[38] G. A. Miller. "Proton polarizability contribution: Muonic hydrogen lamb shift and elastic scattering". *Phys. Rev. B* **718**, p. 1078 (2013).

[39] J. M. Alarcon. "Chiral perturbation theory of muonic-hydrogen Lamb shift: polarizability contribution". *Eur. Phys. J. C* **74**, p. 2852 (2014).

[40] B. R. Holstein and A. M. Nathan. "Dispersion relations and the nucleon polarizability". *Phys. Rev. D* **49**, p. 6101 (1994).

[41] C. E. Carlson et al. "Higher-order proton structure corrections to the lamb shift in muonic hydrogen". *Phys. Rev. A* **84**. (2011) 020102.

[42] U. D. Jentschura. "Lamb shift in muonic hydrogen. II. analysis of the discrepancy of theory and experiment". *Ann. Phys.* **326**, p. 516 (2011).

[43] U. D. Jentschura. "Light sea fermions in electron-proton and muon-proton interactions". *Phys. Rev. A* **88**. (2013) 06514.

[44] G. A. Miller. “Nonperturbative lepton-sea fermions in the nucleon and the proton radius puzzle”. *Phys. Rev. C* **91**. (2015) 055204.

[45] G. W. Bennet. “Measurement of the negative muon anomalous magnetic moment to 0.7 ppm”. *Phys. Rev. Lett.* **92**. (2004) 161802.

[46] B. Batell et al. “New parity-violating muonic forces”. *Phys. Rev. Lett.* **107**. (2011) 011803.

[47] D. Tucker-Smith and I. Yavin. “Muonic hydrogen and mev forces”. *Phys. Rev. D* **83**. (2010) 101702.

[48] G. Carboni et al. “Precise measurement of the $2S_{1/2}$-$2P_{3/2}$ splitting in the $\mu^{-4}He^{+}$ muonic ion”. *Nucl. Phys. A* **278**, p. 381 (1977).

[49] A. Placci et al. “Observation of muonic x-ray in helium gas and the measurement of the two-photon decay rate of the 2S metastable state”. *Nuovo Cimento A* **1**, p. 445 (1971).

[50] E. Z. L. Bracci. *Electromagnetic Cascade and Chemistry of Exotic Atoms* (Springer, 1990).

[51] H. P. von Arb et al. “Measurement of the lifetime and quenching rate of metastable 2s muonic helium ions”. *Phys. Lett. B* **4**, p. 136 (1984).

[52] A. Bertin et al. “Measurement of the $2P_{3/2}$-$2S_{1/2}$ splitting in the $\mu^{-4}He^{+}$ muonic ion by means of a tunable infrared dye-laser”. *Phys. Lett. B* **55**, p. 411 (1975).

[53] G. Carboni et al. “Measurement of the $2S_{1/2}$-$2P_{1/2}$ splitting in the $\mu^{-4}He^{+}$ muonic ion”. *Phys. Lett. B* **78**, p. 229 (1978).

[54] H. Hauser et al. “Search for the 2S-2P energy difference in muonic ^{4}He ions”. *Phys. Rev. A* **46**, p. 2363 (1992).

[55] A. A. Krutov et al. “Theory of the Lamb shift in muonic helium ions”. *JETP Lett.* **120**, p. 73 (2015).

[56] E. Borie. “Lamb shift in light muonic atoms - revisited”. *arXiv* 1103.1772v7.

[57] U. D. Jentschura et al. “Semi-analytic approach to higher-order corrections in simple muonic bound systems: Vacuum polarization, self-energy and radiative-recoil”. *Eur. Phys. J. D* **65**, p. 357 (2011).

[58] E. Y. Korzinin et al. “$\alpha^2(Z\alpha)^4$ contribution to the Lamb shift and the fine structure in light muonic atoms”. *Phys. Rev. D* **88**. (2013) 125019.

[59] S. G. Karshenboim et al. “Contribution of light-by-light scattering to energy levels of light muonic atoms”. *JETP Lett.* **92**, p. 8 (2010).

[60] C. Ji et al. “Nuclear polarization effects in muonic atoms”. *Few–Body Systems* **55**, p. 917 (2014).

[61] C. Ji et al. “Nuclear polarization corrections in the $\mu^{4}He^{+}$ Lamb shift”. *Phys. Rev. Lett.* **111**. (2013) 143402.

[62] U. D. Jentschura. “Relativistic reduced-mass and recoil corrections to vacuum polarization in muonic hydrogen, muonic deuterium, and muonic helium ions, theory of the n=2 levels in muonic deuterium”. *Phys. Rev. A* **84**. (2015) 012505.

[63] K. Pachucki. “Nuclear structure corrections in muonic deuterium”. *Phys. Rev. Lett.* **106**. (2011) 193007.

[64] C. E. Carlson et al. “Nuclear-structure contribution to the Lamb shift in muonic deuterium”. *Phys. Rev. A* **89**. (2014) 022504.

[65] M. Gorshteyn, C. E. Carlson, and S. Bacca. “Priv. comm.” .

[66] E. N. Elekina et al. "Fine structure of the muonic ^{4}He ion". *Phys. Part. Nucl.* **8**, p. 331 (2011).

[67] I. Sick. "Precise root-mean-square radius of 4he". *Phys. Rev. C* **77**. (2008) 041302.

[68] J. L. Friar. "Nuclear polarization corrections in μ^4He atoms". *Phys. Rev. C* **16**, p. 1540 (1977).

[69] F. B. Dittus. *Experimentelle Untersuchung Ueber Bildung und Zerfall myonische Heliumionen im Metastabilen 2S-Zustand.* Ph.D. thesis, ETH Zurich (1985). http://e-collection.library.ethz.ch/view/eth:36748.

[70] G. Reifenröther et al. "Cascade in muonic helium atoms". *Phys. Lett. B* **191**, p. 15 (1987).

[71] S. L. Meyer et al. "Precision lifetime measurements on positive and negative muons". *Phys. Rev. C* **132**. (1963) 002693.

[72] D. F. Measday. "The nuclear physics of muon capture". *Phys. Rep.* **354**, p. 243 (2001).

[73] K. Schuhmann et al. "Thin-disk laser for the measurement of the radii of the proton and the alpha-particle". *Adv. Solid-State Lasers Congress* p. ATu3A.46.

[74] K. Schuhmann et al. "Thin-disk laser multi-pass amplifier". *Proc. SPIE* **342**. (2015) 93420U.

[75] J. Vogelsang et al. "Multipass laser cavity for efficient transverse illumination of an elongated volume". *Optics Express* **22**. (2014) 13052.

[76] G. Backenstoss et al. "Pionic and muonic x-ray transitions in liquid helium". *Nucl. Phys. A* **232**, p. 519 (1974).

[77] L. Ludhova et al. "Planar LAAPDS: temperature dependence, performance and application in low-energy x-ray spectroscopy". *Nucl. Inst. Meth. A* **540**, p. 169 (2005).

[78] L. M. P. Fernandes et al. "Characterization of large area avalanche photodiodes in x-ray and VUV-light detection". *Journ. of Inst.* **2**. (2007) P08005.

[79] M. Diepold et al. "Improved x-ray detection and particle identification with avalanche photodiodes". *Rev. Sci. Instrum.* **86**. (2015) 053102.

[80] D. P et al. "A new method to produce a negative muon beam of kev energies". *Nucl. Inst. Meth. A* **394**, p. 287 (1997).

[81] L. Simons. "Die Zyklotronfalle". *Phys. Bl.* **48**, p. 261 (1992).

[82] A. Antognini. *The Lamb shift experiment in muonic hydrogen.* Ph.D. thesis, Ludwig-Maximilians University Munich (2001). http://edoc.ub.uni-muenchen.de/5044/.

[83] A. Q. R. Baron et al. "A fast, convenient, x-ray detector". *Nucl. Inst. Meth. A* **400**, p. 124 (1997).

[84] K. F. Wall and A. Sanchez. "Titanium sapphire lasers". *The Lincoln Laboratory Journal* **3**, p. 447 (1990).

[85] A. Antognini et al. "Thin-disk Yb:YAG oscillator-amplifier laser, ASE, and effective Yb:YAG lifetime". *IEEE J. Quant. Electr.* **45**, p. 993 (2009).

[86] B. Weichelt et al. "Enhanced performance of thin-disk lasers by pumping into the zero-phonon line". *Optics Letters* **37**, p. 3045 (2012).

[87] A. Giesen et al. "Scalable concept for diode-pumped high-power solid state lasers". *Appl. Phys.* **58**, p. 365 (1994).

[88] J. Krauth. *A monitoring system for the light distribution in a multipass cavity at the μHe^+ Lamb shift experiment.* Master's thesis (2014).

[89] https://midas.triumf.ca/MidasWiki/index.php Accessed: 2015-05-7.

[90] HTTPS://ROOT.CERN.CH Accessed: 2015-05-7.

[91] P. INDELICATO. "Priv. comm." .

[92] J. GÖTZFRIED. *Direct measurement of the 2S-lifetime in muonic* $^4He^+$ *Ions.* Master's thesis (2014).

[93] HTTP://EN.WIKIPEDIA.ORG/WIKI/LANDE G-FACTOR Accessed: 2015-04-24.

[94] R. POHL. "Priv. comm." .

[95] M. DIEPOLD. *Lifetime and population of the 2S-state in muonic hydrogen and deuterium.* Master's thesis (2012).

[96] W. DEMTRÖDER. *Laser Spectroscopy 1* (Springer, 1981).

[97] G. Y. KORENMANN ET AL. "Collisional shift and broadening of the 2p-2s spectral lines in muonic helium ions". *Phys. Rev. A* **88**. (2013) 032503.

[98] B. NAAR. *Contribution to the muonic helium Lamb shift experiment: Frequency calibration of the laser system.* Master's thesis (2014).

[99] C. J. SANSONETTI and M. B. GREENE. "Infrared spectrum and revised energy levels for neutral krypton". *Phys. Scripta* **75**, p. 577 (2007).

[100] T. UDEM ET AL. "Absolute optical frequency measurement of the ceasium D2 line". *Phys. Rev. A* **62**. (2000) 031801.

[101] E. B. SALOMAN. "Energy levels and observed spectral lines of krypton, Kr I through Kr XXXVI". *J. of. Phys. and. Chem. Data Rep.* **36**, p. 251 (2007).

[102] R. VAN ROOIJ ET AL. "Frequency metrology in quantum degenerate helium: Direct measurement of the 2 3s1 - 2 1s0 transition". *Science* **333**, p. 196 (2011).

[103] S. SHINER ET AL. "Three-nucleon charge radius: A precise laser determination using 3He". *Phys. Rev. Lett.* **74**, p. 3553 (1995).

[104] K. PACHUCKI ET AL. "Quantum electrodynamic calculation of the hyperfine structure of 3He". *Phys. Rev. A* **85**. (2012) 042517.

[105] P. CANCIO PASTOR ET AL. "Frequency metrology of helium around 1083 nm and determination of the nuclear charge radius". *Phys. Rev. Lett.* **108**. (2012) 143001.

[106] I. SICK. "Form factors and radii of light nuclei". *arXiv* 1505.06924v1.

[107] HTTP://HENKE.LBL.GOV/OPTICAL_CONSTANTS/ATTEN2.HTML Accessed: 2015-02-18.

[108] D. RENKER and E. LORENZ. "Advances in solid state photon detectors". *Journ. of Inst.* **4**. (2009) P04004.

[109] J. BERINGER ET AL. "2013 review of particle physics". *Phys. Rev. D* **86**. (2012) 010001.

[110] R. BACHER. "Decay rates of the metastable states of one-electron atoms and of the 2S-states of muonic atoms". *Zeit. Phys. A* **315**, p. 135 (1984).

[111] A. P. MARTYNENKO. "Priv. comm." .

[112] C. R. OTTERMANN ET AL. "Elastic electron scattering from ^{3}He and ^{4}He". *Nucl. Phys. A* **436**, p. 688 (1985).

[113] I. SICK. "Priv. comm." .

Acknowledgments

I would like to thank:

- Prof. Dr. T. W. Hänsch for the great opportunity to work is his group and on this outstanding experiment, as well as the great working environment that was provided at MPQ.
- Dr. Randolf Pohl for his excellent guidance over the years, all the fruitful discussions and the inspiration he provided. He allowed only for best possible results through his friendly yet constant "nit-picking". ;-)
- Dr. Franz Kottmann for his swiss calmness and precision, as well as for the seemingly infinite knowledge he shared with everyone around him. Also for his comments and corrections to my thesis and papers.
- Dr. Aldo Antognini, the true heart and spirit of the experiment and the entire collaboration. Success in the experiment would be unthinkable without his tireless work and uplifting spirit.
- Beatrice Franke, Julian Krauth, Johannes Götzfried, for all the friendly time we shared in the office, PSI, apartments and elsewhere. Also for their patience with me and for reading my thesis.
- Tobias Nebel, who provided me with a warm welcome in the group and was a prime example of a nice and friendly colleague that that everyone should aspire to be.
- Dr. Françoise Mulhauser for the life and efficiency she inspired in everyone around her.
- Dr. Andreas Dax and Dr. Szilla Czabo Foster for their help when initially setting up the experiment and teaching the secrets of the CT. I would have probably been lost otherwise.
- Dr. Andrea Gouvea, for her cheerful spirit and the nice company in Munich and at PSI.
- Prof. Lucile Julien, Dr. François Nez and Karsten Schumann for their continuous support and work in the laser hut and their company during the sometimes boring data taking shifts.
- Helmut Brückner, Karl Linner und Wolfgang Simon for their excellent work and help with all the small and big technical technical details that had to be realized.
- All the Technicians at PSI that tirelessly supported the experimentalists as well as the accelerator group for providing a stable beam.
- Prof. Alexei P. Martynenko and Prof. Ingo Sick for their insightful correspondence concerning from factors and QED calculations.
- Ingrid Hermann und Gabriele Gschwendtner for their friendly help and all their organizational effort.

Curriculum Vitae

Education

10.2012 - 12.2015: Dr. rer. nat. in Physics

Max Planck Institute of Quantum Optics Garching, Germany.
Thesis: ”The Lamb Shift in Muonic Helium Ions”
Advisors: Prof. Dr. Theodor W. Hänsch
Dr. Randolf Pohl

08.2013 - 08.2014: Experimental Work

Paul Scherrer Institute Villigen, Switzerland
Within the CREMA Collaboration

10.2010 - 09.2012: Master of Science in Physics

Ludwig Maximilians University Munich, Germany.
Thesis: ”Lifetime and Population of the 2S-State in Muonic Hydrogen and Deuterium”

10.2007 - 09.2010: Bachelor of Science in Physics

Ludwig Maximilians University Munich, Germany.
Thesis: ”Frequency Stabilization of a Spectroscopy Laser”

09.1998 - 08.2007: High School (Abitur)

Erasmus-Grasser-Gymnasium Munich, Germany.

09.1994 - 08.1998: Primary school

Camerloher Primary School Munich, Germany.

Publications

- **J. J. Krauth *et al.*, Theory of the n=2 levels in Muonic Deuterium**,
  Ann. Phys., Submitted
  arXiv:1506.01298
- **P. Amaro *et al.*, Quantum Interference Effects in Laser Spectroscopy of Muonic Hydrogen, Deuterium and Helium-3**,
  Phys. Rev. A. 92, 022514 (2015).

- **M. Diepold *et al.*, Improved X-ray Detection and Particle Identification with Avalanche Photodiodes**,
  Rev. Sci. Inst. 86, 053102 (2015).
- **J. Vogelsang *et al.*, Multi-pass Laser Cavity for Efficient Transverse Illumination of an Elongated Volume**,
  Opt. Express 22, 13050 (2014).
- **M. Diepold *et al.*, Lifetime and Population of the 2S State in Muonic Hydrogen and Deuterium**,
  Phys. Rev. A 88, 042520 (2013).
- **A. Antognini *et al.*, Proton Structure From the Measurement of 2S-2P Transition Frequencies of Muonic Hydrogen**,
  Science 339, 417 (2013).
- **R. Pohl *et al.*, Laser Spectroscopy of Muonic Hydrogen**,
  Ann. Phys. 525, 647 (2013).